UNIVERSITY OF CALIFORNIA
SANTA CRUZ

ADVANCING TYPE IA SUPERNOVA SCIENCE: THE SWOPE SUPERNOVA SURVEY AND RELATIONSHIPS BETWEEN i-BAND LIGHT CURVE DIVERSITY AND SPECTRAL PARAMETERS

A dissertation submitted in partial satisfaction of the
requirements for the degree of

Doctor of Philosophy

in

ASTRONOMY AND ASTROPHYSICS

by

César Rojas-Bravo

March 2025

The Dissertation of César Rojas-Bravo is approved:

Ryan J. Foley, Chair

Sandra Faber

Alex Filippenko

Enrico Ramírez-Ruiz

Armin Rest

Peter F. Biehl
Vice Provost and Dean of Graduate Studies

Table of Contents

List of Figures

List of Tables

Abstract

Advancing Type Ia Supernova Science: The Swope Supernova Survey and Relationships Between i-Band Light Curve Diversity and Spectral Parameters

by

César Rojas-Bravo

Since the beginning of the modern telescope, astronomers have thought of new surveys and methods to study astrophysical phenomena. In this dissertation, I present the Swope Supernova Survey, a low-redshift photometric survey at Las Campanas Observatory, Chile, detailing its motivation, methodology, and significant contributions to transient astrophysics. I also highlight my vital contributions to the survey and science enabled. Since its inception in 2016, the survey has established itself as a critical resource for the study of transients below $+30^\circ$ declination, offering a wide wavelength range (u to i band), precise calibration, and high observing cadences. I specifically focus on the first Type Ia Supernova (SN Ia) data release, an effort that I led to provide over 100 high-cadence light curves in five photometric bands. This dataset enhances low-redshift SN Ia samples and opens the path for future work that will significantly contribute to SN cosmology. Finally, I introduce a novel parametrization of i-band light-curve diversity. I present the $\Delta m_1 - \Delta m_2$ parameter, which captures differences between the data and model at the i-band secondary maximum and minimum. Strong correlations are identified between this parameter and key spectral features, such as Ca II pEW_0 and Si II v_0, highlighting the role of spectral variations in shaping i-band

light curves. This work also shows how these variations impact SN Ia composite spectra and synthetic photometry, revealing limitations in the widely used SALT3 SN Ia model. This dissertation highlights the importance of combining photometric and spectroscopic analyses to advance our understanding of SNe Ia, further exploring connections between SN Ia spectral features, i-band light-curve morphology and diversity, physical processes, environmental dependencies, and the accuracy of SNe Ia as precise cosmological distance indicators.

A mi familia: a quienes están conmigo y a quienes ya partieron.

Personal Acknowledgements

Gracias infinitas a mi familia; sin ellos, no estaría aquí. A ellos les debo todo.

Thanks to my advisor and my Thesis Committee. Thanks for all the support and advice. It's been a long journey, but it has been time well spent.

Thanks to the UCSC students, postdocs, faculty, and friends. Thanks for your patience, advice, and support. The best part of UCSC is the people.

Thanks to the Osterbrock Leadership Program: to Sandra, Bob, Judit. What I have learned from you goes beyond graduate school.

Published Material

Figures 2.7 and 2.8 are from Dimitriadis et al. (2019a,b). © AAS. Reproduced with permission.

Figure 2.9 is from Gagliano et al. (2022). © AAS. Reproduced with permission.

Figure 2.10 is from Hung et al. (2020). © AAS. Reproduced with permission.

Figure 2.11 is from Jacobson-Galán et al. (2020b). © AAS. Reproduced with permission.

Figure 2.12 is from Kilpatrick et al. (2021a). © Oxford University Press. Reproduced with permission.

Figures 2.13, 2.14, 2.15 are from Coulter et al. (2017), SCIENCE, 16 Oct 2017 Vol 358, Issue 6370, pp. 1556-1558, DOI: 10.1126/science.aap9811. Reprinted with permission from AAAS.

Parts of chapters 1 and 2 have been submitted to MNRAS.

Scientific Acknowledgements

I am incredibly thankful to the multiple collaborators and mentors I've had in so many projects throughout my Ph.D.: Ryan Foley, Enrico Ramírez-Ruiz, Armin Rest, David Jones, Justin Pierel, Georgios Dimitriadis, Charlie Kilpatrick, Kyle Davis, Yen-Chen Pan, Dave Coulter, Matt Siebert, Sandra Faber, Bob Williams, Alex Filippenko, Mark Phillips, Kaew Tinyanont, Kirsty Taggart, Prasiddha Arunachalam, Bruno Villaseñor, Ariadna Murguía-Berthier, Tony Piro, Gautham Narayan.

I am grateful to the Swope observers, who for many nights helped us during our observations: Jorge Anais Vílchez, Abdo Campillay, Piera Andrea King Soto, Yilin Kong Riveros, Nahir Muñoz-Elgueta, Natalie Ulloa, Jaime Vargas-González, and Nidia Morrell.

I also thank the staff at Lick Observatory and Las Campanas Observatory for their kind help throughout the Ph.D.; without all of you, it would not have been possible.

Fantastic thanks to the Osterbrock Leadership Program for financial support and professional development experiences. I cannot imagine my grad school without this support.

Chapter 1

Introduction

1.1 Dark Energy

The underlying cause of the accelerated expansion of the Universe is one of the most important open questions in astronomy and physics. Observations of Type Ia supernovae (SNe Ia) were fundamental to the discovery of the Universe's accelerated expansion (Riess et al. 1998; Perlmutter et al. 1999), and SNe Ia remain one of our most precise and important cosmological probes (Foley et al. 2018; Brout et al. 2019; Jones et al. 2019; Riess et al. 2022; Scolnic et al. 2022; DES Collaboration et al. 2024; Riess et al. 2024).

Together with measurements of baryon acoustic oscillations (BAO; e.g., Ross et al. 2015; Alam et al. 2017) and constraints on the cosmic microwave background (CMB), SN Ia measurements suggest that the Universe is flat, accelerating and mainly composed of dark energy ($\sim$70%), dark matter ($\sim$25%), and baryonic matter ($\sim$5%) (Planck Collaboration et al. 2018).

The exact nature of dark energy, a proposed solution to the accelerated expansion, still remains a mystery (see Kamionkowski & Riess 2023, for a recent review). Cosmologists often point to the dark energy equation-of-state parameter, w, which describes the relation between its pressure, P, and density, ρ,

$$P = w\rho c^2, \tag{1.1}$$

to distinguish between different dark energy models. A vacuum energy with $w = -1$, corresponding to a cosmological constant (whose value is often denoted by Λ), is the simplest model of dark energy. However, there are a variety of models besides the cosmological constant that could be dark energy. Values of w greater than -1 would imply a "quintessence" dark energy (a dynamic scalar field), while constant values of w of less than -1 would indicate a "phantom" dark energy, requiring exotic physics (Di Valentino et al. 2021). Alternatively, we may consider an equation of state that evolves with scale factor, a, parameterized as

$$w(a) = w_0 + w_a(1 - a), \tag{1.2}$$

where w_0 is the present-day value and w_a is the derivative of w with respect to redshift at $z = 0$ (Linder 2003). For a flat, wCDM universe, recent measurements from the Pantheon+ collaboration produce constraints of $w_0 = -0.978^{+0.024}_{-0.031}$, and when allowing w to vary with a, the best constraints are $(w_0; w_a) = (-0.841^{+0.066}_{-0.099}; 0.65^{+0.28}_{-0.32})$ (Brout et al. 2022a, see also Rubin et al. 2023; DES Collaboration et al. 2024).

The Hubble constant, H_0, is a cosmological parameter that can be measured with SN Ia observations. However, there is a disagreement for the value H_0 when measured locally by a combination of "calibrators" such as Cepheid variables and SNe Ia and that inferred from the inverse distance ladder measurement from the CMB and, for instance, BAO measurements (Riess et al. 2021). This disagreement might suggest physics beyond ΛCDM (Verde et al. 2019; Di Valentino et al. 2021; Kamionkowski & Riess 2023).

One can measure the expansion history of the Universe, which indirectly constrains cosmological parameters such as w and H_0, by measuring precise luminosity distances as a function of redshift. Owing to their standardizable nature (Phillips et al. 1999), SNe Ia (a carbon-oxygen white dwarf experiencing thermonuclear runaway; Hoyle & Fowler 1960) are exceptional cosmological distance indicators and have proven invaluable in performing this experiment. Constraining w does not require an absolute distance measurement, but instead relies on measuring precise relative distances of SNe Ia across a range of redshifts. An accurate absolute distance measurement is necessary to measure H_0. Distance ladder approaches rely on geometrically calibrated, relatively luminous, and plentiful stars to determine the luminosity of SNe Ia in external galaxies. An additional step on the distance ladder then results in SNe Ia in the Hubble flow, enabling the measurement of H_0. For both cases, low-redshift SNe Ia are necessary, and since there are currently more measured high-redshift than low-redshift SNe Ia, an individual low-redshift SN Ia has more statistical weight than a high-redshift SN Ia in these cosmological measurements (Foley et al. 2018).

1.2 Type Ia Supernovae

Supernovae are energetic stellar explosions. Besides their use in cosmology mentioned above, they are important because they produce iron-group elements and play an important role in the formation of new generations of stars (Liu et al. 2023).

SNe are broadly classified into two main classes depending on their spectroscopic features: Type I and Type II, the main difference being that SNe I do not have hydrogen in their spectra, while SNe II do (Minkowski 1941; Filippenko 1997; Parrent et al. 2012). SNe Ia do not have hydrogen or helium but show strong Si II absorption lines, strong S II lines, O, S, Ca lines, and Fe-group blends. They have typical expansion velocities of $-11,000$ km s^{-1} and typical peak magnitudes of -19.1 mag and -18.76 mag in B and R bands, respectively. They are the most commonly observed objects in SN surveys and are found in all galaxy types (Phillips et al. 1992; Gal-Yam 2017). However, there are several SN Ia subtypes, such as SN 1991T-like events (Filippenko et al. 1992b), overluminous by ~ 0.5 mag than a regular SN Ia, and SN 1991bg-like events (Filippenko et al. 1992a; Leibundgut et al. 1993), underluminous by ~ 1.1 mag in R band (Li et al. 2011).

There are two main proposed channels for the explosion mechanism of SNe Ia: the single-degenerate (SD) and double-degenerate (DD) scenarios, the most significant difference being the nature of the companion of the C-O white dwarf (C-O WD). In the SD scenario, the companion to the C-O WD is typically a non-degenerate star, such as a giant, subgiant, or main sequence star, from which the WD accretes material until it reaches close to the Chandrasekhar mass and explodes (Whelan & Iben 1973; Nomoto

1982). For the DD scenario, the companion is another WD (Iben & Tutukov 1984; Webbink 1984). However, there are several proposed mechanisms, such as dynamical mergers, where the primary WD accretes mass from the secondary WD, triggering a reaction that burns its C and produces a runaway thermal explosion, and violent mergers, where the orbit of the two WDs shrinks due to gravitational wave emission, leading to a violent merger and C detonation (Pakmor et al. 2010, 2012). Other proposed scenarios include the double-detonation models, where the primary WD has a He layer. The companion can be a He-donor, such as a non-degenerate He star (Nomoto 1982; Woosley et al. 1986; Livne 1990), accreting He onto the WD, inducing reactions that lead to C detonation (also called a sub-Chandrasekhar scenario since the WD does not necessarily reach the Chandrasekhar mass). The companion could also be a He-rich WD, inducing an explosion in the He-layer of the primary WD (Maeda & Terada 2016). Furthermore, another scenario considers a triple system containing at least two WDs, leading to a head-on collision between the two WDs, raising the temperature and leading to a C detonation (Kushnir et al. 2013).

SNe Ia are powered by the radioactive decay of elements produced in the explosion (Colgate & McKee 1969). Initially, they are powered by the decay of ^{56}Ni to ^{56}Co, which decays to ^{56}Fe, which is a stable isotope. During a typical SN Ia explosion, $\sim$ 0.3-0.8 $M_{\odot}$ of ^{56}Fe is produced (Arnett 1982). The peak brightness of the light curve is driven by the decay of ^{56}Ni, with its luminosity being directly related to the amount of this isotope synthesized during the explosion.

1.3 Type Ia Supernova Surveys

Over the past few decades, several SN surveys have been conducted to improve our understanding of SNe Ia and their use as cosmological probes. These surveys have covered a broad range of redshifts, as combining measurements across different redshift ranges strengthens constraints on cosmological parameters (Scolnic et al. 2022). Low-redshift SN observations are critical, since they serve as anchors to the high-redshift SN observations (Riess et al. 1999; Perlmutter et al. 1999).

Throughout the years there have been significant efforts in producing low-redshift SNe Ia surveys in the optical and near-infrared which have contributed significantly to measurements of w: Center for Astrophysics (Jha et al. 2006; Hicken et al. 2009, 2012), Carnegie Supernova Project (CSP) (Contreras et al. 2010; Stritzinger et al. 2011; Krisciunas et al. 2017; Phillips et al. 2019), Lick Observatory Supernova Search (Filippenko et al. 2001a; Ganeshalingam et al. 2010; Stahl et al. 2019), Foundation Supernova Survey (Foley et al. 2018), Young Supernova Experiment (Jones et al. 2021; Aleo et al. 2023), and Hawai'i Supernova Flows (Do et al. 2024). Nonetheless, recent SN Ia analyses have found that the relatively small current low-redshift sample limits our current cosmological knowledge (Foley et al. 2018; Scolnic et al. 2022; Brout et al. 2022a). While observing additional SNe Ia will improve statistical uncertainties, better data and techniques are required to improve the low-z SN systematic uncertainties. Low-z SN Ia samples must be improved to harness the advantages of the larger statistical leverage and lower systematic uncertainties in high-redshift SN samples (Scolnic et al. 2022; DES Collaboration et al. 2024).

A large sample of well-measured low-z SNe is necessary for the *Nancy Grace Roman Space Telescope* to successfully constrain dark energy at the precision required (Spergel et al. 2015). Although *Roman* will discover and measure distances to thousands of SNe Ia at medium or high z (i.e., $0.3 \lesssim z \lesssim 2$), a large sample of well-studied low-z ($0.03 < z < 0.1$) SNe Ia is fundamental to anchor *Roman*'s Hubble diagram (Hounsell et al. 2018; Rose et al. 2021). Additionally, the Rubin Observatory Legacy Survey of Space and Time (LSST; (Ivezić et al. 2019) will also contribute to the SN Ia observing efforts by observing a large number of transients from the southern hemisphere.

1.4 The Swope Supernova Survey

The Swope Supernova Survey (SSS, P.I. Anthony Piro) is a precisely calibrated, low-redshift ($z < 0.1$), follow-up imaging transient survey using the 1-m Swope telescope at Las Campanas Observatory, Chile (coordinates 29°00′57″ S, 70°41′31″ W). Since its beginning in 2016, the survey goals include obtaining a large number of well-sampled, multiband light curves of all types of SNe and other transients, the largest subset of which are SNe Ia.

Owing to its southern location, precise calibration, multiband capabilities ($uBVgri$ filters), and number of nights assigned, SSS has impacted different areas of transient astronomy. Data from SSS have contributed to studies of several science cases:

1. Physics of Type Ia Supernova Explosions (Dimitriadis et al. 2019a,b; Li et al. 2019; Wang et al. 2021a, 2024; Pearson et al. 2024).

2. Early/Young Non-Type Ia Supernova Transients (Gagliano et al. 2022; Tartaglia et al. 2018; Armstrong et al. 2021; Jacobson-Galán et al. 2024).

3. Exotic Transients (Hung et al. 2020; Jacobson-Galán et al. 2020a,c; Chen et al. 2023a,b; Nicholl et al. 2019; Holoien et al. 2020; Hinkle et al. 2021; Hung et al. 2021; Neustadt et al. 2020; Barna et al. 2021a; Jencson et al. 2021; Pastorello et al. 2022).

4. Supernova Progenitor Studies (Kilpatrick et al. 2018a, 2021a, 2022a; Vazquez et al. 2023).

5. Gravitational waves. Our team, through the SSS, discovered the first optical counterpart to a gravitational wave (GW) source, SSS17a (or AT 2017gfo; Coulter et al. 2017), and contributed to several additional studies of SSS17a or other GW events (Drout et al. 2017a; Kilpatrick et al. 2017; Murguia-Berthier et al. 2017a; Shappee et al. 2017; Siebert et al. 2017; Piro & Kollmeier 2018; Kilpatrick et al. 2021b; Coulter et al. 2024).

6. SN Ia Cosmology (see paragraph below).

The Swope telescope is one of the best-calibrated telescopes in the Southern Hemisphere (Rheault et al. 2014). With the Carnegie Supernova Projects (Phase 1 and Phase 2, CSP/CSP2), the Swope telescope has observed ∼300 low-redshift SNe Ia (Contreras et al. 2010; Stritzinger et al. 2011; Krisciunas et al. 2017; Phillips et al. 2019). The Swope Supernova Survey builds on this legacy by:

1. Increasing the Swope SN Ia supernova sample to constitute a significant portion

of the *Roman* telescope low-redshift requirement.

2. Observing every possible Cepheid/TRGB Type Ia supernova calibrator.

3. Re-observing CSP/CSP2 SN fields for calibration improvements.

4. Conducting additional standard-star observations.

My work on obtaining SN Ia distances with data from SSS is presented in detail in Chapter 3 of this dissertation.

1.5 The SALT3 SN Ia Model

The SALT (Spectral Adaptive Light-curve Template) model (Guy et al. 2007, 2010; Betoule et al. 2014) is a widely used empirical spectrophotometric SN Ia model, which represents SN Ia light curves as a combination of spectral energy distribution components which are derived from a model training process. This cosmology-independent training process includes data from numerous surveys, which reduces the model's sensitivity to the calibration of any particular survey.

The spectral flux density F for each SN Ia at a specific phase p and wavelength λ is given by (Taylor et al. 2023)

$$F(p,\lambda) = x_0 \times [M_0(p,\lambda) + x_1 M_1(p,\lambda)] \times \exp\left[c\,CL(\lambda)\right]. \tag{1.3}$$

,

where the SALT model components M_0, M_1, and CL are defined as follows:

1. M_0: spectral time-series that describes the mean SED of a SN Ia for $x_1 = 0$ and $c = 0$.

2. M_1: first-order deviations from M_0, associated with light-curve width.

3. CL: wavelength-dependent color law that accounts for phase-independent color variations originating from a combination of intrinsic supernova color and host-galaxy dust extinction.

These trained components, variances, and covariances are called a SALT surface. These SALT surfaces are used to fit the SN Ia light curves to determine its parameters:

1. x_0 (or m_B, proportional to the log of x_0): the overall flux normalization.

2. x_1: corresponding to the light-curve shape.

3. c: parametrization of the phase-independent color law.

This fitting process shifts the model in time and flux to match the data and, in doing so, determines the time of maximum brightness, t_0, and the peak brightness in the B band, m_B.

The most recent implementation of the SALT model is SALT3 (Kenworthy et al. 2021a; Taylor et al. 2023), which has significantly more training data (2.5 times larger than SALT2), improved uncertainty estimation, and improved separation of color and light-curve stretch. Additionally, the SALT3 wavelength range spans from 2000 to 11,000 Å, 1800 Å redder than SALT2.

The SALT3 parameters can be used to measure distances with the Tripp (1998) relation,

$$\mu_B = m_B - M_B + \alpha x_1 - \beta c, \tag{1.4}$$

where M_B is the B-band absolute magnitude for a reference SN Ia ($x_1 = 0$ and $c = 0$, which by definition corresponds to the mean of the `SALT3` training sample), μ_B is the distance modulus, and α and β are nuisance parameters adjusted to minimize Hubble residuals for a given sample.

1.6 Outline of This Work

In this dissertation, I will discuss the science I have led and enabled through the Swope Supernova Survey. In Chapter 2, I present a general overview of the Swope Supernova Survey: its motivation, science cases, operations and observing workflow, target selection, and some of the survey's scientific highlights to which I have contributed. In Chapter 3, I present the core of my dissertation: the Swope Supernova Survey's SN Ia data release: its motivation, detailed reduction methods, calibration, photometry, and Hubble diagram. While this chapter focuses on providing excellent distances, the SSS Ia data can also be used to study the physics of SN Ia progenitors and explosions, simulate future transient surveys, and train photometric classification algorithms. Finally, in Chapter 4, I present the SN Ia i-band light-curve characteristics and introduce a new correlation between its morphology and spectral parameters. This novel relationship opens new possibilities for improving SN Ia homogenization and modeling.

Chapter 2

Swope Supernova Survey overview

2.1 Motivation

We are in a "Golden Age" of time-domain astronomy. Since 2020, $\sim 20,000$ new transients have been reported yearly to the Transient Name Server (TNS), the official transient reporting mechanism of the International Astronomical Union (IAU)[1]. The Vera C. Rubin Observatory, seeing its first light in 2025, will issue approximately 10 million alerts per night (LSST Science Collaboration et al. 2009). The range of transient discoveries is extensive, from thermal runaway and core-collapse supernovae to gravitational-wave counterparts and stars destroyed around black holes.

The Swope Supernova Survey was established in 2016 to obtain optical multi-wavelength follow-up observations for this wide range of astrophysical explosions using

[1] https://www.wis-tns.org/stats-maps

the Swope 1-m telescope at Las Campanas, Chile. A collaboration between Carnegie Observatories scientists and University of California, Santa Cruz researchers, this survey covers multiple science topics, such as **(1)** determining the distances of SN Ia to understand the Universe's expansion rate, **(2)** understanding SN Ia explosions and progenitor systems, **(3)** early observations of young transients to detail their properties, **(4)** characterizing rare transients, **(5)** transient progenitor studies, and **(6)** discovering and following gravitational-wave counterparts.

My role in the overall operations of the survey was to communicate daily with the observers, add targets to the observing queue, create nightly schedules (and sometimes modify them in real-time), troubleshoot any problems in the data processing, and visually inspect the data quality after each observing night. I created around 1000 different schedules (communicating with the observers each night), processed and visually inspected data for approximately 850 nights, updated the calibration and photometry pipeline, and supported a wide range of science programs conducted using survey data. In this chapter, I introduce survey hardware in Section 2.2, describe survey operations in Section 2.3 with particular emphasis on my contributions, and discuss the science I have enabled through the survey in Section 2.4.

2.2 Hardware

The SSS uses the E2V CCD Camera on the Las Campanas Observatory Swope 1.0 m telescope, located near La Serena, Chile, which has a 29.7×29.8 arcmin^2 field of view and an f/7 focal ratio. The CCD camera consists of 4096×4112 pixels, read

out in four amplifiers of 2048 × 2056 pixels each. The plate scale is approximately 29.0″/mm, and each pixel is 15 μm wide for an effective pixel scale of approximately 0.435″. Following the Carnegie Supernova Project (Krisciunas et al. 2017), we only use amplifier 3, corresponding to the south-west quadrant of the detector, and place each SN near its center. A future data release will include photometric data from all amplifiers.

The electronic characteristics of the detector vary across each amplifier: for amplifier 3, the gain is approximately 1.00 e^-/ADU, while the read noise is 3.41 e^-.

We use six optical filters: Sloan *ugri* filters and Johnson *BV* filters (the throughput for each is shown in Figure 2.1). The filter functions are measured by observing a tunable light source through all optics (Rheault et al. 2014), which provides a relative throughput when combined with atmospheric transmission. Only the *BVgri* filters are used in this work. Observations in the *u* band have been acquired but require additional reduction and calibration efforts, and will be released in future work.

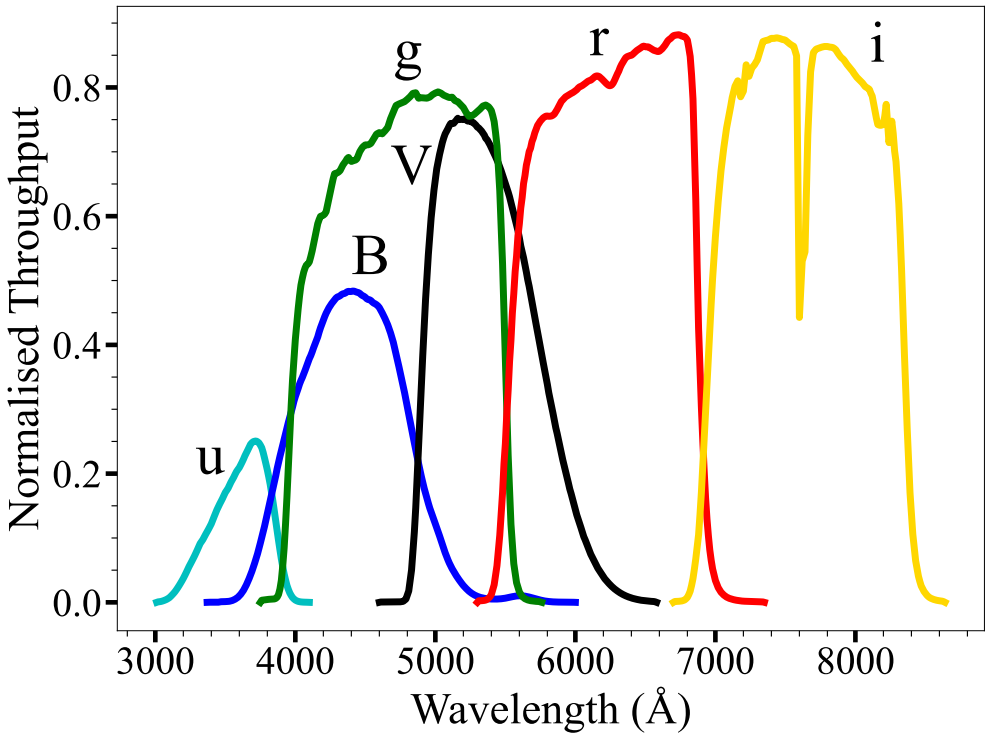

Figure 2.1 *uBVgri* Swope filter transmission functions. Measurements were made by observing a tunable light source through all optics, providing a relative throughput and atmospheric transmission (Rheault et al. 2014).

2.3 Survey Operations

2.3.1 Assigned nights

Since starting on 27 June 2016, the SSS has been allocated a total of 1319 nights (through the 2024A semester), corresponding to an average of 86 nights per semester and 48% of all available time on the telescope. Of these, 50 nights were weathered out or had technical issues. Because of COVID-19 policies, we were unable to use the telescope from March 14, 2020, to April 25, 2022, with some brief observations during April and October 2021 (see Figure 2.2). The survey leverages these nights to build this large, high-cadence, multiband SN Ia sample. Most of our allocated time is assigned

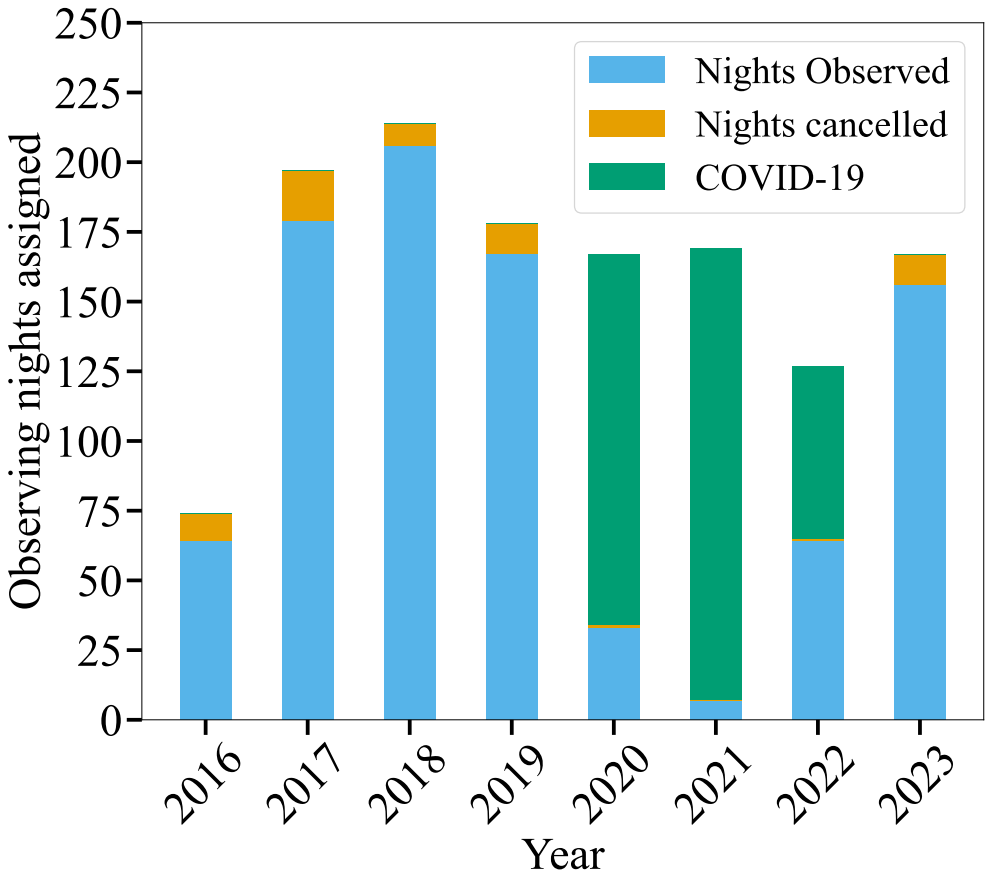

Figure 2.2 Number of assigned nights for the SSS from 2016–2023. We show nights where at least some observations were conducted in blue and those that were completely weathered out or had technical problems preventing observation in orange. From March 2020 to April 2022, the Swope telescope was mostly closed because of COVID restrictions, which we display in green. Ignoring the COVID-cancelled nights, SSS was able to observe 94% of all assigned nights.

in continuous runs of $\sim 7-10$ nights, and we avoid large ($\gtrsim$10-20 days) gaps between assigned nights when possible. We are generally assigned dark and grey nights to reduce the sky background.

Before each observing run, I coordinate with the Chilean observers, ensuring all the nights are covered, providing the observing codes, and ensuring everything is ready logistically for the observations.

2.3.2 Scheduling

On every assigned observing night, I generate a schedule with a target list, exposure times, and airmass plots according to the criteria listed in Section 2.3.4. Since we observe a wide range of targets (SNe Ia, other transients, standard-star observations, and template observations), I must carefully balance the targets. I then send the schedule to a member of our team physically located at the Swope telescope.

Our scheduling code[2] combines a user-defined priority and a priority based on observability per each target. I constantly monitor the progress of the observations in real-time, adjusting the schedule to the conditions of the night (such as weather and technical issues) and adding standard-star observations or templates when appropriate.

Once a SN Ia has significantly faded, corresponding to at least one year after peak, we obtain deep template images in all observed bands. Therefore, I carefully track all SN Ia observations and schedule templates when appropriate. Additionally, if a collaborator writes a scientific article on a transient we have observed, I also schedule templates for this object.

2.3.3 Data management

Starting in 2017, all data are automatically transferred to a server at UC Santa Cruz. Since mid-2018, data reduction has been automated and in real-time (see Section 3.4), thanks to the outstanding efforts of then-postdoc Charlie Kilpatrick and myself. The morning after each observing night, I checked all the images to inspect their quality, note any technical, observing, or reduction issues, and reschedule any deficient

[2] https://github.com/davecoulter/Scheduler

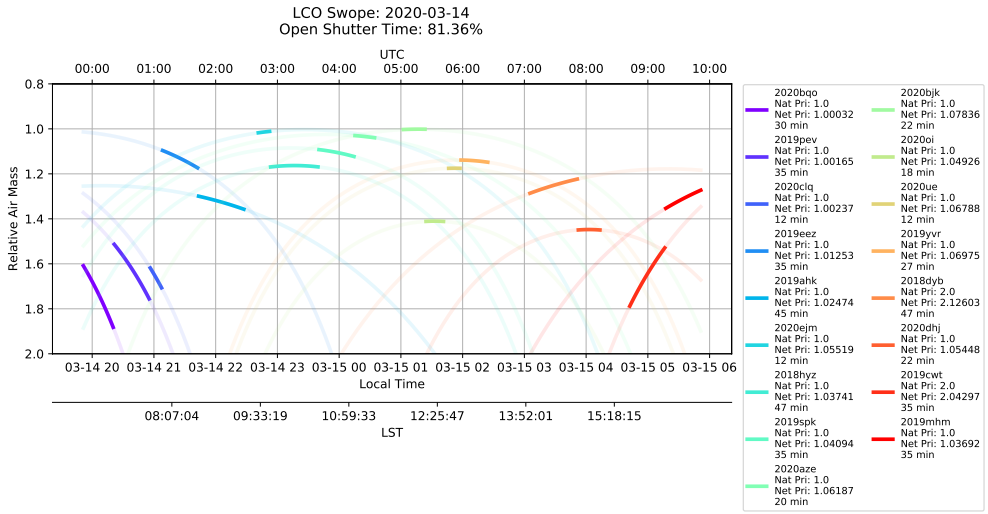

Figure 2.3 Example Swope Supernova Survey scheduling airmass plot: targets are assigned natural (manual input) and net (takes into account natural priority and target visibility) priorities. Observers located at the Swope telescope use this information to select the best targets throughout the night.

observations. If any images present any reduction errors, I troubleshoot the problem and manually finish reducing any pending data. I estimate I have inspected data for at least 850 different nights.

Once the photometry has been processed, all the photometry is uploaded to the transient survey management platform YSE-PZ[3] (Coulter et al. 2023). YSE-PZ allows for a helpful visualization of photometry, spectra, and other relevant information for each transient, enabling better practical monitoring of each transient (Fig. 2.4).

2.3.4 Target selection

Most of the observations of our survey are of SNe Ia; however, we also observe other types of transients, such as core-collapse supernovae, tidal disruption events, and

[3] https://ziggy.ucolick.org/yse

superluminous supernovae (Fig. 2.6).

We continually examine new discoveries and classifications reported to the IAU Transient Name Server (TNS)[4]. We use the transient survey management platform YSE-PZ (Coulter et al. 2023), which automatically collates significant metadata, enhanced data products, and publicly available SN data, to select targets. YSE-PZ is built on a relational database and has the ability to easily select subsets of all SNe using ad-hoc queries.

Type Ia supernovae

To avoid potential host-galaxy biases, we draw our SN Ia sample from mostly untargeted SN surveys. Most of the SSS SNe Ia are discovered by the following surveys (in alphabetical order): All-Sky Automated Survey for Supernovae (Shappee et al. 2014), Asteroid Terrestrial-impact Last Alert System (ATLAS) (Tonry et al. 2018), *Gaia* Photometric Science Alerts (Hodgkin et al. 2021), Distance Less Than 40 Mpc survey (DLT40) (Tartaglia et al. 2018), Pan-STARRS Survey for Transients (PSST) (Chambers et al. 2016), Young Supernova Experiment (YSE) (Jones et al. 2021; Aleo et al. 2023), and Zwicky Transient Facility (ZTF) (Bellm et al. 2019). We do not exclude SNe discovered by amateurs or galaxy-targeted searches since most of these SNe would have eventually been discovered by an untargeted survey if the discovery survey did not exist. Avoiding such SNe could also bias our sample *away* from massive host galaxies.

If a SN Ia fulfills the following criteria, we attempt to observe it as part of the SSS:

[4] https://wis-tns.weizmann.ac.il/

1. Is spectroscopically confirmed as a SN Ia.

2. Has Milky Way reddening ($E(B-V)_{\rm MW} < 0.2$ mag.

3. Is observable from Las Campanas Observatory at an airmass less than 2.

4. Is distant enough to be in the Hubble flow ($z > 0.015$) but close enough to avoid Malmquist bias while obtaining high signal-to-noise ratio (S/N) observations ($z \lesssim 0.08$), *or* close enough where we could measure a Cepheid or Tip of the Red Giant Branch (TGRB) distance ($D \lesssim 40$ Mpc or $z \lesssim 0.01$).

5. The first Swope observation would occur before maximum brightness.

6. Is observable around maximum brightness during our scheduled time and for at least 45 days after maximum brightness.

7. Will be able to obtain a high-cadence light curve (minimum upcoming observing gaps and space in the observing schedule).

Some SNe Ia may also be observed if they do not fulfill all of these criteria. In particular, we observe all SNe at $D < 20$ Mpc regardless of classification, and therefore we sometimes start observations of a SN Ia at these distances before a classification is reported. SNe Ia were also observed with Swope as part of various related projects, such as observing all SNe also observed by K2 (the Kepler space telescope; Haas et al. 2010), where a SN Ia could be observed despite it having a distance/redshift outside of our nominal range.

During the first months of the survey, we followed several SNe Ia even though they were past maximum brightness because the Foundation Supernova Survey (Foley

et al. 2018) was following these SNe, and we wanted to compare our observations directly. Some of these light curves are also part of this data release, although they may not be useful for cosmological analyses without other data from, e.g., the Foundation Supernova Survey.

If the general observing conditions were good (i.e., no or minimal clouds and stable weather) and the seeing was $<1.8''$ and stable, we performed deep template observations of the locations of previously observed but now faded SNe in the same filters previously observed. In these conditions, we combined observations of SNe and templates during the same night. The fraction of the night dedicated to SNe or templates depends on seeing and observing constraints and relative priorities of all targets. The day after we observe a template, we visually inspect the template image to verify its quality; closer inspection is done at the SN position to check for nearby cosmic rays or saturated pixels. We additionally measure the FWHM and image depth.

During the first eighteen months of the survey, we took "snapshot" observations of interesting (e.g., nearby SNe in potential Cepheid galaxies with low reddening and recent non-detections) where we observed a single epoch in all bands. We would not observe the transient again until it was classified and met the above criteria. This strategy allowed us to get our first observations before peak brightness for several SNe Ia, the trade-off being that occasionally we had to drop transients since they were not classified quickly enough. We abandoned this strategy as transient surveys increased in area and improved their cadence.

Other transients

If a non SN Ia transient is interesting for several possible reasons (nearby, has progenitor data, peculiar), or when a collaborator requests observations, we add the transient to our nightly schedule. There are no specific limitations on the selection of non SN Ia observations.

Standard-star observations

When a night was photometric (i.e., favorable forecast during the day; no clouds observed at dusk, dawn, or throughout the night; and constant counts for stars as measured by the guide camera), we would attempt to observe standard stars from the CALSPEC catalog[5] (Bohlin et al. 2014, 2020) and several precisely calibrated white dwarfs (Narayan et al. 2019). On photometric nights, the standard-star observations were integrated with high-priority SN observations.

2.3.5 Exposure time and cadence

For each observation, we calculate the exposure time expected to return a S/N of 30 in typical situations. After the initial calculation, the exposure times were adjusted if the transient was nuclear (increasing) or if the SN was extremely bright (decreasing due to possible saturation). Because of the relative filter throughputs, the exposure times for the $Vgri$ exposures were usually identical, but the B band required longer exposures.

Our ideal cadence is to observe each SN Ia nightly before and around maximum

[5] https://www.stsci.edu/hst/instrumentation/reference-data-for-calibration-and-tools/astronomical-catalogs/calspec

brightness, switching to every three days until 20 days after peak, then updating to four days until 40 days after peak, and adjusting to seven days until 45 days after peak. We attempt to obtain at least one observation $\gtrsim$45 days after peak to obtain a late-time color.

For those SNe whose luminosity can potentially be calibrated by observations of Cepheids or the TRGB, we observe nightly until it sets or is no longer detectable.

Because of weather and not being assigned telescope time every night, the cadence is slightly worse than desired. Before and after peak, the SNe Ia in our sample have a median cadence of 3 and 5.5 days, respectively.

Our initial observations of each SN are with all available filters. This continues for each subsequent epoch until the SN is no longer detectable in a 600 second *gri* exposure. This process continues until either the SN sets, the SN fades and is undetectable, or it is observed until $\sim$45 days after peak. On average, the SNe Ia in DR1 are observed for 10 epochs (Figure 3.3).

Figure 2.4 Example YSE-PZ page for transient SN 2018aoz. The helpful visualization of photometry from our survey and other sources, spectral plots, finder chart generation, and other SN information allows effective monitoring of each transient.

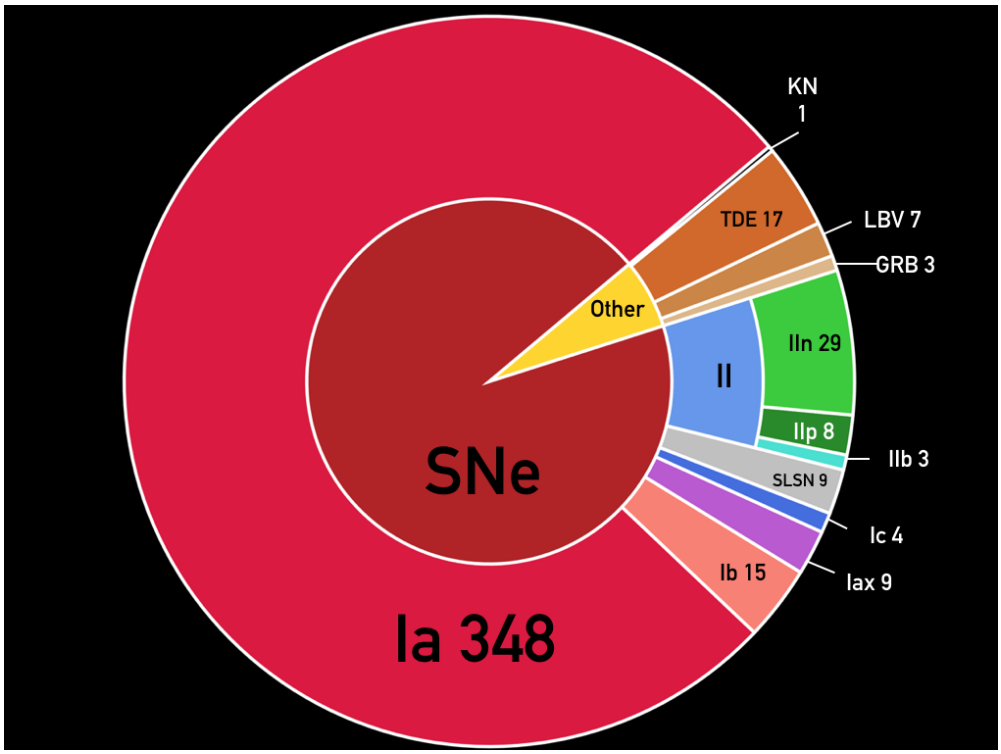

Figure 2.5 Swope Supernova Survey Observations by Type. Most of the observations of our survey are of SNe Ia; however, we also observe other types of transients, such as core-collapse supernovae, tidal disruption events, and superluminous supernovae.

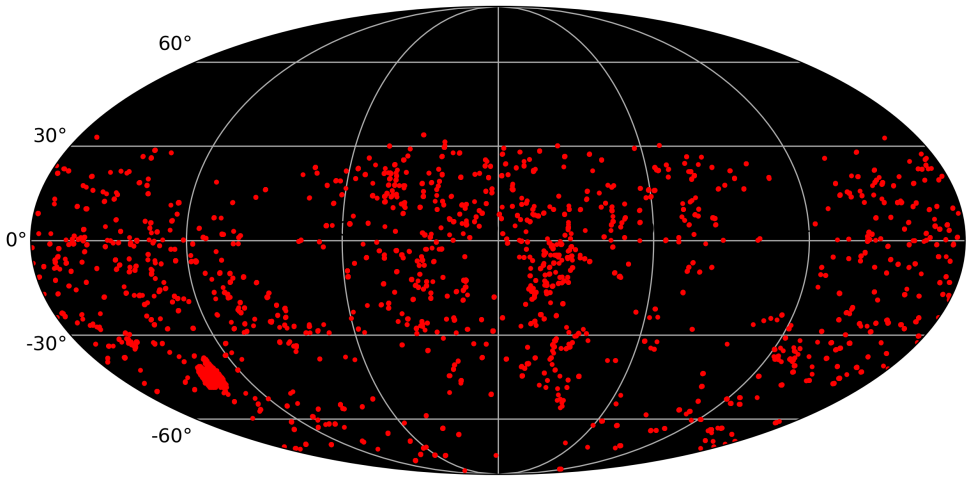

Figure 2.6 Swope Supernova Survey Observations visualized in a Mollweide projection. We observe transients across the sky visible from Las Campanas Observatory, avoiding the Milky Way when possible. The clumps correspond to gravitational-wave searches.

2.4 Swope Supernova Survey Scientific Highlights

The Swope Supernova Survey has been a prolific collaboration, with 41 submitted and published papers (see Table 2.1 for a complete list), over 3,500 citations, and an h-index of 27[6]. Here I present all the papers from the Swope Supernova Survey, grouped as follows: papers related to SN cosmology (Section 2.4.1), SN Ia physics (Section 2.4.2), young non-SN Ia transients (Section 2.4.3), exotic transients (Section 2.4.4), SN progenitors (Section 2.4.5), and gravitational waves (Section 2.4.6).

For all the research papers mentioned below and in Table 2.1, my specific contributions were:

1. Coordination with local observers at Las Campanas Observatory.
2. Daily scheduling of the objects of interest.
3. Daily monitoring of the objects of interest (magnitude estimate for exposure-time calculation, quality control of images observed).
4. Photometric reductions of objects of interest.
5. All the above steps were also performed if template observations were needed for host-galaxy subtraction.
6. If template observations were needed for host-galaxy subtraction, I also performed additional science-template photometry.
7. Sending the final data to the primary authors of the research articles.

[6] https://ui.adsabs.harvard.edu/public-libraries/qzIc960PSDGA7fFjsjhqwA

8. Overall reading of the manuscripts and checking SSS and observer acknowledgments.

Table 2.1. Papers from the Swope Supernova Survey

Title	First Author	Year	Journal
A Neutron Star Binary Merger Model for GW170817/GRB 170817A/SSS17a	Murguia-Berthier, A.	2017	ApJ
The Unprecedented Properties of the First Electromagnetic Counterpart to a Gravitational-wave Source	Siebert, M. R.	2017	ApJ
Early spectra of the gravitational wave source GW170817: Evolution of a neutron star merger	Shappee, B. J.	2017	Science
Swope Supernova Survey 2017a (SSS17a), the optical counterpart to a gravitational wave source	Coulter, D. A.	2017	Science
Light curves of the neutron star merger GW170817/SSS17a: Implications for r-process nucleosynthesis	Drout, M. R.	2017	Science
Electromagnetic evidence that SSS17a is the result of a binary neutron star merger	Kilpatrick, C. D.	2017	Science
The Early Detection and Follow-up of the Highly Obscured Type II Supernova 2016ija/DLT16am	Tartaglia, L.	2018	ApJ
Connecting the progenitors, pre-explosion variability and giant outbursts of luminous blue variables with Gaia16cfr	Kilpatrick, Charles D.	2018	MNRAS
Evidence for Cocoon Emission from the Early Light Curve of SSS17a	Piro, Anthony L.	2018	ApJ
First ALMA Light Curve Constrains Refreshed Reverse Shocks and Jet Magnetization in GRB 161219B	Laskar, Tanmoy	2018	ApJ
X-ray limits on the progenitor system of the Type Ia supernova 2017ejb	Kilpatrick, Charles D.	2018	MNRAS
K2 Observations of SN 2018oh Reveal a Two-component Rising Light Curve for a Type Ia Supernova	Dimitriadis, G.	2019	ApJ
Nebular Spectroscopy of Kepler's Brightest Supernova	Dimitriadis, G.	2019	ApJ
Photometric and Spectroscopic Properties of Type Ia Supernova 2018oh with Early Excess Emission from the Kepler 2 Observations	Li, W.	2019	ApJ
The tidal disruption event AT2017eqx: spectroscopic evolution from hydrogen rich to poor suggests an atmosphere and outflow	Nicholl, M.	2019	MNRAS
To TDE or not to TDE: the luminous transient ASASSN-18jd with TDE-like and AGN-like qualities	Neustadt, J. M. M.	2020	MNRAS
SN 2013aa and SN 2017cbv: Two Sibling Type Ia Supernovae in the Spiral Galaxy NGC 5643	Burns, Christopher R.	2020	ApJ
Ca hnk: The Calcium-rich Transient Supernova 2016hnk from a Helium Shell Detonation of a Sub-Chandrasekhar White Dwarf	Jacobson-Galán, Wynn V.	2020	ApJ
The Rise and Fall of ASASSN-18pg: Following a TDE from Early to Late Times	Holoien, Thomas W. -S.	2020	ApJ
SN 2019ehk: A Double-peaked Ca-rich Transient with Luminous X-Ray Emission and Shock-ionized Spectral Features	Jacobson-Galán, Wynn V.	2020	ApJ
Double-peaked Balmer Emission Indicating Prompt Accretion Disk Formation in an X-Ray Faint Tidal Disruption Event	Hung, Tiara	2020	ApJ
Discovery and follow-up of ASASSN-19dj: an X-ray and UV luminous TDE in an extreme post-starburst galaxy	Hinkle, Jason T.	2021	MNRAS
SN 2019muj - a well-observed Type Iax supernova that bridges the luminosity gap of the class	Barna, Barnabás	2021	MNRAS
A cool and inflated progenitor candidate for the Type Ib supernova 2019yvr at 2.6 yr before explosion	Kilpatrick, Charles D.	2021	MNRAS
Discovery of a Fast Iron Low-ionization Outflow in the Early Evolution of the Nearby Tidal Disruption Event AT 2019qiz	Hung, Tiara	2021	ApJ
AT 2019qyl in NGC 300: Internal Collisions in the Early Outflow from a Very Fast Nova in a Symbiotic Binary	Jencson, Jacob E.	2021	ApJ

Table 2.1 (cont'd)

Title	First Author	Year	Journal
SN2017jgh: a high-cadence complete shock cooling light curve of a SN IIb with the Kepler telescope	Armstrong, P.	2021	MNRAS
The Gravity Collective: A Search for the Electromagnetic Counterpart to the Neutron Star-Black Hole Merger GW190814	Kilpatrick, Charles D.	2021	ApJ
SN 2018agk: A Prototypical Type Ia Supernova with a Smooth Power-law Rise in Kepler (K2)	Wang, Qinan	2021	ApJ
An Early-time Optical and Ultraviolet Excess in the Type-Ic SN 2020oi	Gagliano, Alexander	2022	ApJ
Updated Photometry of the Yellow Supergiant Progenitor and Late-time Observations of the Type IIb Supernova SN 2016gkg	Kilpatrick, Charles D.	2022	ApJ
Forbidden hugs in pandemic times. IV. Panchromatic evolution of three luminous red novae	Pastorello, A.	2023	A&A
The Optical Light Curve of GRB 221009A: The Afterglow and the Emerging Supernova	Fulton, M. D.	2023	ApJ
The Type II-P Supernova 2019mhm and Constraints on its Progenitor System	Vazquez, J.	2023	ApJ
Late-time Hubble Space Telescope Observations of AT 2018cow. I. Further Constraints on the Fading Prompt Emission and Thermal Properties 50-60 days Post-discovery	Chen, Yuyang	2023	ApJ
Late-time Hubble Space Telescope Observations of AT 2018cow. II. Evolution of a UV-bright Underlying Source 2-4 Yr Post-discovery	Chen, Yuyang	2023	ApJ
Strong Carbon Features and a Red Early Color in the Underluminous Type Ia SN 2022xkq	Pearson, Jeniveve	2024	ApJ
Flight of the Bumblebee: the Early Excess Flux of Type Ia Supernova 2023bee Revealed by TESS, Swift, and Young Supernova Experiment Observations	Wang, Qinan	2024	ApJ
The Gravity Collective: A Comprehensive Analysis of the Electromagnetic Search for the Binary Neutron Star Merger GW190425	Coulter, D. A.	2024	ApJ, subm.
Final Moments. II. Observational Properties and Physical Modeling of Circumstellar-material-interacting Type II Supernovae	Jacobson-Galán, W. V.	2024	ApJ
Swope Supernova Survey: First Photometric Data Release of 111 Type Ia Supernovae	Rojas Bravo, César	2025	MNRAS, subm.

Note. — List of all the papers produced by the Swope Supernova Survey. Due to my data reduction/scheduling/survey management efforts, I am a co-author in all the above research articles.

2.4.1 Type Ia supernova cosmology

SSS SN cosmology efforts currently consist of two papers, the main one being the survey's first SN Ia data release (Rojas-Bravo et al., submitted to *MNRAS*), presented in detail in Chapter 3. In this paper, we list the SSS SN Ia program motivations and advantages, describe the SN Ia observations, introduce our novel photometry pipeline, describe the survey's calibration, and present the light curves and model fits. Additionally, we compare our observations to the Foundation Supernova Survey (Foley et al. 2018), and present a Hubble Diagram with our photometric data. Finally, we discuss the next steps and future directions for the SSS SN Ia survey.

Additionally, SSS obtained the images for SN 2017cbv, sibling to SN Ia 2013aa, in the spiral galaxy NGC 5643. These SNe Ia were observed with the same telescope and instruments (eliminating most instrumental systematics) and by having the same host galaxy, eliminating peculiar-velocity and distance systematics. These conditions make these SNe ideal candidates as testbeds for the precision of SNe Ia as standard candles (Burns et al. 2020).

2.4.2 Physics of Type Ia supernova explosions

SNe Ia are believed to result from thermonuclear disruptions of white dwarf stars; however, the dominant progenitor channel for these events remains uncertain (Maoz et al. 2014). Progenitor systems may include double-degenerate (DD) systems with two white dwarfs (Iben & Tutukov 1984; Webbink 1984) and single-degenerate (SD) systems, where a white dwarf explodes due to accretion from a companion star (Whelan & Iben 1973). Several unresolved problems remain unanswered, such as whether SNe Ia

with different progenitors appear so similar, the typical masses, ages, and metallicities of SD progenitor systems, the relative fraction of each progenitor type, and possible bias of cosmological parameters if the relative progenitor rates vary with redshift. Understanding these astrophysical systematics is separate from current efforts to reduce calibration systematics and requires a deeper understanding of the physics of the SN Ia explosions and progenitors.

Observations within a few days of a SN Ia explosion can help differentiate between various progenitor scenarios. For example, shock interaction with a non-degenerate companion (Kasen 2010) and the presence of extended or circumstellar material (CSM) (Piro & Morozova 2016) can significantly influence early-time light curves. The SSS has contributed to important papers that challenge traditional SN Ia models, expanding the limits of our understanding of SN Ia physics. Examples of SNe Ia with early SSS observations that contribute to our SN Ia understanding are SN 2018oh, SN 2018agk, SN 2023bee, and SN 2022xkq.

SN 2018oh

K2 (Haas et al. 2010) observations of SN Ia 2018oh (Dimitriadis et al. 2019a) with a 30-minute cadence revealed a two-component rising light curve, covering pre-SN, during, and post-SN explosion. This supernova presents a "flux-excess" relative to normal SN Ia behavior, peaking $\approx$ two days after the explosion. Extensive additional optical, ultraviolet, and near-infrared photometry (including a great amount of Swope $uBVgri$ photometry, which I scheduled and reduced), plus high-cadence optical spectra, helped characterize in great detail many SN 2018oh properties, such as rise time, Δm_{15}

(B-band), peak luminosity, and ^{56}Ni mass (Li et al. 2019). The early- and late-time Swope photometry helped constrain the color evolution of SN 2018oh (Figure 2.7).

The flux excess observed in SN 2018oh was initially attributed to the interaction between the SN ejecta and a Roche-lobe-filling non-degenerate companion star. However, late-time Swope photometry and Keck spectra, obtained 235-270 days after peak brightness, paint another picture. No narrow H or He emission was detected in the nebular spectrum, which would have been expected from the stripped material of a companion star once the SN ejecta became optically thin (Dimitriadis et al. 2019b). Stringent upper limits on hydrogen and helium, along with the absence of late-time narrow emission features, contradict the early interpretation of a companion interaction. The combination of flux excess, blue color, and lack of late-time emission features remains unexplained by any existing model (Dimitriadis et al. 2019b).

SN 2018agk, SN 2023bee, SN 2022xkq

SSS photometry has further complemented early space-based observations of two SNe Ia, each presenting different progenitor scenarios. SN 2018agk was observed by the K2 telescope one week before explosion, during the entire rise, and until +40 days after peak with a 30-minute cadence, in which no excess flux was detected, effectively ruling out a scenario with a nondegenerate companion undergoing Roche-lobe overflow at small viewing angles (Wang et al. 2024). In contrast, SN 2023bee's early TESS and Swift UV data show a redder, less luminous excess flux than other early SN Ia observations, such as SN 2018oh. A comparison of SN 2023bee's space- and ground-based photometric observations (including SSS data) and optical spectra with early

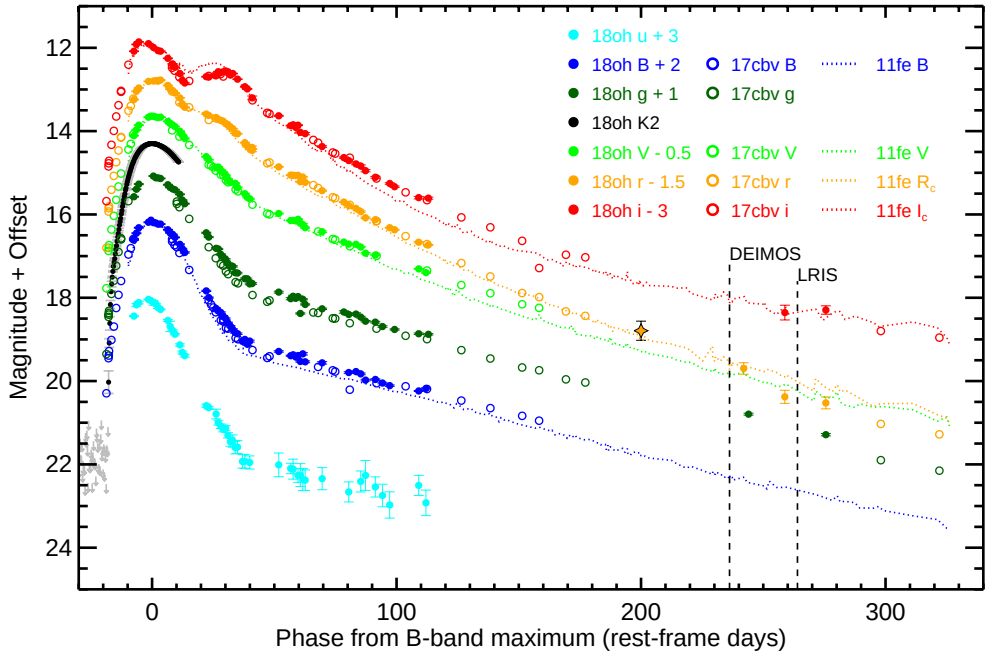

Figure 2.7 Swope $uBVgri$ light curves of SN 2018oh (full circles) as shown in Dimitriadis et al. (2019b), compared to SN 2011fe and SN 2017cbv observations. Vertical black dashed lines correspond to dates of late-time DEIMOS and LRIS spectra.

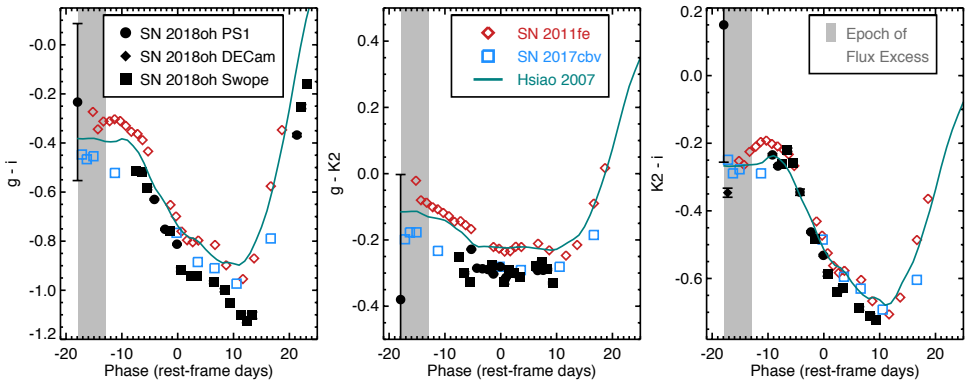

Figure 2.8 Early-time color curves for SN 2018oh as presented in Dimitriadis et al. (2019a), including data from the Swope Supernova Survey, compared to SN 2011fe, SN 2017cbv, and Hsiao (Hsiao et al. 2007) templates. The gray-shaded region corresponds to the flux excess period.

excess flux models reveals that no existing model accurately reproduces the data. This suggests that (a) none of the suggested physical mechanisms accurately represent the

source of the flux excess, or (b) the current models are not sophisticated enough (Wang et al. 2021b).

Additionally, SSS optical data complemented optical, IR, UV, and radio observations of SN 2022xkq, an underluminous and fast-declining SN 1991-bg-like SN Ia, which also possesses an early flux excess prominent in redder bands. SN 2022xkq's multiple spectra exhibit carbon detections, which are hard to align with a double detonation of a sub-Chandrasekhar WD (suggested by the early red excess flux). Similarly to SN 2023bee, no current explosion model can explain this object's photometric and spectroscopic data (Pearson et al. 2024).

2.4.3 Early/Young Non-Type Ia Supernova Transients

In addition to early observations of SNe Ia, early SSS observations have also contributed to our understanding of the progenitors of non-SN Ia transients, such as SN 2020oi (Type Ic, Gagliano et al. (2022), SN 2016ija (Type II, Tartaglia et al. (2018)), and SN 2017jgh (Type IIb, Armstrong et al. (2021)). The multiple photometric and spectroscopic data for each study demonstrate the valuable insights gained from early-time observations.

Type Ic supernovae (SNe Ic) are core-collapse transients that lack hydrogen and helium lines in their spectra, signifying that the progenitor star's outer layers were stripped away before the explosion. Their progenitor systems remain unresolved and are even ambiguous from pre-explosion photometry (Kilpatrick et al. 2018b). Detailed photometric and spectroscopic observations (including SSS observations, see Fig. 2.9) of nearby SN 2020oi, located in M100, 17.1 Mpc away, has helped increase our knowledge

of this type of transients, characterizing its evolution and constraining its progenitor system (Gagliano et al. 2022). Its early flux excess and derived SN bolometric luminosity suggest an ejecta interaction with circumstellar material. Hubble Space Telescope (HST) pre-explosion imaging reveals a likely stellar cluster in the SN's location, consistent with a low-mass progenitor system derived from spectral modeling analysis.

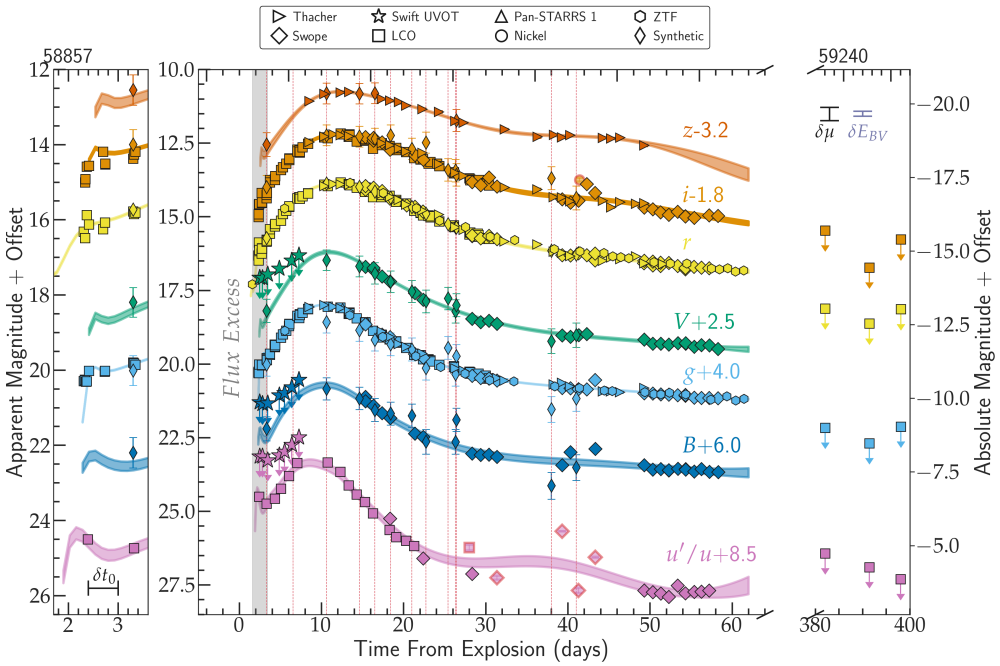

Figure 2.9 Host-galaxy subtracted photometry for SN 2020oi presented in Gagliano et al. (2022), including data from the Swope Supernova Survey. Photometric data helped assess its photometric evolution and model its bolometric luminosity.

Additionally, early photometric observations and follow-up, including SSS data, of Type II SN 2016ija and Type IIb SN 2017jgh have enabled a further understanding of these transient types. The observations of SN 2016ija, which show a rapid rise time and a bright V-band absolute magnitude at peak, challenge the prediction that luminous SNe II typically exhibit longer rise times compared to other subluminous events (Tartaglia et al. 2018). Early *K2* and ground-based observations of Type IIb (possess-

ing helium in the spectrum but with disappearing H, Filippenko (1997)) of SN 2017jgh reveal its progenitor to likely be a yellow supergiant with a constrained envelope radius, envelope mass, and shock velocity (Armstrong et al. 2021).

Finally, SSS provided partial $uBVgri$ data for a large Type II SN sample compiled in Jacobson-Galán et al. (2024). This work, the largest SN II sample with spectroscopic evidence for CSM interaction, finds a significant correlation between peak UV brightness and rise time, quantifies mass-loss rates, and analyzes several subsamples based on photometric and spectroscopic properties.

2.4.4 Exotic Transients

In the last twenty-five years, numerous explosions have been discovered that do not fit into the traditional supernova classifications (Ia, II, Ib/c). Among these are calcium-rich transients (Filippenko et al. 2003; Jacobson-Galán et al. 2020a,c), and "rapid evolvers" (Ho et al. 2023; Chen et al. 2023a,b), a group of exotic transients that achieve SN luminosities but with much faster timescales ($\sim$ an order of magnitude). Understanding the nature of these transients requires high-cadence optical light curves, which can be obtained using the Swope telescope.

Additionally, tidal disruption events (TDEs) occur when a star passes too close to a supermassive black hole (SMBH): the SMBH's tidal forces overpower the star's self-gravity, tearing it apart. Some of this disrupted material is ejected, while the rest accretes onto the black hole, producing a luminous accretion flare (Rees 1988; Phinney 1989; Gezari 2021). The Swope Supernova Survey has observed several bright TDEs, combining the Swope light curves with other multiwavelength spectra and photometry

for detailed studies.

AT 2018hyz

The SSS provided *gri* photometric data for the TDE AT 2018hyz (Fig. 2.10), the first unambiguous case of resolved double-peaked Balmer emission in a TDE (Hung et al. 2020). This discovery is the first observational evidence of prompt circularization after the disruption of a star. SSS's photometry, along with Swift XRT observations, were used for temperature, luminosity, and radius measurements, assuming the UV and optical emission were characterized by a blackbody spectrum: by interpolating the Swope data to the Swift epochs, the authors found the light curve is well described by a black body temperature of $\sim$ 18,000 K. Overall, observations of AT 2018hyz align with classical models where the formation of a new accretion disk powers TDE flares. This study is a reference for future investigations into the physics of accretion disks around supermassive black holes under diverse accretion conditions.

Calcium-Rich Transients: SN 2016hnk and SN 2019ehk

Calcium-rich supernovae are believed to originate from progenitor systems involving a WD; they exhibit peak magnitudes ranging from -14 to -16.5 mag, rapidly evolving light curves, and prominent calcium features (Taubenberger 2017); SN 2016hnk is an example. SSS observations contributed to the understanding of some key characteristics of this object: its intrinsically red color, low luminosity, fast-rising light curve, and ^{56}Ni mass. In addition to the observed spectra, SN 2016hnk light curves are consistent with the result of a helium-shell (0.02 $M_{\odot}$) double-detonation explosion of a

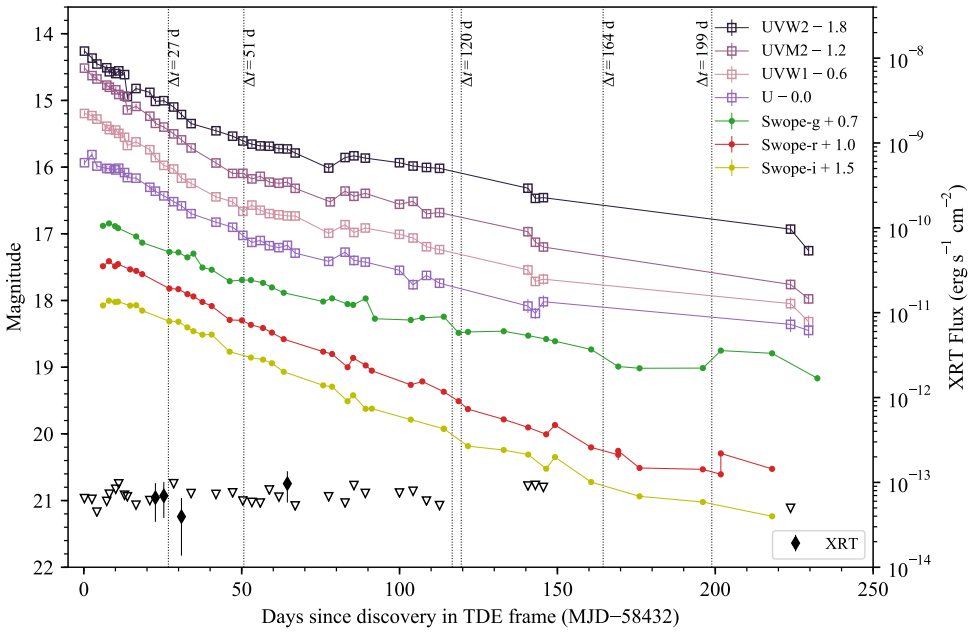

Figure 2.10 Multiwavelength light curve of TDE AT 2018hyz, as presented in Hung et al. (2020). The Swope *gri* photometry was key for temperature and luminosity measurements.

$0.85M_{\odot}$ C/O WD, making it just the second observed case of such He-shell double-detonation, suggesting a thermonuclear explosion different from typical SNe with low luminosity and strong Ca II emission (Jacobson-Galán et al. 2020a).

Additionally, the SSS provided *uBVgri* observations for the calcium-rich transient SN 2019ehk (Jacobson-Galán et al. 2020c) (Figure 2.11). Located in the star-forming galaxy M100, SSS data, along with other ground-based photometry, were able to show a double-peaked optical light curve, a quick rise-time, and peak absolute magnitude consistent with Ca-rich SN models. The pseudobolometric light curve derived from the photometry provided a blackbody luminosity, temperature, and radius. Furthermore, the bolometric light curve models calculate this event's nickel and ejecta mass. In addition to the optical, X-ray, UV, NIR, and radio data, pre-explosion HST,

Chandra, and Spitzer imaging (no source detected in any archival imaging), and optical spectra, this work places tight constraints on this type of SN progenitor models. It suggests a strong interaction with CSM. Finally, this work presents the first evidence of hydrogen- and helium-rich CSM surrounding a Ca-rich transient and the first detection of X-ray emission from such an event (Jacobson-Galán et al. 2020c).

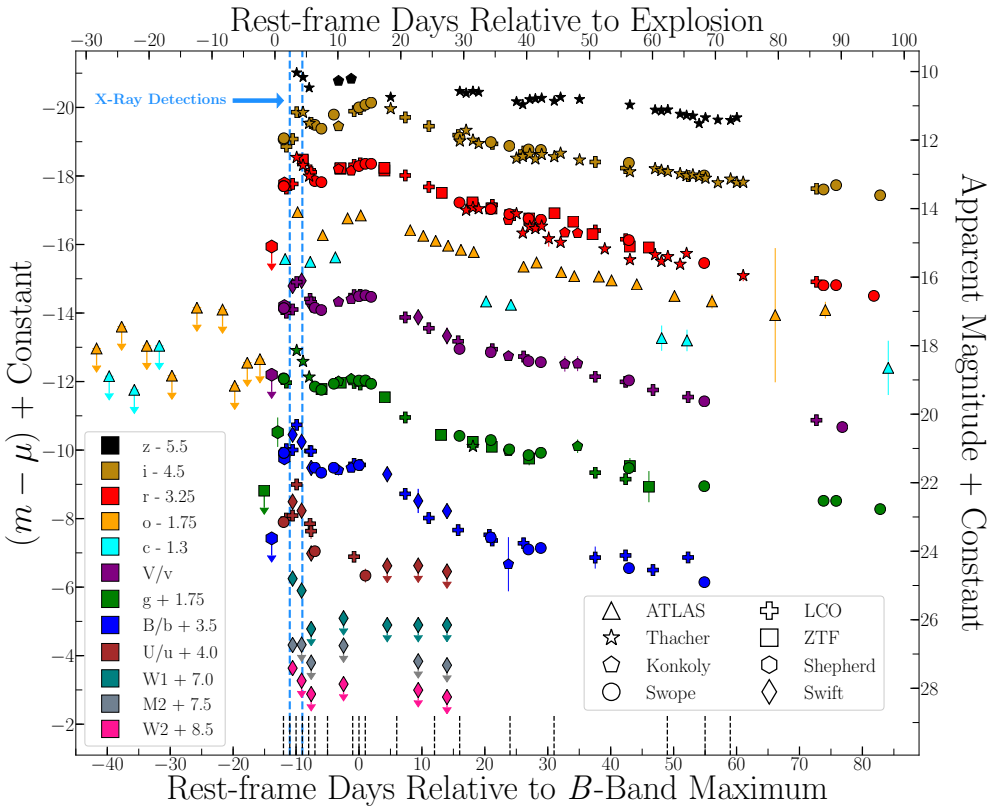

Figure 2.11 Multiwavelength light curves of SN 2019ehk, as presented in Jacobson-Galán et al. (2020b). The Swope $uBVgri$ photometry was part of a rich dataset for this object, which included the first X-ray detections for a calcium-rich transient.

The fast-decliner AT 2018cow

AT 2018cow was a fast blue optical transient whose rapid rise, early discovery, low redshift, and unprecedented properties generated much interest in the transient com-

munity. These properties included UV thermal emission, with a blackbody temperature that initially rose, then declined, and remained constant 20 days post-discovery; initial featureless spectra, followed by the emergence and disappearance of broad absorption features; the appearance of He and H lines 15 days post-discovery; and multi-wavelength emission detected in the NIR, X-ray, and radio (Ho et al. 2019; Margutti et al. 2019; Perley et al. 2019; Ho et al. 2023)..

The SSS AT 2018cow was part of a two-paper study focusing on late-time HST observations, constraining the prompt emission and its thermal properties (Chen et al. 2023a,b). The SSS data were critical to constrain the spectral energy distributions of the prompt emission, especially at the time of HST observations. In conjunction with the HST and UV photometry, these works confirmed that the fading prompt emission is blackbody (optically thick), with a high temperature and small radius, and for the first time report a break in the bolometric light curve, with a much faster decline 13 days after the explosion. The authors also disfavor radioactive decay as the dominant power source by calculating the luminosity decline and ^{56}Ni mass. While the origin of the power source is still unclear, the constraints from these works point toward an accreting central engine or an ejecta-CSM interaction (Chen et al. 2023a,b).

Other Tidal Disruption Event Observations

In addition to AT 2018hyz, SSS data contributed to five other TDE papers. SSS optical observations, in addition to other multiwavelength and spectral data, have advanced our understanding of the physical mechanism of TDEs. For example, observations of AT 2017eqx (Nicholl et al. 2019) show the first complete spectral transition

from broad hydrogen and helium features to a blueshifted helium profile at late times, and light-curve modeling suggests its origin as a complete disruption of a solar-mass star by a $\sim 10^6 M_\odot$ black hole. Additionally, extensive multiwavelength observations of TDE AT 2018dyb (X-ray, UV, and optical photometry including SSS, data and radio), plus optical spectroscopy and the first spectropolarimetric observations of a TDE, allowed close monitoring of one of the brightest and nearest TDEs to date. Its comprehensive observations allowed for detailed rise-time measurement, reasonable constraints on black hole mass and star mass, and a careful luminosity measurement, making it one of the most luminous UV/optical TDEs observed. Furthermore, the authors suggest that the UV/optical emission could be due to reprocessing of emission from the accretion disk, given the emission lines in all epochs other than around peak light, unlike other TDEs (Holoien et al. 2020).

Two further examples of novel TDE observations that used SSS data are AT 2019azh and AT 2019qiz. AT 2019azh, discovered in an extreme post-starburst galaxy, is an X-ray and UV luminous TDE, which presented an initial optical rise and roughly constant X-ray evolution and posterior slow UV and optical decline. However, after $\sim$ 225 days after the peak, its X-ray flux increased by an order of magnitude, suggesting an increase in the area of the region emitting X-rays (Hinkle et al. 2021). AT 2019qiz, with extensive SSS *ugri* data, exhibits an iron and low-ionization broad absorption line observed for the first time in a TDE from an HST spectrum. The optical data were particularly useful in modeling the spectral energy distribution and deriving the bolometric luminosity, blackbody temperature, and radius. These combined AT 2019qiz observations suggest a connection between TDEs and engine-powered SNe during their

early stages (Hung et al. 2021).

Sometimes, it is difficult to distinguish between a TDE and another type of astronomical object, such as a new type of nuclear transient. For example, optical (including SSS), X-ray, and UV observations of transient AT 2018bcb provided interesting insights: X-ray and UV observations are more consistent with blackbody emission. In contrast, optical photometry is well-fit by a power law consistent with an accretion disk. This object would be one of the most luminous and slow-declining observed TDEs, challenging the current TDE paradigm (Neustadt et al. 2020).

Other Rare Transients

SSS data has provided useful photometric data for studies of other transient types. For instance, SSS $uBVgri$ contributed to the observations of SN 2019muj, a SN Iax, a thermonuclear subclass with lower ejecta velocity and luminosities than normal SNe Ia (Li et al. 2003; Foley et al. 2013; Jha 2017). The multiple UV, optical, and NIR observations allowed physical estimation properties of the ejecta, linking extremely low-luminosity SNe Iax to brighter SNe Iax (Barna et al. 2021a). SSS optical data also contributed to the study of the nova AT 2019qyl (Jencson et al. 2021), a rapid-riser and rapid-decliner transient, with low-mass ejecta and an IR-variable counterpart. This study suggests that interactions between multiple outflow components likely produce the shock-powered emission observed in galactic recurrent novae. Finally, a study of luminous red nova (LRN) AT 2018bwo included SSS data, which helped constrain this object's peak luminosity and contributed to understanding the wide range of physical varieties of LRNe, supporting the evidence that most observational LRNe quantities

are correlated, such as peak luminosity, outburst duration, photometric radius, effective temperature, and mass of the progenitor star systems (Pastorello et al. 2022).

2.4.5 Supernova Progenitor Studies

SSS has contributed to detailed progenitor studies of different types of SNe. While a 1-m telescope does not have the capability of performing extremely deep observations to successfully image the pre-explosion counterparts of transients, it can be a very useful complement to space-based telescopes such as the HST.

For example, the progenitor source of Type Ib (hydrogen-stripped core-collapse) SN 2019yvr was identified in Kilpatrick et al. (2021a) using high-resolution HST pre-explosion images, just the second SN Ib progenitor candidate ever identified. SSS's multiband $uBVgri$ photometry (see Figure 2.12) and optical spectra were critical to infer SN 2019yvr's reddening. After correcting the pre-explosion photometry with this derived reddening value, the authors derive the pre-explosion source's luminosity, effective temperature, and radius, with the radius much larger than expected for SN Ib progenitor stars. Additionally, late-time spectra and imaging show signatures of strong CSM interaction, suggesting an eruptive mass-loss evolution.

Further examples of SSS and HST joint progenitor studies are the observations of Type IIb SN 2016gkg (Kilpatrick et al. 2022a) and Type II-P SN 2019mhm (Vazquez et al. 2023). SSS observations of SN 2016gkg in $uBVgri$ bands from around +30 to +300 days past maximum light, combined with HST observations at +652, +1698, and +1795 days, show that this object is decaying slower than expected for its ^{56}Co decay during its nebular phase. When adding the spectral data to the analysis, the

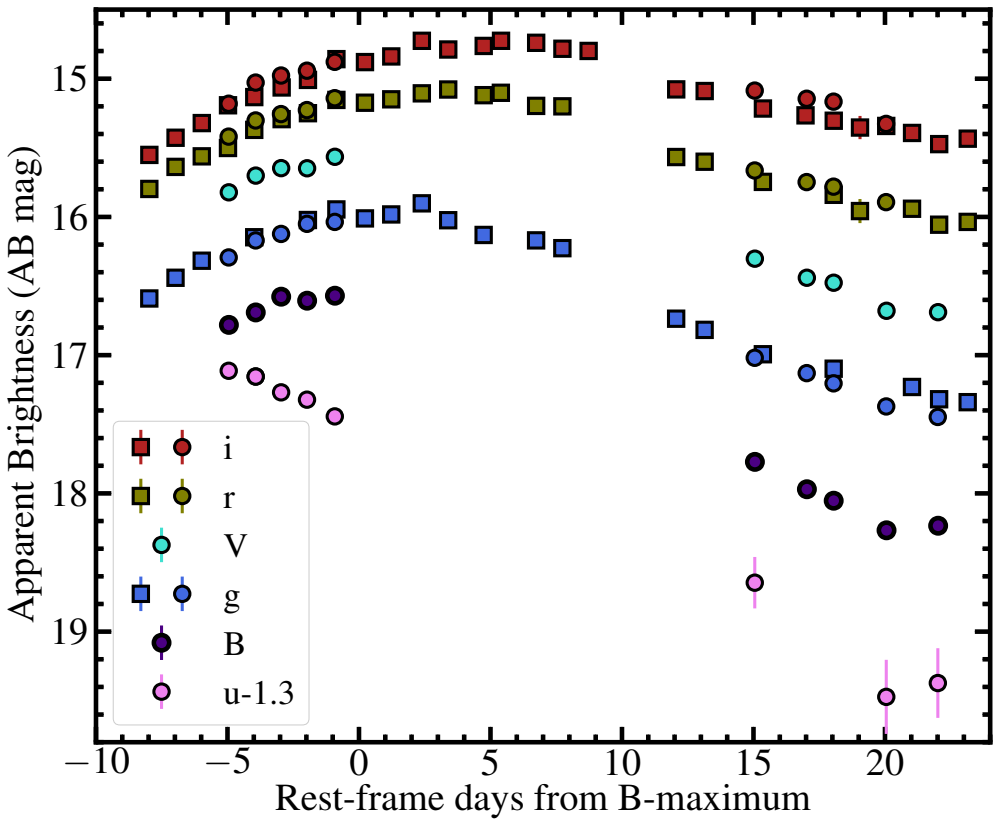

Figure 2.12 Multiwavelength light curves of SN 2019yvr, a SN Ibn with a cool progenitor, as presented in Kilpatrick et al. (2021a). The Swope $uBVgri$ photometry is marked with circles.

authors suggest that SN 2016gkg is powered mainly by interaction with CSM (Kilpatrick et al. 2022b). Additionally, detailed photometric and spectroscopic observations of SN 2019mhm (including SSS's $uBVgri$ data) identify this object as a typical Type II-P SN (core-collapse with a plateau in its light curve decline), with its ^{56}Ni inferred from the bolometric light curve. A counterpart is not detected in pre-explosion HST images, but the derived mass upper limits are consistent with other SN II-P progenitor stars (Vazquez et al. 2023).

Similarly, SSS's $uBVgri$ data (in addition to optical spectroscopy) is used to characterize SN 2017ejb as a low-luminosity SN Ia. No X-ray sources are identified in

pre-explosion *Chandra* X-ray Observatory images; however, the X-ray limits placed on potential progenitor sources indicate that low-luminosity SNe Ia, like SN 2017ejb, likely originate from low-mass white dwarfs with low pre-explosion accretion rates (Kilpatrick et al. 2018a).

2.4.6 Gravitational-Wave Counterpart Observations

SSS17a: the first joint gravitational and electromagnetic observation

The first detection of a gravitational-wave signal detected by the Laser Interferometer Gravitational-wave Observatory (LIGO) in September 2015 from the inspiral and merger of a relatively massive binary black hole (BBH) system revolutionized astronomy (Abbott et al. 2016). In contrast to black holes, merging neutron stars were anticipated to emit electromagnetic radiation, providing more information than just from the GW alone, such as constraining the exact position of the source and studying the expansion rate of the Universe (Holz & Hughes 2005; Nissanke et al. 2013). Additionally, while it is well understood that $\sim 50\%$ of elements heavier than iron are formed through rapid neutron capture nucleosynthesis (r-process), the origin of these processes has been a subject of debate, with core-collapse SNe and compact binary mergers, such as neutron-star—neutron-star systems, proposed as potential sites (Lattimer & Schramm 1974).

Two years after the first gravitational-wave detection, on August 17, 2017, LIGO and Virgo detected gravitational waves from a binary neutron star merger, GW170817 LIGO/Virgo collaboration (2017a,b). Following gamma-ray detections by the *Fermi* and INTErnational Gamma-Ray Astrophysics Laboratory (INTEGRAL)

GBM-LIGO (2017); INTEGRAL (2017) telescopes, our One-Meter, Two-Hemisphere (1M2H) collaboration started the search for a possible electromagnetic counterpart using the Swope telescope. By following the strategy described in Coulter et al. (2017) (using a catalog of nearby galaxies and prioritizing based on stellar mass and star-formation rate), our team, using the Swope telescope, detected a source not present in template images (see Figures 2.13, 2.14). Located at right ascension $13^{\rm h}09^{\rm m}48^{\rm s}.085 \pm 0.018$, declination $-23°22'53''.343 \pm 0.218$ (J2000 equinox), we designated this source as Swope Supernova Survey 2017a (SSS17a) (IAU name AT 2017gfo). This source was located $10.6''$ from the nucleus of galaxy NGC 4993, located at $z = 0.009680$ (Jones et al. 2009) or 40 Mpc (Freedman et al. 2001). My role in the discovery was the real-time image reduction (while I was physically located in my office on the UC Santa Cruz campus), which was crucial for quickly detecting SSS17a.

After follow-up observations using the Magellan telescopes, we reported this discovery through the LIGO-Virgo Collaboration (LVC) Gamma-ray Coordination Network (GCN) (One-Meter Two-Hemisphere (1M2H) collaboration 2017). By comparing these observations to Swope and Magellan images obtained 18-20 days afterward, and combined with the gravitational-wave and multiwavelength observations, this observation was the first joint electromagnetic and gravitational-wave confirmation of a kilonova (Abbott et al. 2017; Coulter et al. 2017; Drout et al. 2017a; Foley 2017; Kilpatrick et al. 2017; Murguia-Berthier et al. 2017b; Siebert et al. 2017).

By using SSS's early photometric data (see Figure 2.4.6), in combination with UV and NIR photometry, Drout et al. (2017b) were able to constrain the light-curve evolution, and fit blackbody model temperatures and radii, which are all consistent

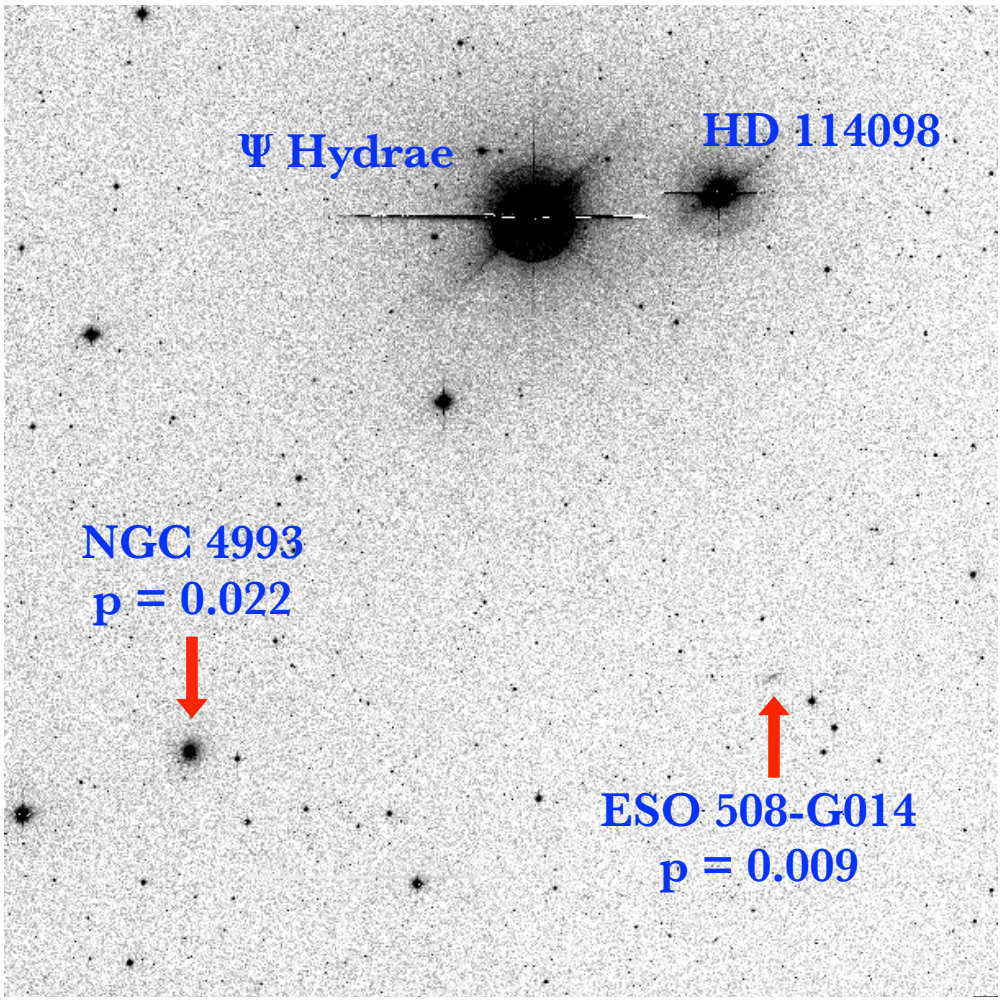

Figure 2.13 Swope telescope i-band image containing NGC 4993, the host galaxy of SSS17a. This galaxy had a 0.022 probability of hosting GW170817 (Coulter et al. 2017). From Coulter et al., SCIENCE, 16 Oct 2017 Vol 358, Issue 6370, pp. 1556-1558, DOI: 10.1126/science.aap9811. Reprinted with permission from AAAS.

with multiple ejecta components with varying lanthanide abundances. Furthermore, they estimate that at least 0.05 $M_{\odot}$ of r-process material was created in this event.

SSS17a presented unprecedented optical photometric and spectroscopic properties, such as fading and cooling faster than any other astrophysical transient, with featureless spectra during its cooling (Siebert et al. 2017; Shappee et al. 2017). Its light-

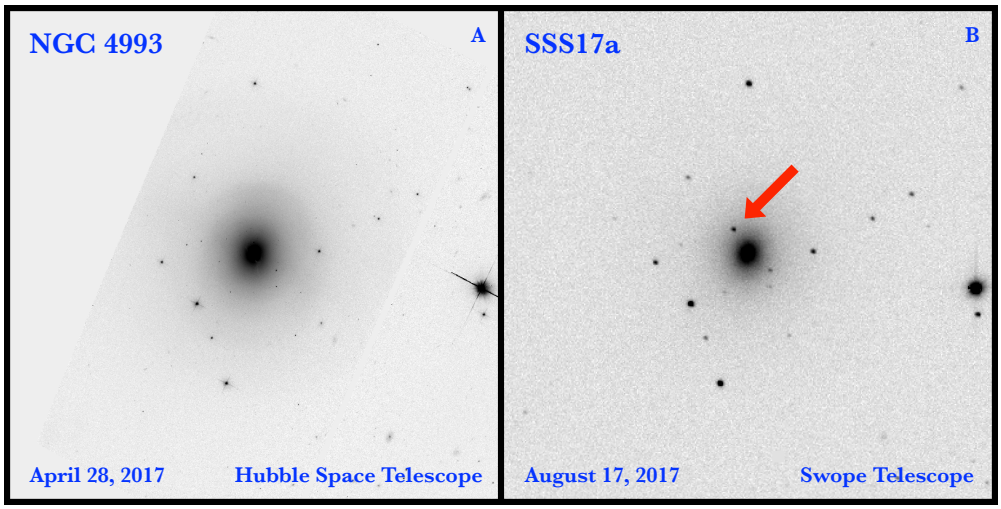

Figure 2.14 Images of NGC 4993 before and after August 17, 2017. *Left panel*: *Hubble Space Telescope* F606W-band image 4 months before GW170817 (Foley et al. 2017; Pan et al. 2017). *Right panel*: Swope image (i band) of SSS17a, obtained on August 17, 2017; SSS17a is marked with the red arrow. No object is in the left *Hubble* image at SSS17a's position (Foley et al. 2017; Pan et al. 2017). From Coulter et al., SCIENCE, 16 Oct 2017 Vol 358, Issue 6370, pp. 1556-1558, DOI: 10.1126/science.aap9811. Reprinted with permission from AAAS.

curve models match closely with compact binary system kilonova models composed of two neutron stars (Kilpatrick et al. 2021b), and in addition to the prompt γ-ray emission and gravitational-wave merger signal, are consistent with a typical, powerful short γ-ray burst seeing off-axis (Murguia-Berthier et al. 2017a). Finally, the power-law evolution of SSS17a's light curve regarding luminosity, temperature, and radius can be attributed to the cooling of shock-heated material surrounding the neutron-star merger (Piro & Kollmeier 2018).

Further Gravitational-Wave Counterpart Searches: GW190814 and GW190425

SSS17a's spectacular discovery demonstrated the SSS's capability for discovering and providing optical light curves that constrain the properties of the glowing

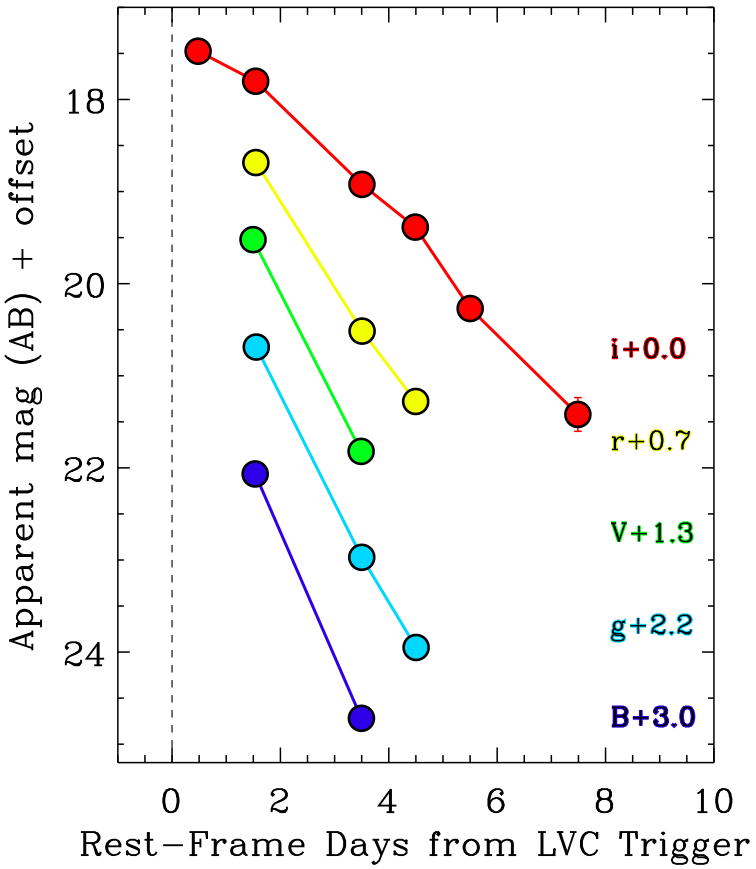

Figure 2.15 *BVgri* light curves of SSS17a (Drout et al. 2017a; Kilpatrick et al. 2017; Murguia-Berthier et al. 2017b). From Coulter et al., SCIENCE, 16 Oct 2017 Vol 358, Issue 6370, pp. 1556-1558, DOI: 10.1126/science.aap9811. Reprinted with permission from AAAS.

neutron-rich ejecta. Early-time SSS17a emissions were surprisingly blue, making it crucial to observe future counterparts promptly after the merger to understand the physical origin. The SSS has developed the tools to generate a ranked list of targets and conduct a galaxy-targeted search for GW counterparts, as was done in the search for the electromagnetic counterpart to the neutron-star—black-hole merger GW190814 (Kilpatrick et al. 2021b) and binary neutron-star merger GW190425 (Coulter et al. 2024).

These papers present optical (GW190814) and UV, optical, and IR (GW190425)

observations searching for electromagnetic counterparts, with the SSS contributing significantly. Although no EM counterparts were found in either search, limits on the r-band decline rates and the absolute magnitudes of possible counterparts were placed. SSS has played an important role in GW counterpart searches and advancing multi-messenger astronomy, paving the way for future GW counterpart detection efforts.

Chapter 3

Swope Supernova Survey Type Ia Supernova Data Release

3.1 Introduction

While the Swope Supernova Survey covers a wide variety of research topics in transient astronomy as described in Chapter 2, its main science driver, in terms of the objects observed, is SN Ia cosmology (see Figure 2.6). SNe Ia are crucial in cosmology owing to their role as standard candles and precise measurement of cosmic distances. Since the survey's first weeks in June 2016, we have continuously observed SNe Ia.

I joined the survey in July 2017 and learned the different scheduling tasks, communicating with the observers, daily operations, data reduction and uploading, and final photometry with the existing photometry code. However, in 2021, we identified an issue with the photometry reduction pipeline, requiring a complete rewrite of the photometry code. I led the detective work under the guidance of Ryan Foley and Armin

Rest to figure out the cause of the issue. Once it was determined (spatially-varying PSF across the detector), I also led the new photometry code writing, working very closely with photometry experts Armin Rest, Ryan Foley, and especially Justin Roberts-Pierel, who provided very comprehensive advice and helped with the coding and debugging (see Section 3.4). The first data release of SNe Ia was finally submitted to *MNRAS* in 2024.

In the following sections, I present the SSS SN Ia program's motivation (Section 3.2), reduction (Section 3.4) and calibration (Section 3.6) processes, present the light curves and resulting Hubble diagram (Section 3.7), and describe the future plans for the program (Section 3.8).

3.2 Motivation and Survey Advantages

Systematic effects related to the current low-redshift SN Ia sample will propagate to systematic uncertainties on measurements of w in several ways:

1. *Photometric calibration*: Low-z samples used in recent SN analyses (Scolnic et al. 2018; Jones et al. 2018b; Brout et al. 2019; Scolnic et al. 2022) are heterogenous, consisting of observations on more than 13 different photometric systems. Some of these systems cannot be better understood or calibrated, since some cameras, filters or telescopes used no longer exist (Foley et al. 2018). Efforts to combine these observations in a homogeneous way have been recently implemented (Scolnic et al. 2015; Brownsberger et al. 2021; Brout et al. 2022b).

2. *Selection effects*: Many of the low-z SN searches (particularly before 2008, such

as Li et al. 2000; Filippenko et al. 2001a) targeted bright, massive galaxies, while the high-z surveys performed untargeted observations with no preference for observations of specific galaxy types. For older surveys, it is hard to reproduce their observing choices, resulting in a large correction for selection bias and a large associated uncertainty. Given that there is an observed correlation between SN Hubble residuals and host-galaxy properties (Kelly et al. 2010; Lampeitl et al. 2010; Sullivan et al. 2010; Pan et al. 2014), biased selection strategies and the unclear connection between host-galaxy and SN properties increase systematic uncertainties on distances and resulting cosmological parameters (Jones et al. 2019).

3. *SN modeling*: SN modeling is the second largest single systematic uncertainty component in the Pantheon+ analysis (the first being redshift bias) (Brout et al. 2022a). A time-evolving, empirical SN Ia spectral energy distribution (SED) model is required to accurately standardize SNe Ia and derive SN distances. The SALT2 model (Guy et al. 2007) is a widely used spectrophotometric light-curve model for this purpose: it takes the SN Ia light curves and z as input and returns several diagnostic parameters. Recent efforts from Taylor et al. (2023) as well as the development of the SALT3 model have improved the model by recalibrating the training data and extending the wavelength range through the rest-frame z band (Kenworthy et al. 2021a; Pierel et al. 2022; Dai et al. 2023; Jones et al. 2023; Taylor et al. 2023). However, high-quality, high-cadence training data, especially in the u band, is necessary to reduce this systematic uncertainty significantly.

The need for excellent calibration makes the Swope telescope ideal owing to its wide wavelength coverage ($uBVgri$ filters, Figure 2.1). Additionally, the u band is especially useful for the SN modeling efforts, although it is not included in this work. We have a large amount of observing nights assigned per year, so we can follow many SNe to observe a sizeable fraction of the low-z Roman requirement (Spergel et al. 2015) and with a high cadence, which translates to better SN Ia distance measurements. Finally, we follow mostly SNe Ia from untargeted surveys to avoid survey biases.

Additionally, even though recent SN data releases have largely increased the amount of data at low redshift, such as the Foundation Supernova Survey (Foley et al. 2018), Pantheon+ (Scolnic et al. 2022), and the Young Supernova Experiment (Aleo et al. 2023), most of the data are still at high redshift.

Finally, the SSS builds upon the legacy of CSP[7], a SN observational program which ran from 2004-2009 (phase 1) and 2011-2015 (phase 2) at Las Campanas Observatory, Chile. CSP has precisely calibrated the Swope telescope system and observed hundreds of SNe Ia and other transients (Hamuy et al. 2006; Freedman et al. 2009; Contreras et al. 2010; Stritzinger et al. 2011; Krisciunas et al. 2017; Phillips et al. 2019; Burns et al. 2020; Uddin et al. 2023; Lu et al. 2023): we use the same telescope, and similar (CSP-I) and the same (CSP-II) optical filters. SSS will have a direct impact on the measurement of w by adding hundreds of SNe Ia on a similar photometric system as CSP, decreasing the current photometric calibration uncertainties (Brout et al. 2022a), and providing a unique sample for modern SN Ia analyses with significant legacy value.

[7] https://csp.obs.carnegiescience.edu/

3.3 Swope Supernova Survey Type Ia Supernova Observations

We have observed 342 SNe Ia as of March 2024, 216 of which have full template observations. Since we currently tie our photometry to Pan-STARRS1 (PS1; see below), we only include SNe Ia within its survey area, corresponding to a declination $\geq -30°$. This limitation results in a further reduction of SNe in our current data release, but will be part of a future data release. Ultimately, we present 111 SNe Ia in DR1. In Fig. 3.1, we compare the mean number of observations per SN, and the total number of SN Ia observed in several low-z surveys. The total number of SNe from the Swope Supernova Survey (SSS DR1 red pentagon) will increase significantly with the second data release (red hexagon). Further work will combine the SSS data with the CSP-I data (blue hexagon).

Figure 3.2 shows a false-color image of SN 2018gv, with *irB* filters mapped to the RGB color channels. This image represents a typical observation from our survey, although we only use one amplifier (one-quarter of the entire image) in our data processing, following CSP-I (Krisciunas et al. 2017).

In Figure 3.3, we show the number of observations in the i-band of all the SNe Ia in SSS DR1. With a median of 10 i-band observations per SN, we ensure we obtain good light-curve coverage of most targets. Additionally, in Figure 3.4, we display the phase of the first observation of all the SNe in SSS DR1. In the first year of the survey, most of the first observations were post B-band peak since we were mainly following SNe observed by other surveys for comparison purposes (Foley et al. 2018).

However, after I joined the survey in mid-2017, I prioritized obtaining pre-B-band peak observations for all SNe.

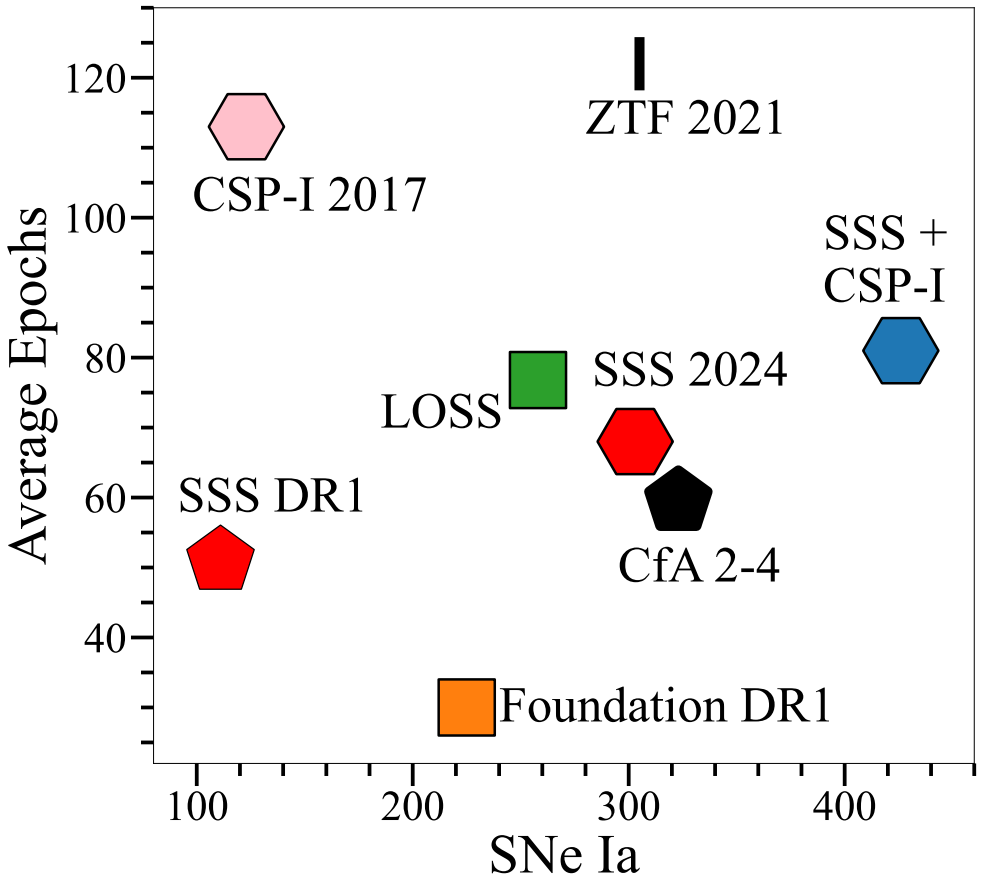

Figure 3.1 Comparison of optical low-redshift SN Ia surveys, displaying the number of SNe observed, the cadence of observations, and the number of filters used (indicated by the number of sides for a given data point; e.g., a pentagon indicates five filters). The SSS DR1 (this work; displayed as the red pentagon) has observed 111 SNe Ia in five filters (*BVgri*) with an average of 51 observations per SN. The red hexagon shows the status of SSS as of March 2024. The expanded sample includes the additional u band. The pink hexagon, orange square, green square, black line, and black hexagon represent data releases from the CSP (Krisciunas et al. 2017), Foundation Supernova Survey (Foley et al. 2018), Lick Observatory Supernova Search (Ganeshalingam et al. 2010; Stahl et al. 2019), Zwicky Transient Facility (Dhawan et al. 2022), and Center for Astrophysics (Jha et al. 2006; Hicken et al. 2009, 2012) samples, respectively. We present the combined CSP and SSS sample as a blue hexagon.

Table 3.1. SNe Ia in SSS DR1

SN	Discovery Survey Name	Host Galaxy	Discovery Reference[1]	Classification Reference[2]	Subclass
2016cvn	ATLAS16bdg	NGC 4708	TNS 2734 ATEL 9151	ATEL 9165	
2016cxb	PS16cvc	GALEXASC J211223.05+144644.9	TNS 2783 ATEL 9174	TNS 279 ATEL 9182	
2016cyt		NGC 7033	TNS 2828	ATEL 9210 TEL 9210	
2016eky	PS16dnp	WISEA J225937.41+020909.4	TNS 3912 ATEL 9302	TNS 308 ATEL 9297	
2016fff	ASASSN-16jf	UGCA 430	TNS 4498 ATEL 9398	TNS 348 ATEL 9405	
2016gsn	ASASSN-16la	2MASXi J0229172+180515	TNS 5615 ATEL 9571	TNS 467 ATEL 9581	
2016ije		SDSS J015830.25+125528.1	TNS 6944	TNS 585 ATEL 9790	91bg
2016ivt	ATLAS16dzg	SDSS J113502.19+082825.3	TNS 7315	TNS 647 ATEL 9873	
2016ixb	ASASSN-16ov		TNS 7357 ATEL 9875	TNS 654 ATEL 9878	
2016iyv	ASASSN-16oz	GALEXASC J090013.19-133803.5	TNS 7405 ATEL 9887	TNS 665 ATEL 9889	91T
2016jbs	Gaia16cfp	MCG -02-24-017	TNS 7489 TNS 7489	TNS 678 TEL 9913	
2017aaa	PS17akj	LCRS B134713.8-024957	TNS 8450	TNS 777 ATEL 10056	
2017aac	PS17ajt	2MASX J08103080+0515368	TNS 8452	TNS 778 ATEL 10056	
2017adj	ATLAS17axb	GALEXASC J134322.97-195637.5	TNS 8548	TNS 781 ATEL 10056	
2017cal	ASASSN-17dh	NGC 6321	TNS 9957 ATEL 10156	TNS 840 ATEL 10159	
2017cfc	ATLAS17cog	UGC 08783	TNS 10092	TNS 869 ATEL 10212	
2017cne	PTSS-17ntl	SDSS J150842.78+040846.9	TNS 10336	TNS 885 ATEL 10234	91T
2017cpu	ASASSN-17ej	SDSS J140752.70+093828.5	TNS 10416 ATEL 10241	TNS 886	
2017djl	ATLAS17exo	LEDA 83608	TNS 11014	TNS 968 ATEL 10334	
2017drh	DLT17aw	NGC 6384	TNS 11243 ATEL 10343	TNS 990 ATEL 10345	
2017dys	ASASSN-17gb	2MASX J23050199-2638071	TNS 11446 ATEL 10370	ATEL 10375 ATEL 10375	
2017erp		NGC 5861	TNS 12021	TNS 1041 ATEL 10490	
2017euz	ATLAS17hdh	GALEXASC J194112.34-233001.7	TNS 12123	TNS 1053 TEL 10525	91T?
2017evc	ATLAS17hdo	2MASX J21175062-2506262	TNS 12126	TNS 1054 ATEL 10525	91T
2017fgc	DLT17bx	NGC 474	TNS 12450 ATEL 10569	TNS 1084 ATEL 10570	
2017fms		IC 1371	TNS 12635	TNS 1099 ATEL 10582	
2017fmz	ATLAS17ipa	CGCG 377-011	TNS 12642	ATEL 10582	
2017fnz	ATLAS17ite	GALEXASC J222942.86+114818.1	TNS 12670	TNS 1462	

Table 3.1 (cont'd)

SN	Discovery Survey Name	Host Galaxy	Discovery Reference[1]	Classification Reference[2]	Subclass
				ATEL 10593	
2017fzw	DLT17cd	NGC 2217	TNS 13029	TNS 1105	91bg
			ATEL 10629	ATEL 10639	
2017gdg	ATLAS17jnn	LEDA 3253279	TNS 13127	TNS 1134	
				ATEL 10657	
2017gfa	PS17egq	LEDA 771483	TNS 13180	TNS 1135	
				ATEL 10657	
2017gfl	ATLAS17jof	LEDA 769205	TNS 13192	TNS 1140	
				ATEL 10659	
2017gjd	ASASSN-17lj	2MASX J20034478-2759181	TNS 13293	TNS 1187	
			ATEL 10695	ATEL 10689	
2017glb	ASASSN-17ll	2MASX J04512765-1657381	TNS 13349	TNS 1195	
			ATEL 10695		
2017gvp	ASASSN-17ms	UGC 12739	TNS 13716	TNS 1235	
			ATEL 10796	ATEL 10782	
2017gwy		UGC 12017	TNS 13756	TNS 1240	
				ATEL 10793	
2017hdv	ATLAS17lxk	LEDA 966359	TNS 13967	TNS 1274	
2017hfv	ASASSN-17nf	CGCG 087-028	TNS 14028	TNS 1305	
			ATEL 10883		
2017hhi	ATLAS17mag	GALEXASC J222201.94-260957.8	TNS 14076	TNS 1314	02cs
2017hmf	ATLAS17mlj	GALEXASC J214438.86+070131.8	TNS 14208	TNS 1339	
2017hoo	ATLAS17mrn	GALEXASC J032955.28-181741.7	TNS 14274	TNS 1364	
2017hou		UGC 2969	TNS 14280	TNS 1346	
2017hpa		UGC 3122	TNS 14288	TNS 1362	
				ATEL 10896	
2017hpj	ASASSN-17nz	MCG -03-60-023	TNS 14301	TNS 1368	
			ATEL 10897	ATEL 10906	
2017hqc	PTSS-17ygs	GALEXASC J232308.47+103844.5	TNS 14324	TNS 1367	
				ATEL 10904	
2017htb	ASASSN-17oc	KUG 2207+174	TNS 14413	TNS 1392	91T
			ATEL 10930	ATEL 10933	
2017hxc	ASASSN-17og	2MASX J22065211-0557073	TNS 14532	TNS 1414	
			ATEL 10960	ATEL 10966	
2017hxo	PTSS-17zfr	2MASX J03024953+0529054	TNS 14546	TNS 1403	91T
				ATEL 10954	
2017hyx	ASASSN-17or	2MASX J04470897-1620433	TNS 14581	TNS 1419	
			ATEL 10967	ATEL 10963,10964	
2017ilf	ASASSN-17pp	NGC 2803	TNS 14940	TNS 1481	
			ATEL 11018,11344	ATEL 11009,11012	
2017iln	ATLAS17njg	2MASS J03352437+0605244	TNS 14948	TNS 1470	
				ATEL 11007	
2017isj	ASASSN-17qg	UGC 6216	TNS 15179	TNS 1500	
			ATEL 11035	ATEL 11032	
2017itv	Gaia17deh	2MASX J04404501-2755038	TNS 15226	ATEL 11051	91T
				ATEL 11051	
2017iws	PS17fim	SDSS J084241.66+135806.3	TNS 15319	TNS 1512	
			ATEL 11218	TEL 11055	
2017iye	ATLAS17nsd	2MASX J10070053-1416102	TNS 15360	TNS 1561	
				ATEL 11084	
2017jgi	PS17fkc	SDSS J090157.95+134645.5	TNS 15602	ATEL 11217	
			ATEL 11218,11344	ATEL 11217	
2017lb	Gaia17adz	2MASX J10124957-1806506	TNS 8004	TNS 722	
				ATEL 9980	

Table 3.1 (cont'd)

SN	Discovery Survey Name	Host Galaxy	Discovery Reference[1]	Classification Reference[2]	Subclass
2017lc	Gaia17aea	Anonymous	TNS 8005	TNS 732 ATEL 9990	
2017nk	ASASSN-17bd	2MASX J15591858+1336487	TNS 8070 ATEL 10000	ATEL 10014	91T?
2017ux	ATLAS17apl	2MASX J09225310-0312502	TNS 8295	TNS 769 ATEL 10053	
2017yk	ATLAS17asj	2MASX J09443215-1218233	TNS 8404	ATEL 10032	
2017yn	ATLAS17asm	2MASS J11323796-2503316	TNS 8407	TNS 770 ATEL 10053	
2018aay	ASASSN-18et	LCRS B103002.1-022549	TNS 17145 ATEL 11391	TNS 1766 ATEL 11383	
2018abz	ATLAS18mit	LCRS B101737.6-062228	TNS 17180	TNS 1773 ATEL 11388	
2018ael	PS18oa	GALEXASC J131605.19-140324.4	TNS 17259	TNS 178 ATEL 11463	
2018agk	PS18mr	IC 855	TNS 17323 ATEL 11663	TNS 1858 ATEL 11433,11551	
2018aoz	DLT18q	NGC 3923	TNS 17594 ATEL 11496	TNS 1823 ATEL 11496	
2018aqh	ATLAS18myy	NGC 4090	TNS 17629	TNS 1841 ATEL 11516	
2018bfr	ASASSN-18jp	2MASX J11044706-1538068	TNS 18182 ATEL 11653	TNS 1993 ATEL 11622	
2018bfs	C17-0117	PSO J133433.574-132547.914	TNS 18183	TNS 1988 ATEL 11616,11642	
2018bgz	SNhunt374	UGC 09544	TNS 18224	TNS 2016	
2018bq	ASASSN-18ac	LCRS B110329.3-121524	TNS 16331 ATEL 11145	TNS 1615 ATEL 11154	
2018bs	ASASSN-18af	2MASX J03232113-2207024	TNS 16333 ATEL 11178	TNS 1633 ATEL 11170	
2018bsn		SDSS J145728.17+055038.05	TNS 18640	TNS 2032 ATEL 11651	
2018cjy	ATLAS18qlv	AM 1257-251	TNS 19294	TNS 2151 ATEL 11731	
2018cqw	ASASSN-18na	CGCG 113-034	TNS 19552 ATEL 11764	TNS 2154	
2018feb	ZTF18abmxahs	CGCG 139-041	TNS 21697	TNS 2556 ATEL 11969,11987	
2018ghb	ASASSN-18vm	ESO 427- G 022	TNS 22634 ATEL 12063	TNS 2730 ATEL 12040	
2018gl	ASASSN-18an	NGC 3070	TNS 16486 ATEL 11178	TNS 1641 ATEL 11169	86G,06bt
2018gv		NGC 2525	TNS 16498	TNS 1643 ATEL 11175,11177	
2018hfp	ASASSN-18xm	MCG -03-53-015	TNS 23443 ATEL 12112	TNS 2892 ATEL 12110	
2018hfr	ASASSN-18xn	2MASX J09305509-0434173	TNS 23446 ATEL 12112	TNS 2891 ATEL 12107	91T
2018hhn		UGC 12222	TNS 23507	TNS 2896	
2018how	ATLAS18xzc	GALEXASC J232612.68-254424.6	TNS 23763	TNS 2923 ATEL 12144	
2018hzx	ATLAS18ykt	2MASX J01083884+2004454	TNS 24164	TNS 2995 ATEL 12213	
2018ilu	ATLAS18zek	SDSS J233317.83+044710.2	TNS 24960	TNS 3033	

Table 3.1 (cont'd)

SN	Discovery Survey Name	Host Galaxy	Discovery Reference[1]	Classification Reference[2]	Subclass
				ATEL 12216,12286	
2018jeo	ASASSN-18aai	ESO 564- G 014	TNS 25684	TNS 3112	
			ATEL 12249		
2018kav	ATLAS18bbvc	LEDA 874406	TNS 26534	TNS 3286	
2018km	Gaia18agl	2MASX J03161380-1500449	TNS 16624	TNS 1672	
2018oh	ASASSN-18bt	UGC 4780	TNS 16751	TNS 1682	
			ATEL 11253,11344	ATEL 11267	
2018ph		IC 2231	TNS 16784	1691, ATEL 11265	
2018tt	ASASSN-18co	2MASX J09542381-1439215	TNS 16913	TNS 1738	
			ATEL 11308	ATEL 11315	
2019aox	Gaia19amg	MCG -01-11-007	TNS 29711	TNS 3526	
				ATEL 12500	
2019bka	ASASSN-19ea	ABELL 1367:[GP82] 0726	TNS 30412	TNS 3567	91T
			ATEL 12547	ATEL 12546	
2019cpe	ZTF19aanonjt	2MASX J09501327-1401298	TNS 31771	TNS 3763	
2019dfa	ATLAS19gcr	IC 0582	TNS 32740	TNS 3853	
2019dwq	ZTF19aarnqzw	IC 1073	TNS 33527	TNS 3945	
2019fzm	ASASSN-19nn	CGCG 020-034	TNS 35864	TNS 4169	
			ATEL 12819	ATEL 12828	
2019gbx	ATLAS19ltg	MCG -02-33-017	TNS 35946	TNS 4150	
				ATEL 12823	
2019gcw	ZTF19aavrswr	SDSS J151636.35+070346.1	TNS 36003	TNS 4185	
2019gf	ATLAS19adv	SDSS J080535.52-093449	TNS 28169	TNS 3396	91 T
				ATEL 12371	
2019jf	ATLAS19aew	2MASX J08361402-0521041	TNS 28312	TNS 3397	
				ATEL 12371	
2019kcx	ATLAS19oif	CGCG 013-107	TNS 40479	TNS 4455	
				ATEL 12908	
2019lqv	ZTF19abhpvfq	ESO 530- G 053	TNS 42282	TNS 4639	
2019lrc	ATLAS19pmc	CGCG 378-007	TNS 42290	TNS 4632	
				AstroNote 2019-50	
2019nhy	ZTF19abornyn	GALEXASC J174643.48+230156.0	TNS 43800	TNS 4818	
2019ons	ZTF19abrsssx	MCG -03-55-010	TNS 45044	TNS 4870	
				ATEL 13043	
2019teo	ATLAS19ynv	SDSS J221926.08-072956.6	TNS 50050	TNS 5354	
				AstroNote 2019-110	
2019vju	ATLAS19bbmr	NGC 3514	TNS 53208	TNS 5618	
2019vnj	ASASSN-19abq	LEDA 922031	TNS 53370	TNS 5597	
			ATEL 13323	ATEL 13313	
2020dhj	ZTF20aaqshoz	SDSS J145330.02+171728.5	TNS 62710	TNS 6298	

[1]TNS numbers correspond to Astronomical Transient Reports

[2]TNS numbers correspond to Classification Reports

Note. — SNe Ia in SSS DR1. Discovery and classification information is noted, as well as the SN Ia subtype, if any.

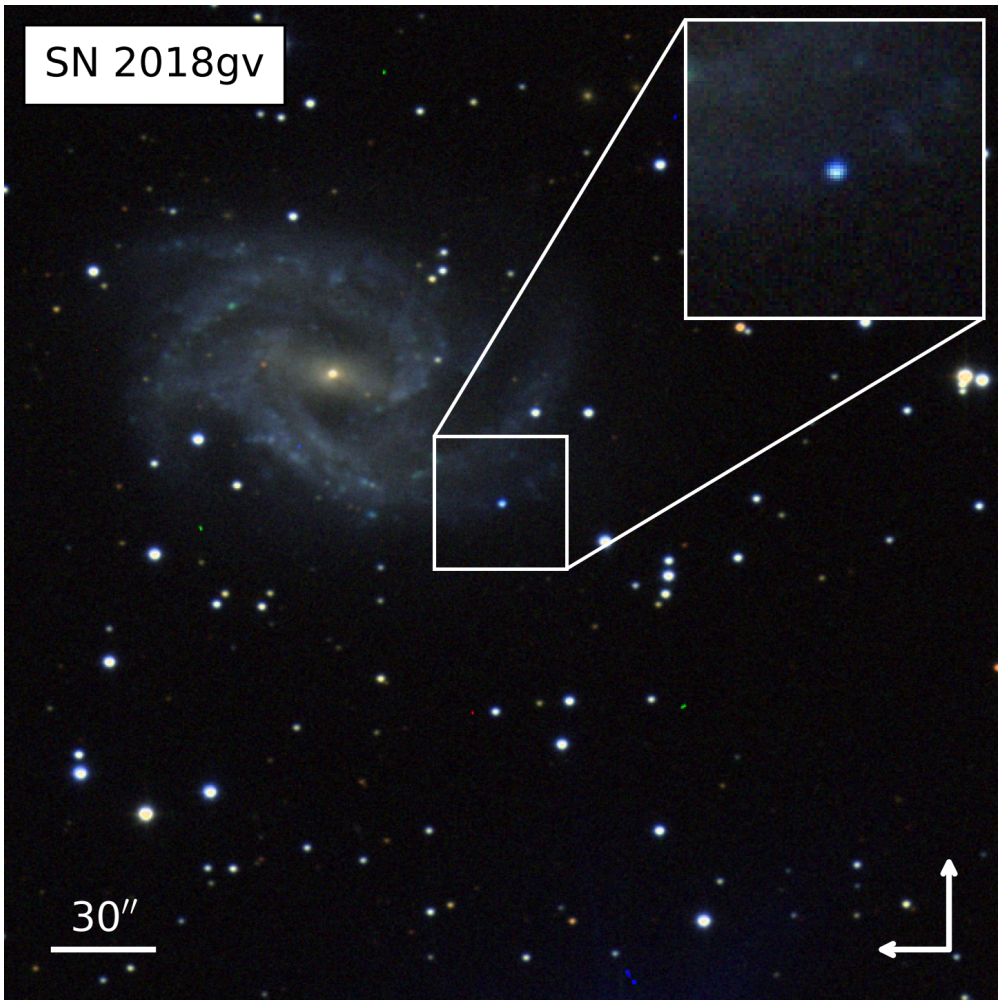

Figure 3.2 False-color image of SN 2018gv, with irB filters mapped to the RGB color channels. The image is $5' \times 5'$ with North up and East to the left. The SN is at the center of the image and the corresponding zoomed-in inset. This image is typical of our observations (although the SN is particularly close), but is only a fraction of the reduced $14.848' \times 15.132'$ image (one amplifier), which is only one quarter of the entire image.

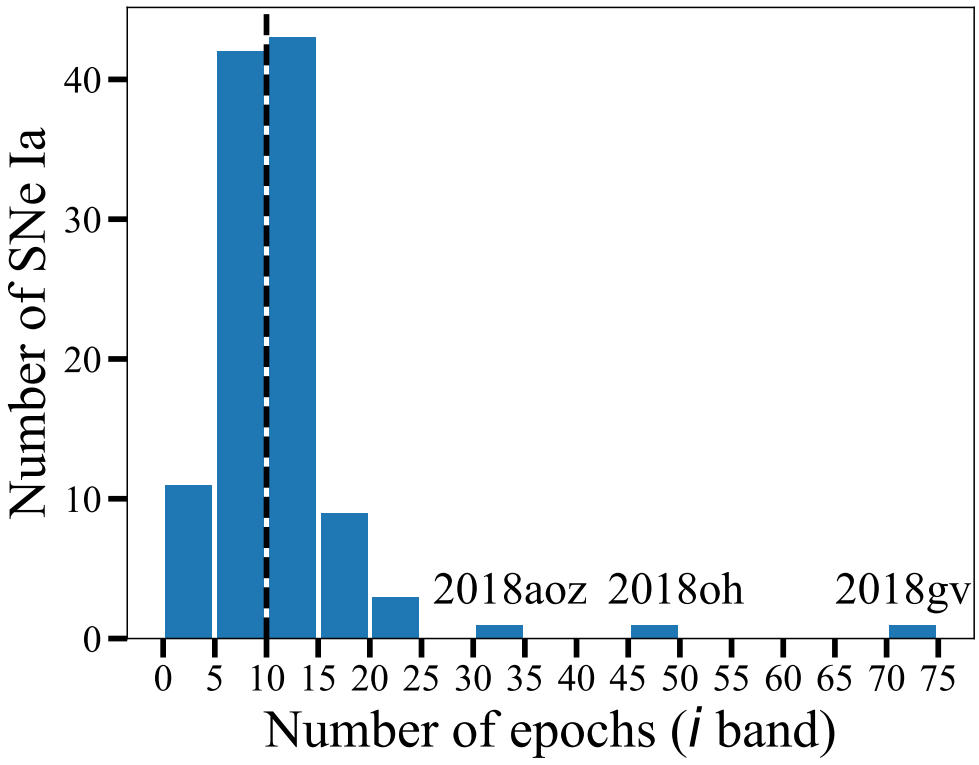

Figure 3.3 Histogram of the number of epochs for each DR1 SN Ia in the i band. The median number of epochs is 10 (dashed line). We highlight SNe 2018gv, 2018oh (Dimitriadis et al. 2019a; Li et al. 2019), and 2018aoz, which have 76, 43, and 34 epochs, respectively.

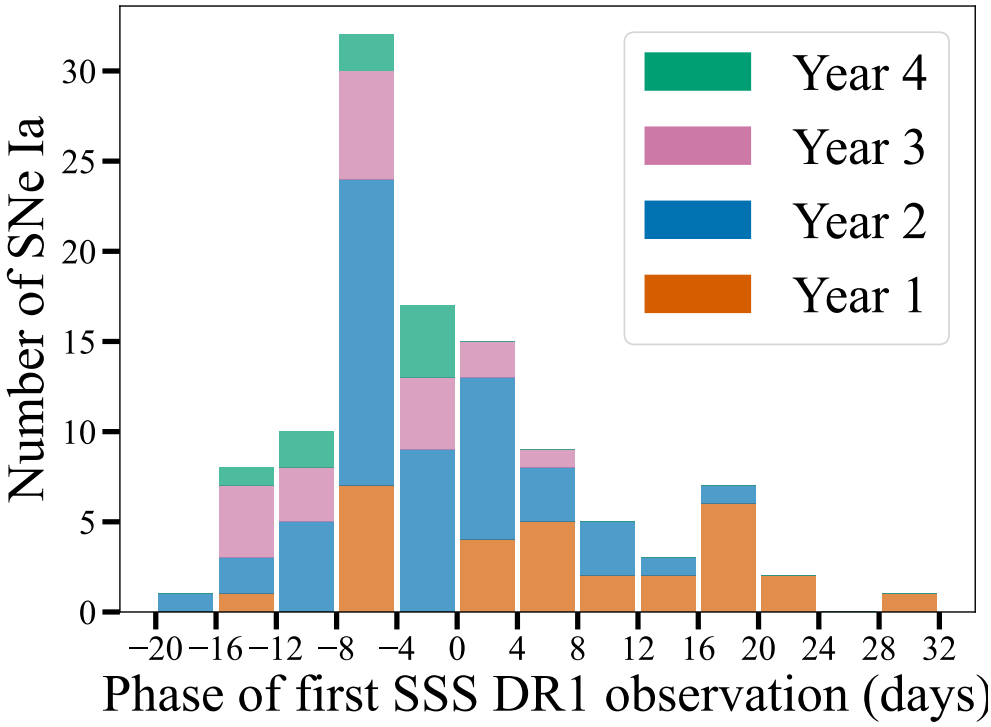

Figure 3.4 Phase of first observation from B-band maximum light for all the SNe Ia in SSS DR1. The SN Ia with the earliest phase of the first observation is SN 2018gv (-16 days). For SSS DR1, 65% of the SNe Ia were observed before peak and 21% were first observed $\geq$7 days before peak. Most of the SNe Ia with first observations starting $\geq$10 days post-peak happened during the first year of the survey or were followed for particular projects (such as K2 SNe Ia) and selected using different criteria from those listed in Section 2.3.4.

3.4 Photometric Data Reduction

The Swope detector and camera are described in Section 2.2. All SSS photometric data are reduced with the `photpipe` imaging and photometry package (Rest et al. 2005, 2014), which performs the standard bias-subtraction, flat-field correction (using calibration frames from the same night when possible), and astrometric solution. The detector is noticeably nonlinear, even at relatively low count levels. We determine the nonlinearity and correct for it, following a similar procedure to that of CSP-II[8]. Additionally, we correct for the differential exposure time across the field of view caused by the camera's iris-style shutter (Figure 3.5). Geometric distortion corrections are applied with `IRAF` (Tody 1986) using the TNX World Coordinate System (WCS)[9] convention with fourth-order distortion terms (Calabretta & Greisen 2002). Image deprojection is done with `SWarp` (Bertin et al. 2002). We then perform initial photometry with the method described in detail below. The photometric calibration is done by using PS1 secondary standard stars transformed into the Swope natural system by determining a linear transformation to correct PS1 magnitudes as a function of PS1 colors (similar to Scolnic et al. 2015; Brout et al. 2022b). From this, we determine the zero point of each image (see Section 3.6, Scolnic et al. 2015).

Once we obtain template observations for each SN and vet them according to the procedure described in Section 2.3.4 we use `HOTPANTS` (Becker 2015) to convolve and subtract the template image from the science image, producing a difference image. We finally perform forced photometry with the method described below, using the weighted

[8] http://csp2.lco.cl/manuals/swo_nc_linearity.php
[9] https://fits.gsfc.nasa.gov/fits_wcs.html

centroid position of the SN across all our images.

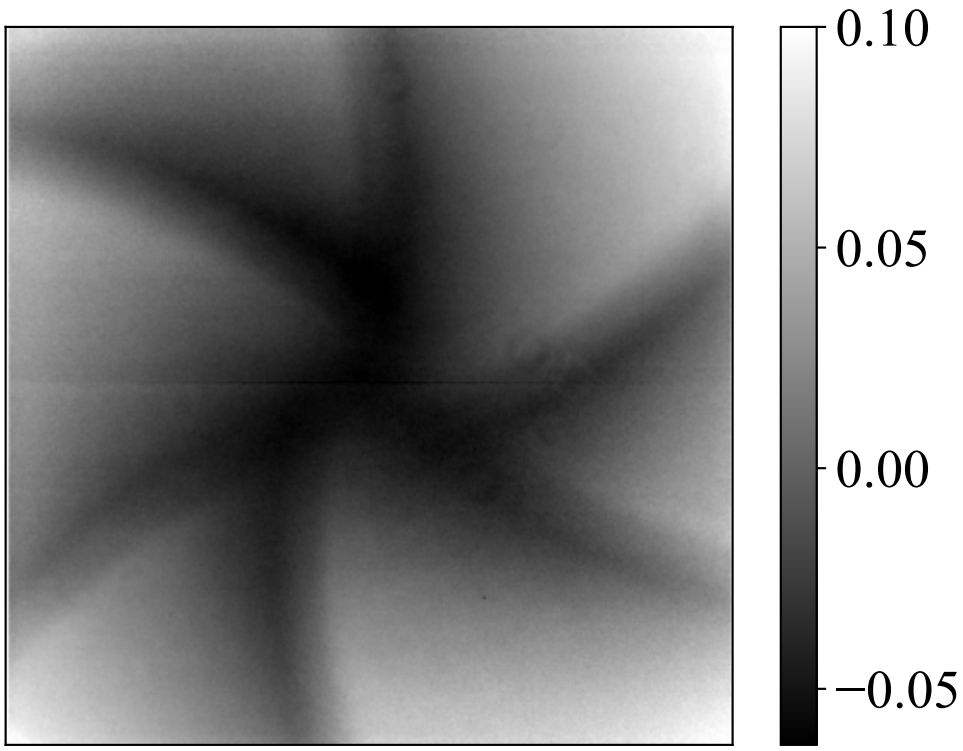

Figure 3.5 A map of the relative exposure time for a given pixel on the entire Swope detector. This was constructed by taking several dome flats with consistent intensity and different exposure times. Since the camera has an iris shutter, pixels near the center of the image are illuminated for longer than pixels near the edge of the detector. This distinctive pattern is a reflection of the iris's mechanical design. This map is used to correct the count rate for each image.

To initially test the photometric precision, we measure the photometry of stars in each image using the fixed point-spread function (PSF) photometry code, `DoPHOT` (Schechter et al. 1993). `DoPHOT` calculates an "extendedness" parameter, which is a measure of the size of an object relative to the PSF and is often used to separate stars from galaxies. We find that the extendedness of stars from `DoPHOT` fits in Swope images correlates strongly with the star's position on the detector (Figure 3.7). We interpret this resulting from a significantly varying PSF across the detector. We also find that the

residuals between Swope and PS1 photometry are highly correlated with extendedness (Figure 3.8). As a result, we have attempted to model the PSF as a function of detector position when performing photometry. As `DoPHOT` is not currently capable of using a varying PSF, we explored alternative photometry routines.

We developed a method to build an effective PSF (ePSF; Anderson & King 2000; Anderson 2016) in different locations using `Astropy`'s `photutils` (Bradley et al. 2024) photometry package. We aim to divide the detector into a grid: We set a threshold per grid cell of N stars (25 in this work) to build the ePSF and divide the detector into as many grid cells as possible.

To select stars to build the ePSF, we first run `SExtractor` (Bertin & Arnouts 1996) on the Swope images and remove any stars with neighboring sources within 15 pixels that have a flux $\geq$5% that of the primary star's flux or a magnitude that is $\leq$4 mag below that of the primary star. We only select bright stars with no chance of saturation and far from any possibility of Malmquist bias ($14 \leq m \leq 18$ mag). Next, we compute roundness and sharpness values with `DAOFIND` (Stetson 1987) as implemented in `photutils` for all the remaining possible PSF stars and perform a three-sigma clipping to remove outliers. Next, we use `photutils` to remove stars with additional sources in the PSF cutout using a 50-sigma threshold, to avoid contamination of the PSF building. Finally, we remove stars near invalid regions or borders.

After performing all these selection criteria, we create an ePSF for each cell with the PSF stars selected; we then interpolate the ePSFs across the different cells with an inverse-squared distance algorithm to each star. SN fields with insufficient PSF stars to apply this method will be published in an upcoming release with an alternative

photometry method.

As an example, Figure 3.6 displays the residuals between a fixed PSF and a spatially varying PSF calculated for 16 cells. One can see strong positive and negative residuals near the center of the PSF as well as differences in the extended structure depending on the cell.

Finally, for each SN, we calculate its weighted average position across all bands and apply the ePSF to this position through the `photutils` photometry package, thus obtaining forced photometry at the SN position.

Following CSP (Krisciunas et al. 2017), we only apply this method to amplifier 3, on which the SNe were observed. We find a consistent decrease in root-mean square (RMS) with the spatial-varying PSF method, up to 31% with respect to a non-spatial-varying PSF. In a subsequent data release, we will apply this method to the entire image, increasing the number of stars available to determine the PSF, likely improving the model ePSF. We note that this photometry method could be applied to any telescope.

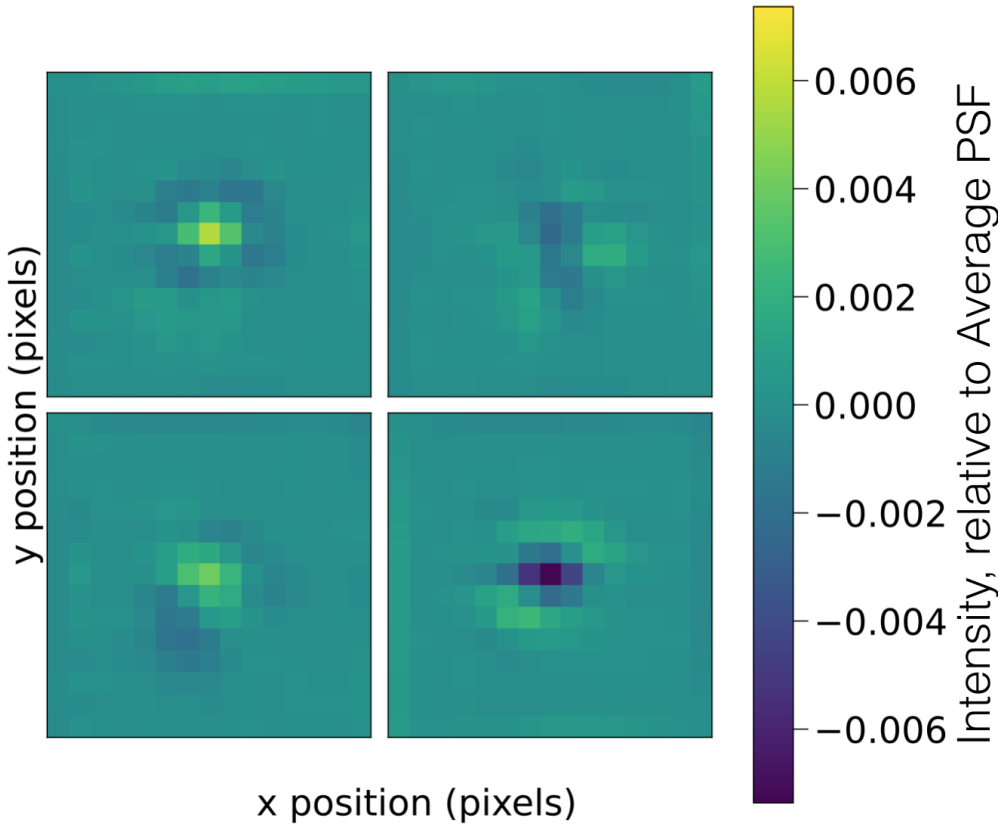

Figure 3.6 Residuals of the fitted ePSF for each sector in a 2×2 grid for amplifier 3 in a single image relative to the PSF generated for the entire amplifier 3. Even within a single amplifier, the PSF changes across the detector are noticeable.

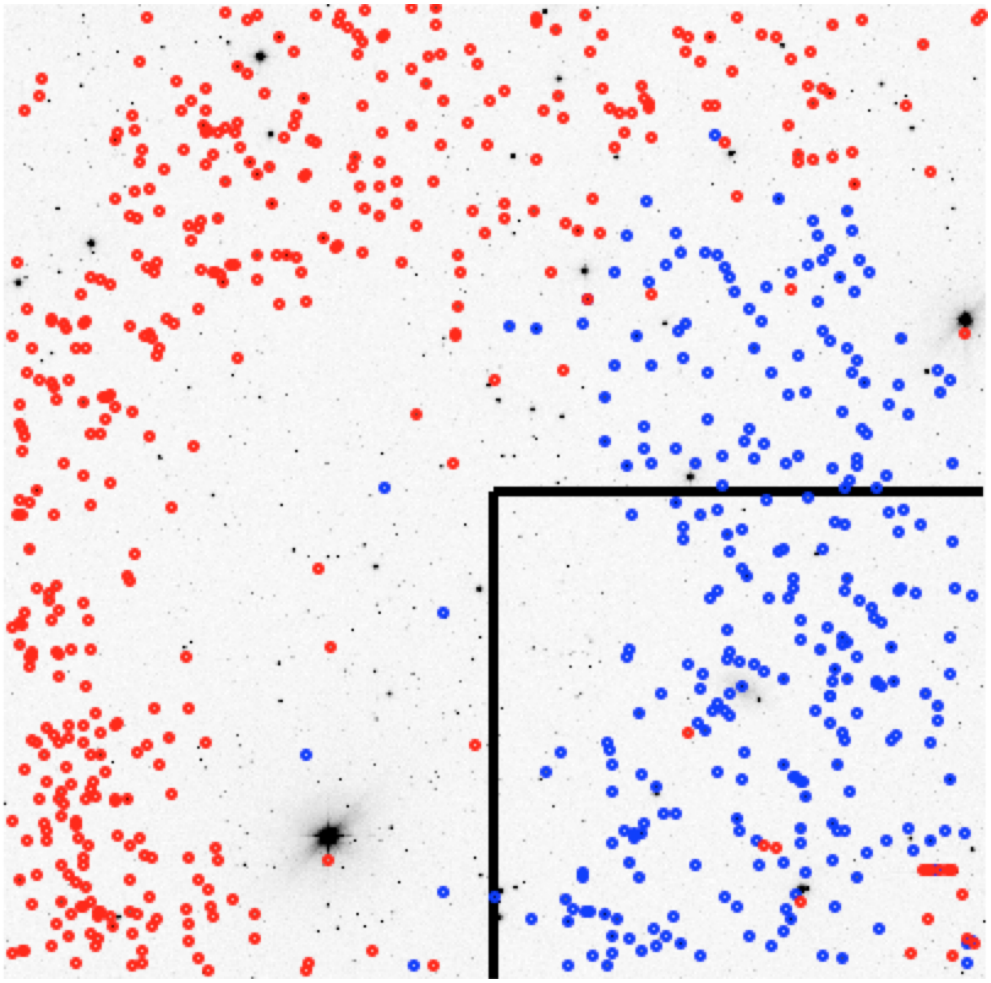

Figure 3.7 Swope g-band image, displaying all four amplifiers. Amplifier 3, where the SNe are placed and the focus of this work, is outlined in black. We have marked all stars with `DoPHOT` extendedness of >25 (<-25) as red (blue) circles. The spatial clustering of stars with similar extendedness suggests strong PSF variations across the Swope detector.

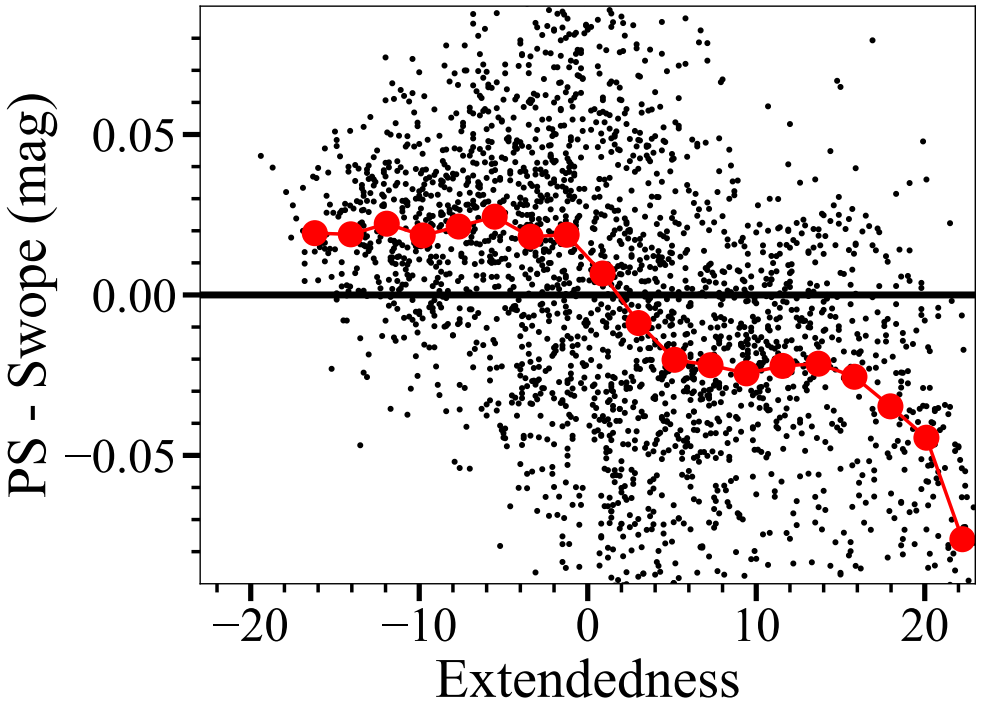

Figure 3.8 Residuals between Swope `DoPhot` and PS1 photometry as a function of `DoPhot` extendedness for a single i-band Swope image. The Swope zeropoint is derived by these data, and thus the average residual is close to zero by design. The black points represent individual stars while the red points represent the mean residual in different extendedness bins. There is a strong trend where stars with negative (positive) extendedness have positive (negative) photometric residuals.

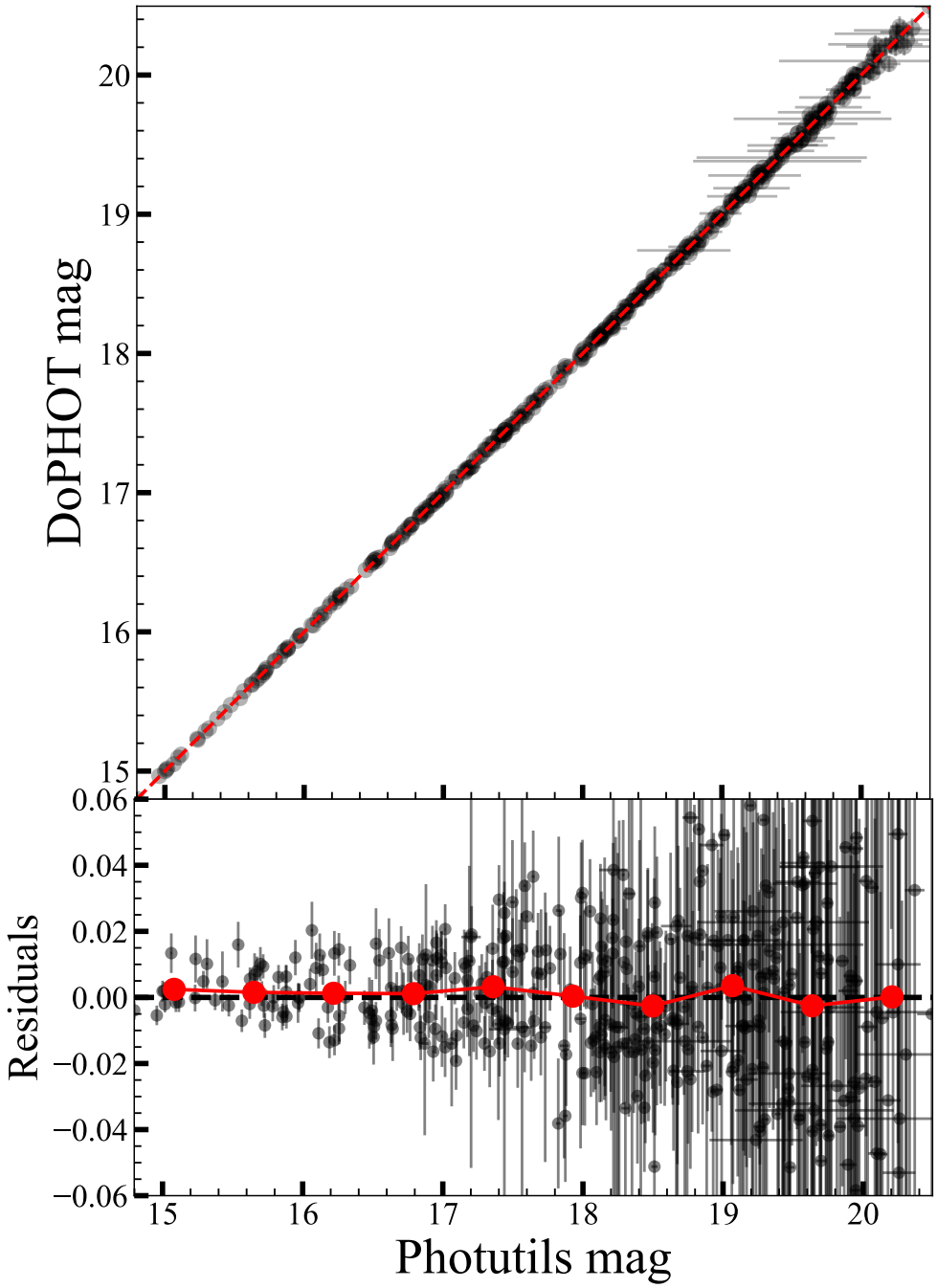

Figure 3.9 Fixed PSF star photometry(`DoPHOT`) vs spatially-varying PSF star photometry (`photutils`) for amplifier 3 of an example Swope field in i band (top panel), with the dashed line showing a one-to-one comparison, and residuals with the mean binned values in the bottom panel. We divide amplifier 3 into four equal cells, calculate the ePSF in each, and interpolate. The RMS with PS1 mags decreases from 0.019 (`DoPHOT`) to 0.013 (`photutils` ePSF) in this example Swope field, an RMS decrease of 31% by accounting for the strong PSF variation across the Swope detector.

3.5 Additional Spectroscopic Observations

Every DR1 SN has been spectroscopically classified as a SN Ia directly by our team or through public reports. We aim to obtain at least one spectrum with our spectroscopic resources to ensure a consistent classification. Through a combination of our observations made with Kast double spectrograph (Miller & Stone 1994) on the Lick Observatory 3-m Shane telescope, the LRIS spectrograph (Oke et al. 1995) on the W. M. Keck Observatory 10-m telescope, the KOSMOS spectrograph (Martini et al. 2014) on the KPNO 4-m Mayall telescope, the Goodman spectrograph (Clemens et al. 2004) on the 4-m SOAR telescope, and the FLOYDS spectrograph (Sand et al. 2011) on the Faulkes 2-m telescopes, plus additional archival FLOYDS spectra and public classifications, we have obtained 436 spectra of 109 SNe Ia in DR1, corresponding to 98% of the sample. These data provide a confirmation of the SN type and phase of our first photometric observation, as well as spectral properties such as velocities and equivalent widths of spectral features. For 25 SNe Ia (21% of the sample), we possess $\geq$4 spectra; 12 SNe Ia have $\geq$10 spectra each.

Some host galaxies for SNe Ia in DR1 do not have cataloged redshifts. Our spectra often provide a precise redshift of the host galaxy, and when such data are absent, the SN spectrum itself provides a reasonable redshift (typical uncertainty of 0.005). We present new redshifts for 14 SN host galaxies in Table 3.2. Furthermore, we have obtained spectra of numerous host galaxies at the SN position after the SN has faded, providing additional environmental information that may reduce distance biases and uncertainties (Rigault et al. 2013, 2018; Jones et al. 2018c; Roman et al. 2018). All

spectroscopic data will be provided in a future work.

Table 3.2. Significant redshift differences

SN	Literature Redshift	New Redshift	$\lvert\Delta z\rvert$
2016eky	0.056	0.0513	0.0047
2016iyv	0.031	0.0303	0.0007
2017aac	0.03	0.0270	0.0030
2017euz	0.05	0.0502	0.0001
2017evc	0.049	0.0489	0.0001
2017hdv	0.0642	0.0564	0.0078
2017hmf	0.0619	0.0599	0.0020
2017hoo	0.0574	0.0623	0.0049
2017iln	0.078	0.0752	0.0028
2018bs	0.07	0.0670	0.0030
2019cpe	0.054	0.0489	0.0052
2019gbx	0.013	0.0131	0.0000
2019nhy	0.06	0.0550	0.0050
2019vnj	0.02	0.0247	0.0047

Note. — All of our measured redshifts have an uncertainty of ± 0.0001.

3.6 Survey Calibration

3.6.1 The Swope Natural System

All SSS *BVgri* photometry is presented in the Swope natural system. We note that this system was also used by CSP and discussed in a series of papers (Hamuy et al. 2006; Contreras et al. 2010; Stritzinger et al. 2011; Krisciunas et al. 2017; Phillips et al. 2019). The Swope natural system is presented in detail by Krisciunas et al. (2017), but here we offer a summary. The Swope natural system is defined on the AB system (Oke & Gunn 1983) such that

$$m_{\rm AB} = -2.5 \log f_\nu - 48.60, \tag{3.1}$$

where f_ν is in ergs^{-1} cm^{-2} Hz^{-1}.

Normally any photometric system can be transformed into a standard system by deriving color terms using stars observed by the two systems and determining corresponding transformations. However, SNe Ia have different spectral energy distributions from the stars used to determine the color transformation. For this reason, color terms cannot be used to reliably transform SN Ia magnitudes to a standard system. Instead, we present measurements in the Swope natural system and measure zero points by transforming the stellar magnitudes from the standard system, currently the PS1 system (Flewelling et al. 2020), to the Swope natural system.

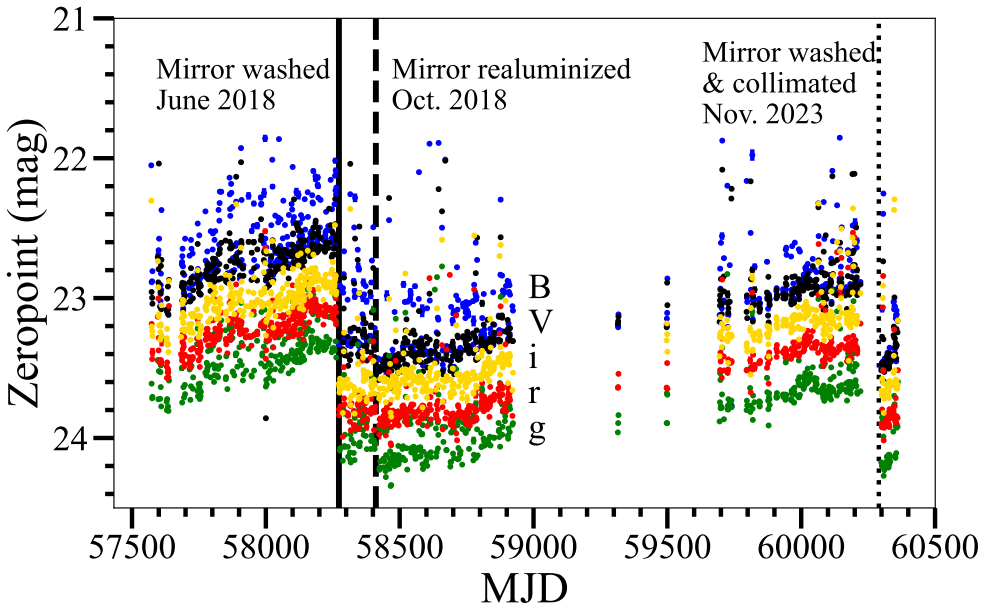

Figure 3.10 Nightly Swope zero points in *BVgri* bands. With time, the zeropoints slowly decrease. We mark the times when the primary mirror was washed and realuminized as solid and dashed lines, respectively. After each of these events, the zeropoint increases dramatically. Note that the large gap corresponds to the period of COVID restrictions when SSS did not obtain data.

3.6.2 Observations of Standard Stars

Standard stars were observed exclusively on photometric nights. In total, we observed 113 photometric nights. The majority of standard stars observed were CALSPEC stars[10], a group of bright stars with HST observations. Each star possesses STIS and NICMOS observations, from which calibrated composite spectra are produced.

Additionally, we have observed some other standard stars and fields, which will be used in future calibration analyses.

3.6.3 Supercal

The PS1 system has an excellent photometric calibration to the millimagnitude (mmag) level; Schlafly et al. (2012) used the 3π steradian sky coverage of PS1 to solve for its relative calibration with a precision of 5 mmag via the Ubercal method (Padmanabhan et al. 2008), and its absolute calibration was performed by Scolnic et al. (2015), who compared standard stars across multiple photometric systems (the "Supercal" method). PS1 has already observed thousands of SNe at low and high redshift (Jones et al. 2018a, 2021; Aleo et al. 2023). Here, we use the Supercal method to tie the Swope system to a single, homogeneous PS1 catalog . This PS1 catalog covers 3π of the sky, with a relative calibration of $\sim$ 5 mmag (Schlafly et al. 2012), and a depth of $\sim$ 22 mag (Scolnic et al. 2015).

The Supercal method compares observations of secondary stars in the Swope natural system to those in the PS1 system, determining the offsets between both sys-

[10] http://www.stsci.edu/hst/instrumentation/reference-data-for-calibration-and-tools/astronomical-catalogs/calspec

tems. This method uses many stars in the Swope system and the PS1 catalog, as it provides much better statistics than traditional calibration methods. These observed differences are compared to the differences in synthetic photometry from the HST CALSPEC standards stars. The final offsets between systems come from the difference between the observed and synthetic photometry fits at a reference color. We use the `PySynphot` (STScI Development Team 2013)[11] package to perform the synthetic photometry. The steps of Supercal are described in full in Scolnic et al. (2015) but are briefly summarized here:

1. Match astrometric positions of stars observed by Swope and PS1 to < 2 arcseconds, removing stars with companions of $m < 22$ within 15 arcseconds.

2. Subtract the observed magnitudes in a Swope filter to the closest PS1 filter, and compare to colors in the PS1 catalog ($g-r$ or $r-i$). Include the global offset (the zero point) of Swope magnitudes from each individual image as free parameters.

3. Choose a color range over which a linear relation as a function of PS1 color is valid, and select CALSPEC stars with colors in that range for comparison.

4. Determine the synthetic photometry of the CALSPEC standards in the desired Swope and PS1 filters, subtract the PS1 synthetic magnitude from the Swope magnitude, and find the PS1 synthetic color as in step 2.

5. Choose only PS1 and Swope stars with uncertainties < 0.02 mag to reduce the Malmquist bias and conservatively remove PS1 stars brighter than 16 mag in any of gri to eliminate any possible effects of nonlinearity in the PS1 detector.

[11] https://pysynphot.readthedocs.io/en/latest/index.html

Table 3.3. Supercal Transformation Parameters

Filt.$_{PS1}$	Filt.$_{Sw}$	Slope$_{\rm Obs}$	PS1 trans.	PS1 color cut
$g_{\rm PS1}$	$B_{\rm Sw}$	0.530	$g_{\rm PS1} - r_{\rm PS1}$	[0.25,0.85]
$g_{\rm PS1}$	$V_{\rm Sw}$	-0.384	$g_{\rm PS1} - r_{\rm PS1}$	[0.3,1.4]
$g_{\rm PS1}$	$g_{\rm Sw}$	0.076	$g_{\rm PS1} - r_{\rm PS1}$	[0.2,1.3]
$r_{\rm PS1}$	$r_{\rm Sw}$	-0.008	$g_{\rm PS1} - r_{\rm PS1}$	[0.2,1.3]
$i_{\rm PS1}$	$i_{\rm Sw}$	-0.070	$r_{\rm PS1} - i_{\rm PS1}$	[0.1,1.5]

6. Correct for the Milky Way reddening using Schlafly et al. (2012).

7. Perform the fits to the observed and synthetic data, propagating the errors and performing an iterative 3σ clipping.

We additionally apply the cuts used by Scolnic et al. (2015) on the HST CALSPEC standards, namely only solar analog stars (ensuring many stars are available to use for this calibration) and standards recently calibrated with WFC3.

We find that for 4 CALSPEC standard stars, the offset between Swope natural system magnitudes and synthetic magnitudes are 0.199, 0.001, 0.040, -0.000, and -0.004 for $BVgri$, respectively.

The typical uncertainties for bright stars in SN fields are 0.027, 0.018, 0.019, 0.019, 0.018 for $BVgri$, respectively. We also add a 1% error floor in quadrature to ensure the typical χ^2/dof is close to 1 when calculating mean magnitudes of stars.

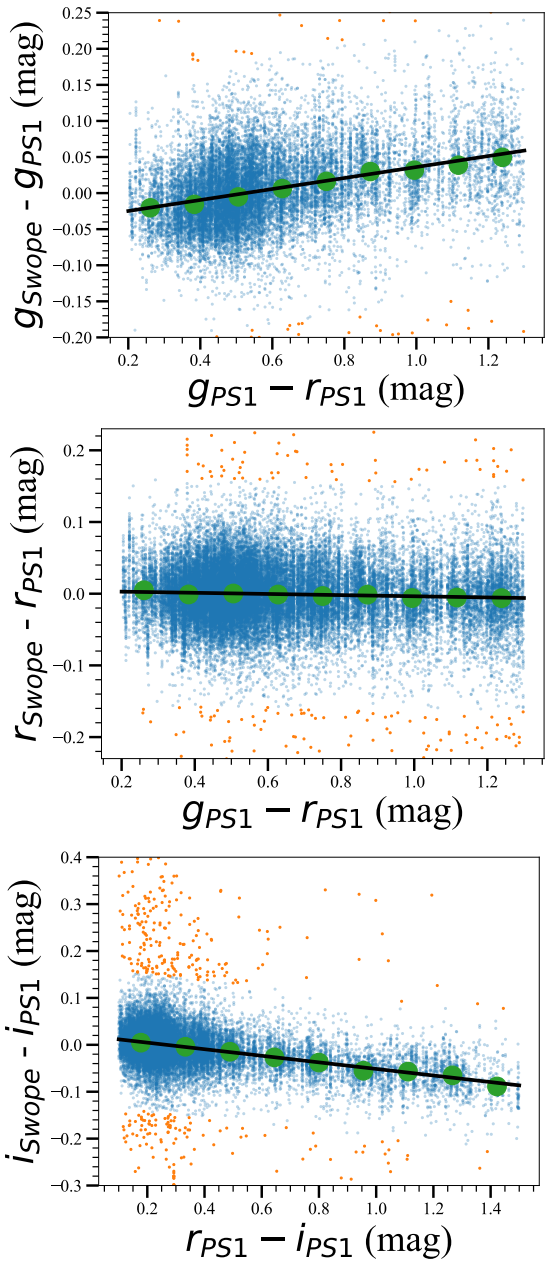

Figure 3.11 Difference between Swope and PS1 observations for stars observed in photometric conditions as a function of their PS1 color. The black line represents the best fit (best-fit parameters are listed in Table 3.3). The orange circles correspond to the clipped data from the best fit, and the green circles correspond to the median bins. Using the process outlined by Scolnic et al. (2015), these data can place Swope observations on the PS1 system.

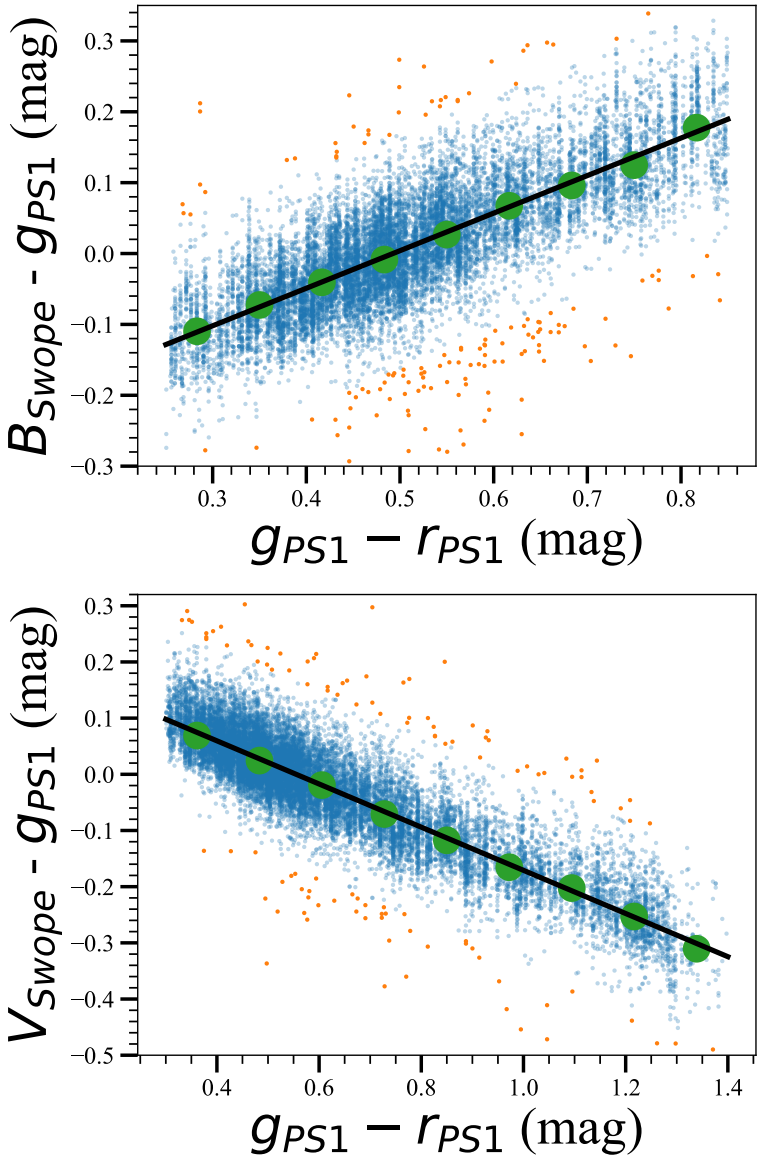

Figure 3.12 Same as Figure 3.11, for BV bands.

3.7 Light Curves and Sample Characteristics

After data reduction (Section 3.4) and calibration (Section 3.6), the SN photometry is finalized. We present example light curves in Figure 3.13, and also display all light curves in Figure 3.14 to show the temporal density and magnitude range of

observations for all of DR1.

A redshift is necessary to analyze a SN light curve, and we use host-galaxy redshifts when available. We use cataloged redshifts, retreived from the NASA/IPAC Extragalactic Database (NED) when possible, supplementing with our host-galaxy redshift measurements when necessary. If no host-galaxy redshift is available for this work, we use the redshift from the SN and will update with the host-galaxy redshift and new light-curve-fit parameters in future work (see Section 3.5).

3.7.1 Light-curve Fitting

We use the `SALT3` model (Kenworthy et al. 2021a), the standard distance-fitting method for SN Ia cosmology, implemented in `SNANA`[12] (Kessler et al. 2009), a SN light-curve analysis package, to fit all light curves and measure distances. The `SALT3` SED model is parameterized by an amplitude x_0 (or m_B, proportional to the log of x_0), x_1, which corresponds to a light-curve shape, and a phase-independent "color law," with the direction and amount of modification parameterized by c. The fitting process shifts the model in time and flux to match the data, and in doing so, determines the time of maximum brightness, t_0, and the peak brightness in the B band, m_B.

We measure distances using a Tripp (1998) relation,

$$\mu_B = m_B - M_B + \alpha x_1 - \beta c, \tag{3.2}$$

where M_B is the B-band absolute magnitude for a reference SN Ia ($x_1 = 0$ and $c = 0$, which by definition corresponds to the mean of the `SALT3` training sample), μ_B is the

[12] https://github.com/RickKessler/SNANA

distance modulus, and α and β are nuisance parameters adjusted to minimize Hubble residuals for a given sample.

We present light-curve parameters for SSS DR1 in Table 3.7.4.

3.7.2 Defining the Cosmology Sample

All SNe Ia included in this sample are selected for observation according to the criteria presented in section 2.3.4. We apply additional quality criteria to the SNe and their light curves to include them in our cosmology sample. These criteria are similar to the ones used by Foley et al. (2018) and are listed below:

1. A spectroscopically "normal" SN Ia (i.e., not similar to SNe Iax (Li et al. 2003; Foley et al. 2013; Jha 2017), SN 1991bg (Filippenko et al. 1992a; Leibundgut et al. 1993), SN 2000cx (Li et al. 2001), and SN 2006gz (Howell et al. 2006; Hicken et al. 2007; Yamanaka et al. 2009; Silverman et al. 2011; Taubenberger et al. 2011; Scalzo et al. 2012)).

2. Milky Way reddening of $E(B-V)_{\rm MW} < 0.2$ mag.

3. A total of at least 15 light-curve points in the different $BVgri$ Swope bands.

4. First observation has a phase of at least seven days before maximum light.

5. An uncertainty on x_1 of <1.

6. An uncertainty of the time of maximum brightness of $< +1$ days.

7. $-0.3 < c < 0.3$.

8. $-3.0 < x_1 < 3.0$.

9. Chauvenet's criterion (Chauvenet 1863), a statistical method used exclude outliers far from a normal distribution, applied to the pulls rather than to the residuals, which would bias against SNe at low redshift due to their larger peculiar-velocity scatter.

These additional criteria are selected to remove objects that may be poorly fit by SALT3, and SNe Ia that do not follow the Phillips relation (1), unreliable light-curve fits (2-6), and for them to be within the bounds of the SALT3 model (7-8), and removes systematic outliers outside a normal distribution (9).

Of the 111 light curves presented in this paper, 76 pass the above criteria and therefore are expected to produce accurate distances. Of the 35 objects removed, 17 were observed at the beginning of the survey, when we selected SNe Ia already followed by the Foundation Supernova Survey (Foley et al. 2018), and therefore do not have complete light curves. We present a summary of the SNe failing each criterion individually and cumulatively as well as the SNe remaining in the sample after each criterion in Table 4.2.

3.7.3 Comparison to Foundation Supernova Survey

A basic test of the SSS photometry is to compare to other observations. In Section 3.6, we discuss photometry of the same stars observed by both the Swope and Pan-STARRS1 telescopes. While this comparison is informative and allows for an analysis of a large number of measurements, it does not directly address SN photometry itself.

However, as part of the Foundation Supernova Survey (Foley et al. 2018), Pan-

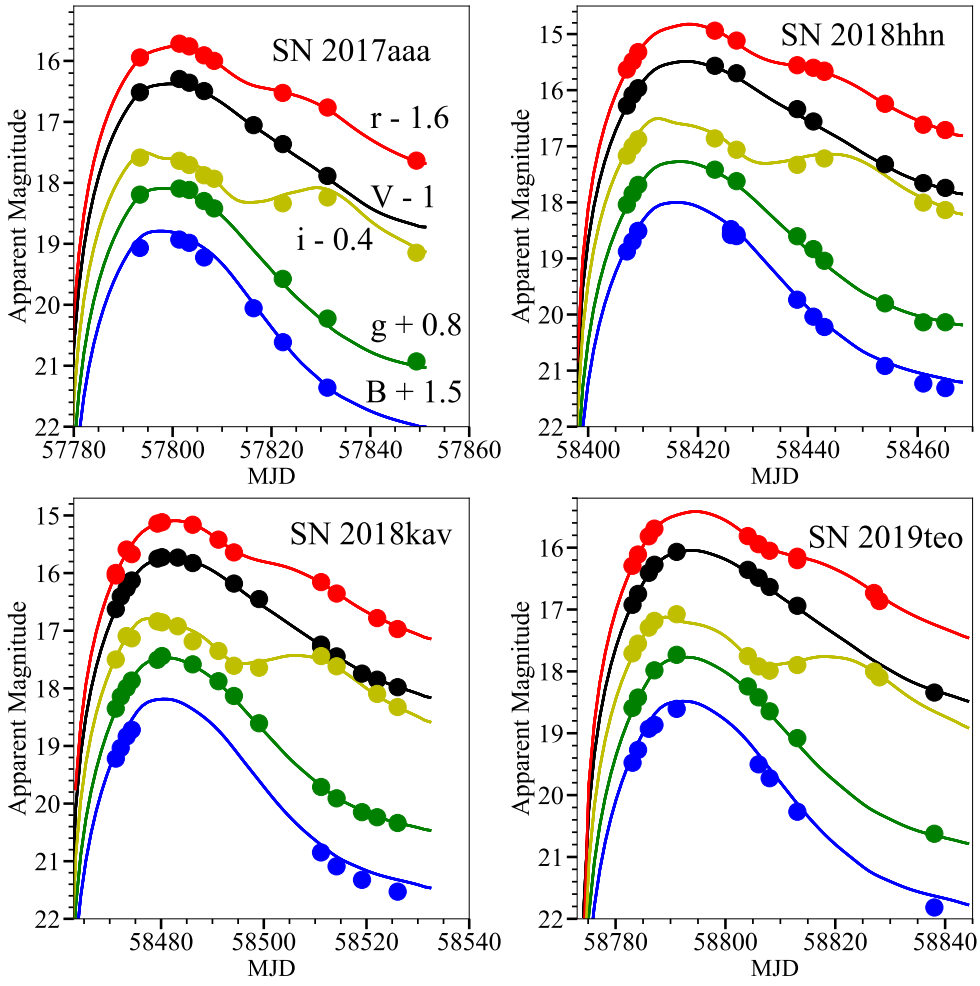

Figure 3.13 Swope *BVgri* light curves for a representative sample of SNe Ia in this data release. Magnitudes are offset for clarity purposes in all four panels.

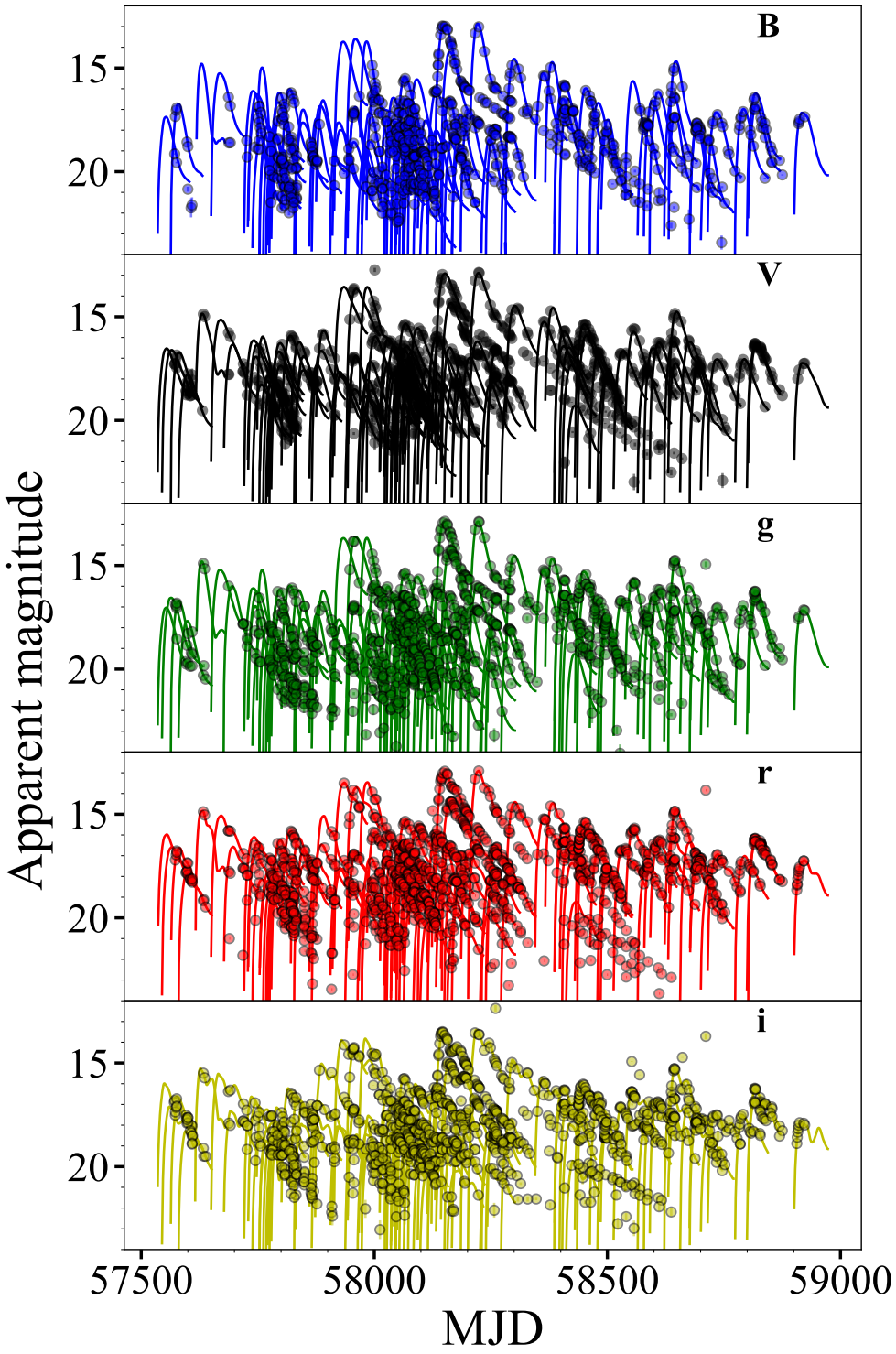

Figure 3.14 Complete light curves with SALT3 fits for SSS DR1 in all five *BVgri* bands presented in this work.

STARRS1 observed hundreds of SNe Ia, and its first data release, covering 225 SNe Ia observed over 2015–2017, had several SNe Ia in common with SSS DR1. The final samples of both surveys will have ∼100 overlapping SNe Ia, to directly compare SN photometry in addition to stellar photometry.

Here, we present an initial comparison of photometry and light-curve parameters for the overlapping 13 objects between the Foundation Supernova Survey DR1 and SSS DR1. We note that most of these objects were observed during the first year of SSS, including several that had peaked before SSS began its survey. Nevertheless, this limited sample provides an opportunity that few previous surveys have had – to directly compare SN photometry.

Figure 3.15 presents the combination of Foundation Supernova Survey and SSS light curves for a single SN Ia. We also present the best-fitting SALT3 model for the Foundation data in the Swope bands. For each overlapping SN, we are able to both measure the residual between the SSS photometry and the Foundation-fit SALT3 model, as well as the residuals between SSS and Foundation photometry when observations on the two systems were taken within 0.7 days of each other. We find that the residuals with the SALT3 model have a weighted RMS (WRMS) of 0.045, 0.027, 0.033, 0.022, and 0.029 mag in $BVgri$, respectively. For the gri bands, we find that the weighted mean offset between Foundation and SSS photometry when observations on the two systems were taken within 0.7 days of each other is 0.028 ± 0.017, -0.032 ± 0.007, and -0.002 ± 0.011 mag, respectively, while the WRMS of the same residuals is 0.064, 0.030, and 0.039 mag, respectively.

Fitting the SSS light curves with SALT3, we are able to measure independent

Table 3.4. Cosmology sample cuts

Criterion	No. SNe NP	Cum. SNe NP	SNe Rem.
Initial Sample	···	···	111
Not similar to Iax/ 91bg/06gz	2	2	109
$E(B-V)_{\rm MW} < 0.2$ mag	0	2	109
Suffic. LC coverage (> 15 data points)	1	3	108
$t_{\rm first} < 7$ day	22	22	89
$\sigma(x_1) < 1$	3	23	87
$\sigma(t_{\rm peak}) < 1$ day	8	23	87
$-0.3 < c < 0.3$	6	26	84
$-3.0 < x_1 < 3.0$	3	27	83
Chauvenet	7	34	76

light-curve parameters and distances that can be directly compared to the values derived from Foundation Supernova Survey data (Figure 3.16). For the SNe that pass all of the criteria for being included in the cosmological sample, we find a WRMS of 0.304, 0.049, and 0.049 mag for x_1, c, and distance modulus, respectively.

3.7.4 Hubble Diagram

In Figure 3.21, we present a Hubble diagram for SSS DR1 SNe Ia that fulfill all of the criteria outlined in Section 3.7.2 for inclusion in a cosmological analysis. In this work, we have not performed several steps necessary to derive cosmological parameters such as determining any bias correction, and thus this Hubble diagram is more illustrative of the quality of data and distribution of SNe Ia in redshift. Because of its illustrative nature, we also removed any SN with $\sigma_\mu > 0.3$ mag.

Additional examination of the SNe and light curves may further improve distance measurements or exclude non-standard SNe. In particular, external data that

could constrain the time of maximum independently from Swope data will likely improve the distance measurements and uncertainties for a subset of the sample. Furthermore, spectral data may result in the reclassification of some SNe, potentially removing some outliers that are peculiar.

With all of the above caveats, we measure a weighted RMS of 0.122 mag. Accounting for an uncertainty for peculiar velocity of 250 km/s, we measure an intrinsic scatter of 0.110 mag. This is comparable to the Pantheon+ value, (Brout et al. 2022a), lower than the original Pantheon value (Scolnic et al. 2018), and comparable to the Foundation (Foley et al. 2018) values. We aim to decrease our intrinsic scatter measurement with additional examination as mentioned above, and at least double our SN sample in future work.

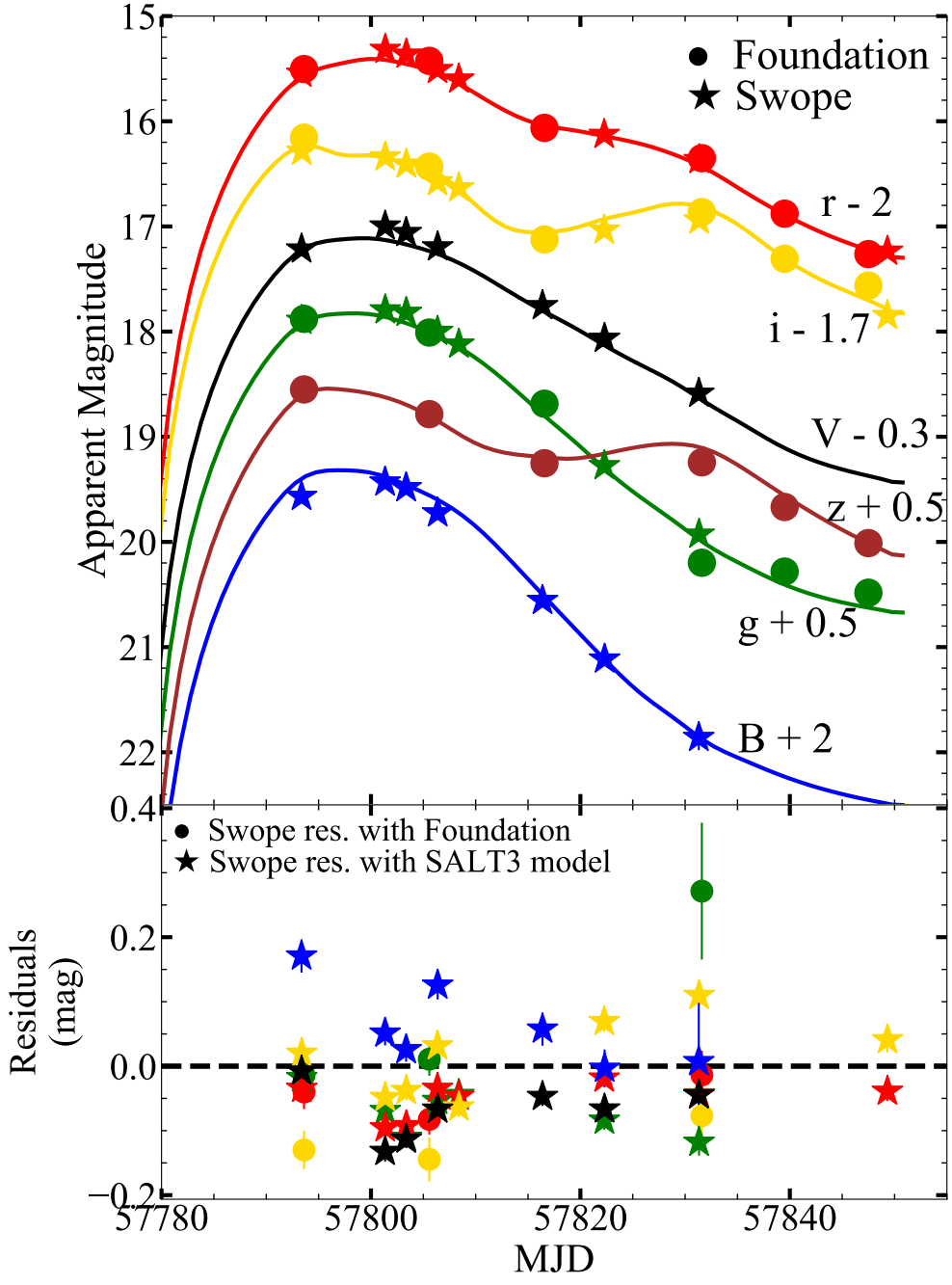

Figure 3.15 *Top panel*: *BVgri* light curves of SN 2017aaa as observed by Pan-STARRS1 and presented by the Foundation Supernova Survey (circles) and presented in this work and observed by Swope (stars). Each band is labeled and an offset is applied to each band, marked on the plot, for clarity. Solid lines represent the SALT3 models using the best-fitting x_1 and c parameters from only the Foundation data, but in the Swope bands. *Bottom panel*: Residuals of the SSS photometry relative to Foundation photometry (circles) and the SALT3 model with the Foundation best-fitting parameters (stars). We only compare the two data sets on epochs where the data are obtained within one day, resulting in three epochs.

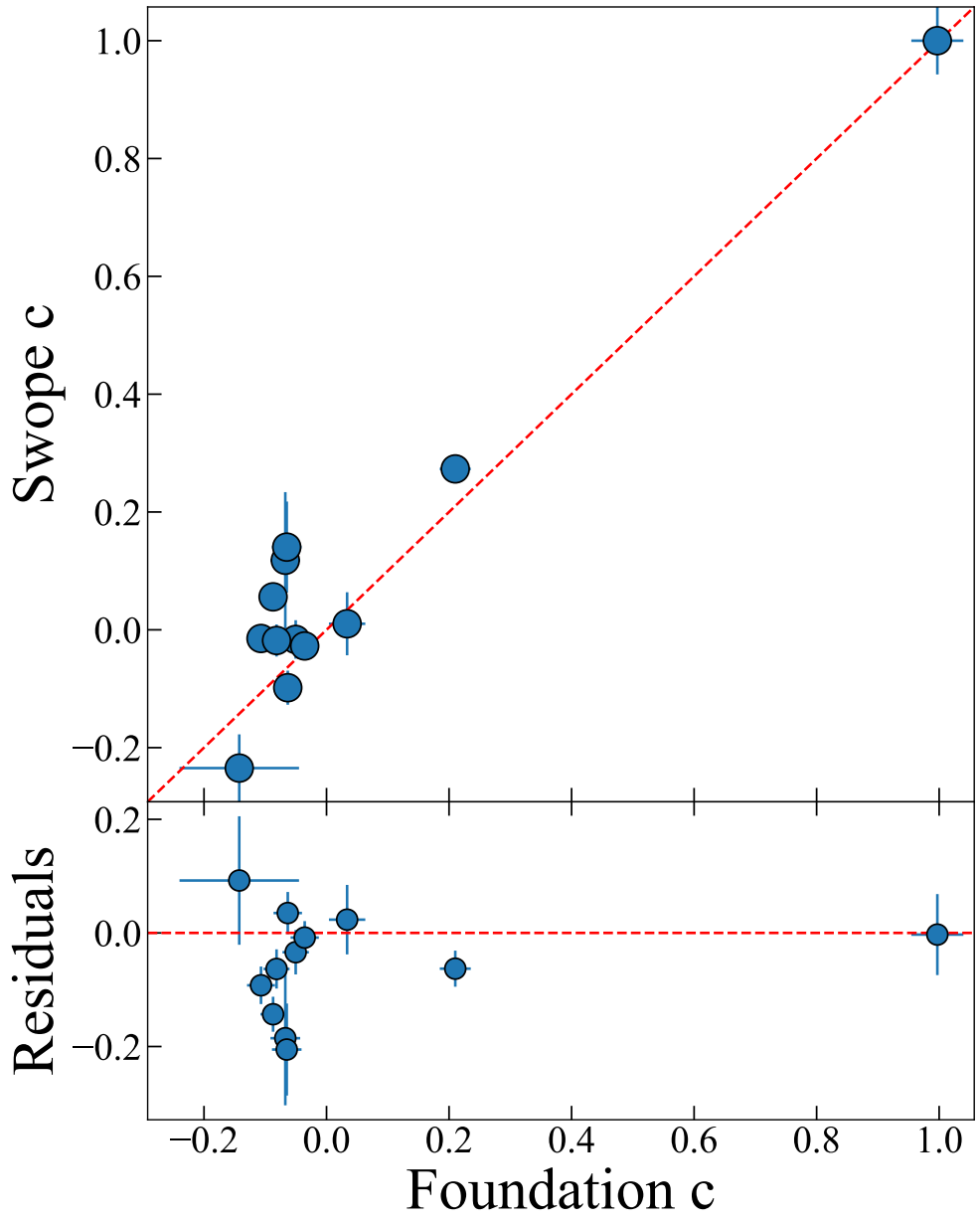

Figure 3.16 Comparison between SSS DR1 and Foundation DR1 of light curve parameter c for 12 overlapping SN Ia. We removed SNe with errors > 0.5 for clarity purposes (SN 2017nk, which has a poor SSS DR1 light curve, and is excluded from our cosmological sample according to the criteria listed in Section 3.7.2).

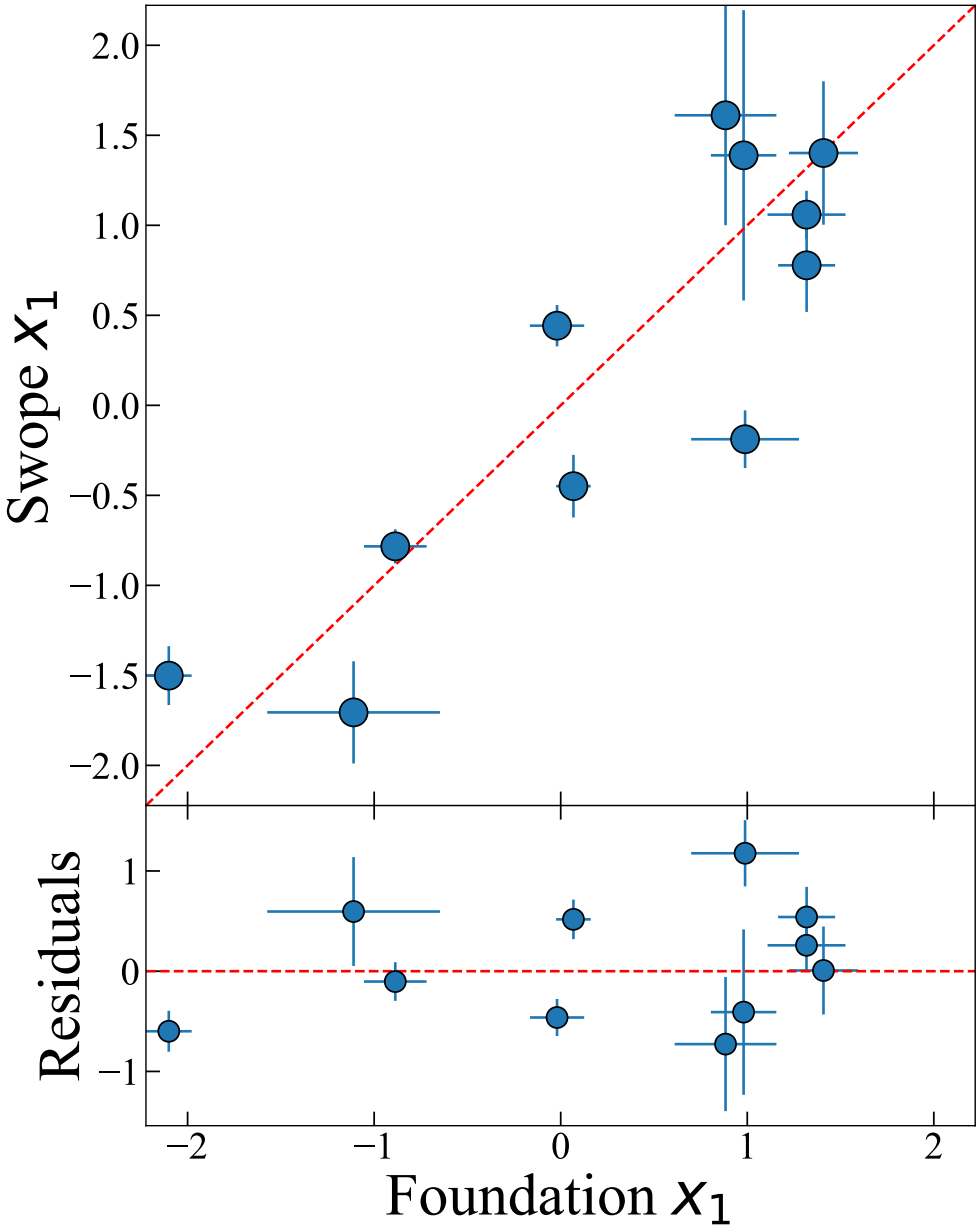

Figure 3.17 Comparison between SSS DR1 and Foundation DR1 of light-curve parameter x_1 for 11 overlapping SN Ia. Similarly to Figure 3.16, we remove outliers for clarity purposes (SN 2016fff and SN 2017nk, which are excluded from our cosmological sample).

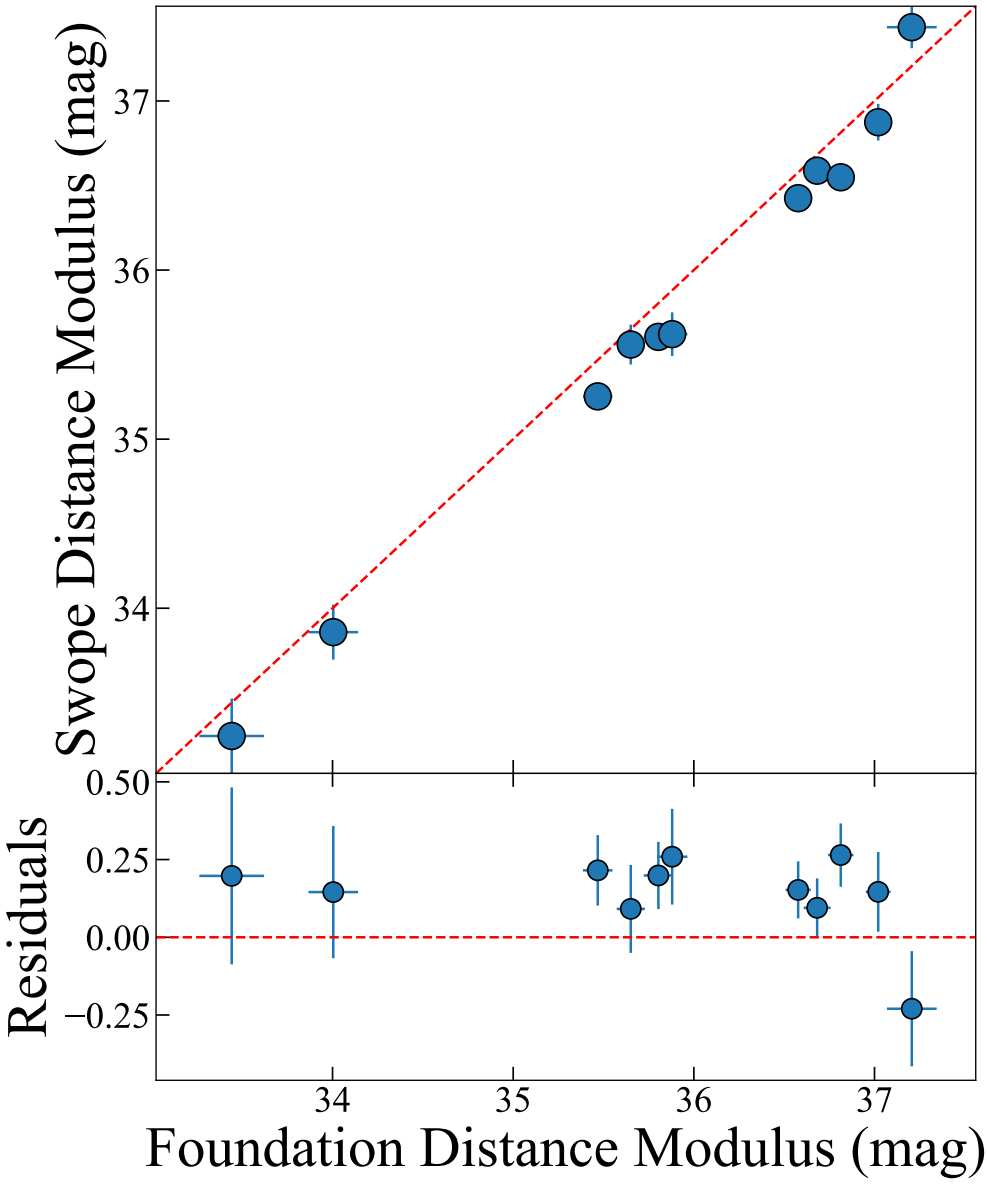

Figure 3.18 Comparison between SSS DR1 and Foundation DR1 of light-curve parameter μ, the distance modulus, for 12 overlapping SN Ia. Similarly to Figure 3.16, we remove SN 2017nk.

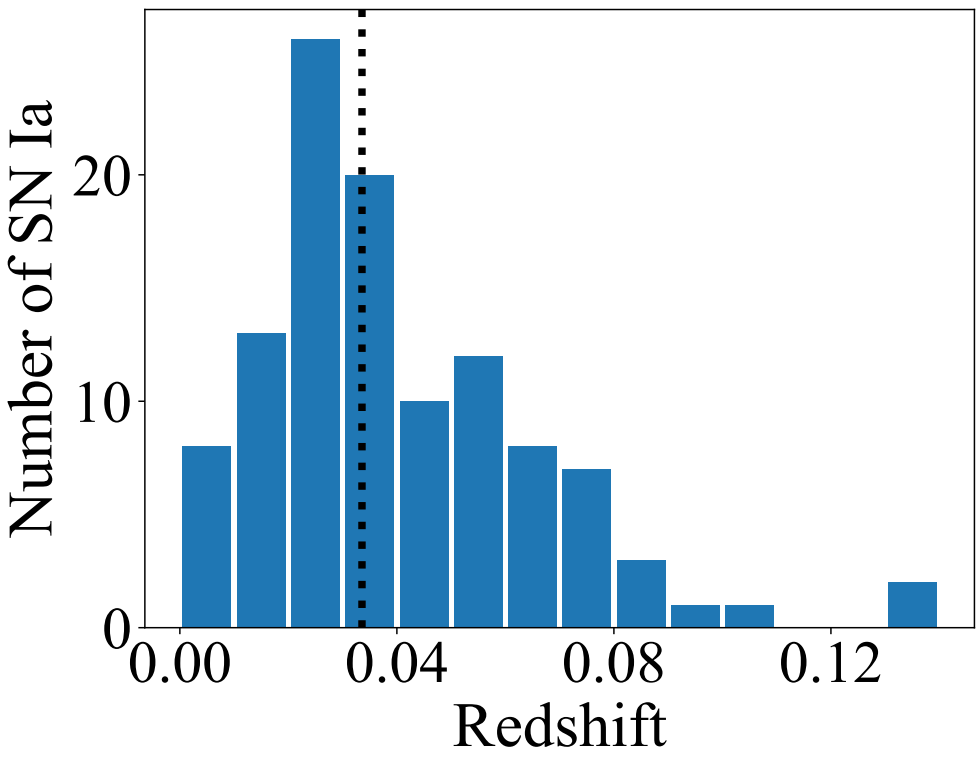

Figure 3.19 Redshift distribution for the complete SSS DR1 sample. The median redshift, 0.034, is marked with a dashed line.

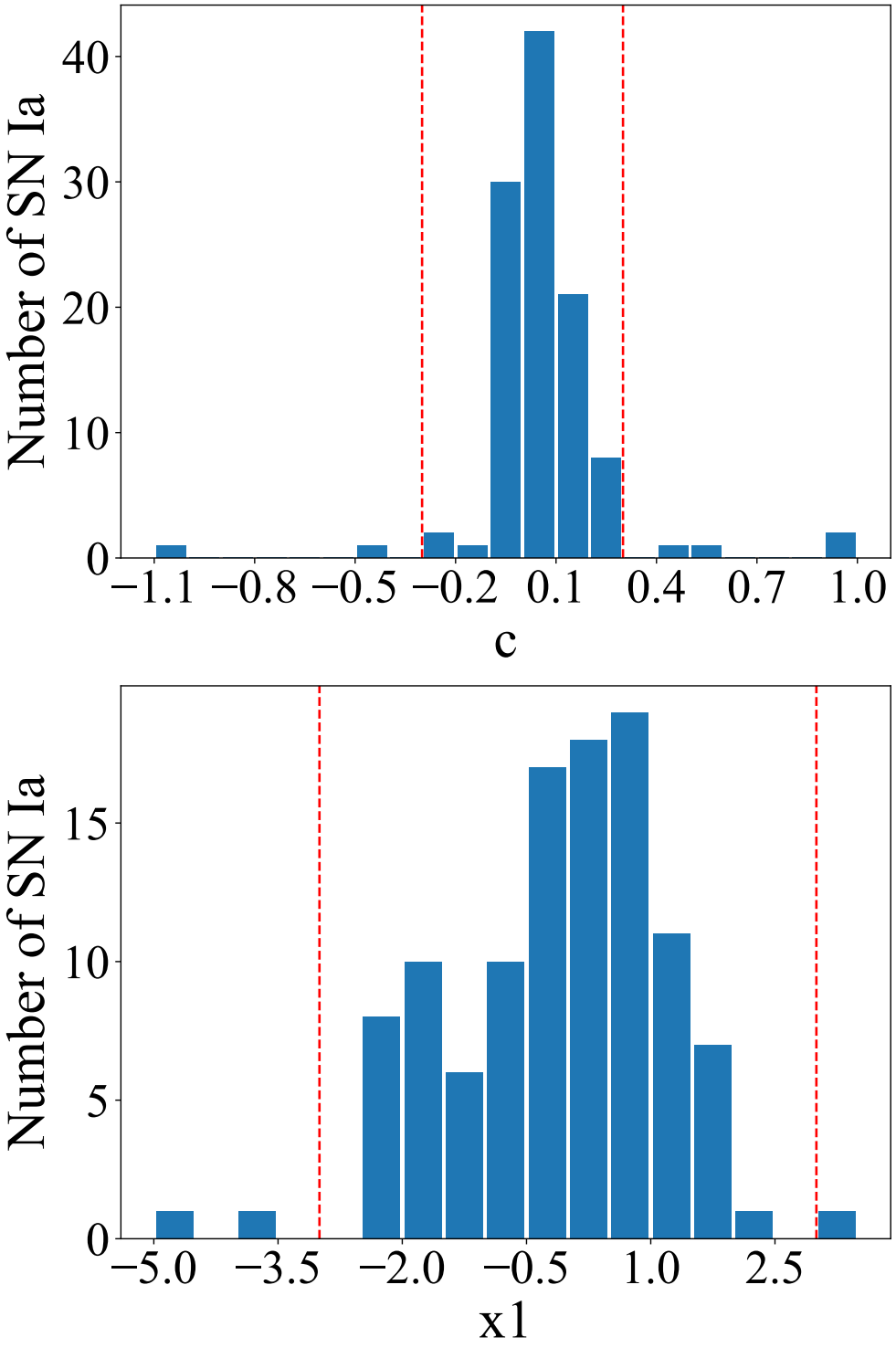

Figure 3.20 Distributions of c (top panel) and x_1 (bottom panel) for the SSS. Vertical dashed lines correspond to the sample cuts necessary to be included in the cosmology sample.

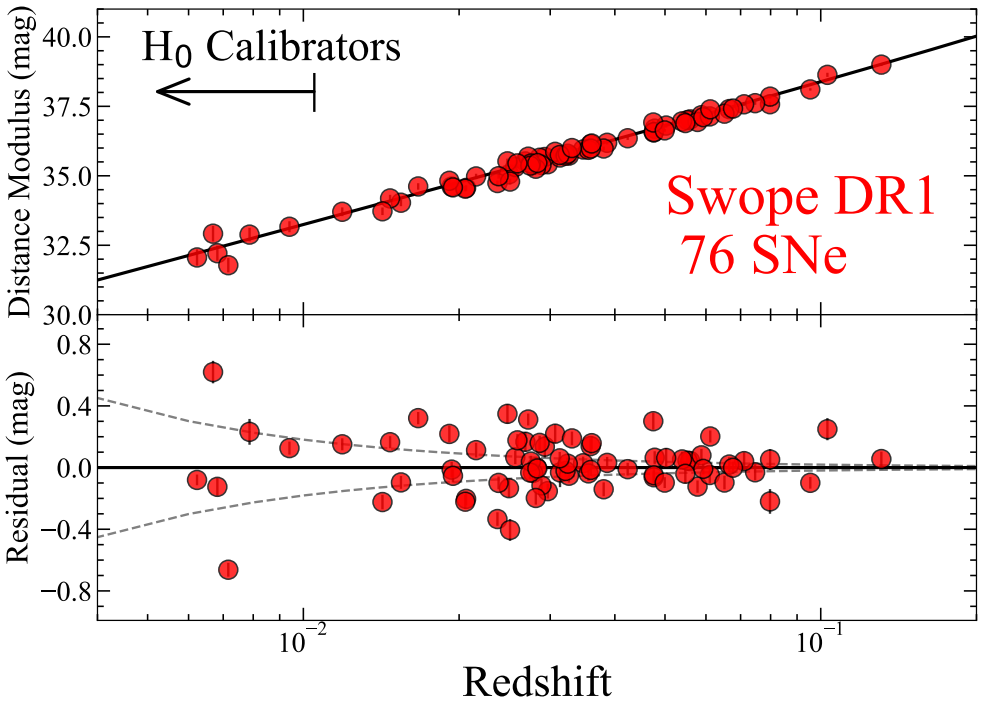

Figure 3.21 Hubble diagram for the SSS DR1 sample and residuals to a fiducial ΛCDM model (lower panel). Error bars do not include uncertainties related to peculiar velocities (represented by the dotted curves in the lower panel), intrinsic scatter, and redshift uncertainties.

Table 3.5. SSS DR1 light-curve parameters.

SN	$z_{\rm helio}$	$z_{\rm CMB}$	Peak MJD	x_1	c	m_B (mag)
2016cvn	0.01369 (0.00012)	0.01481 (0.00012)	57553.42 (0.72)	−0.45 (0.17)	1.000 (0.057)	17.08 (0.03)
2016cxb	0.02954 (0.00009)	0.02847 (0.00009)	57564.66 (0.76)	0.78 (0.26)	−0.018 (0.027)	16.09 (0.08)
2016cyt	0.03074 (0.00009)	0.02968 (0.00009)	57580.55 (0.12)	−1.50 (0.16)	0.056 (0.023)	16.29 (0.05)
2016eky	0.05127 (0.00003)	0.05004 (0.00003)	57599.12 (1.02)	−0.19 (0.16)	−0.098 (0.029)	17.23 (0.09)
2016fff	0.01144 (0.00001)	0.01041 (0.00001)	57629.77 (0.93)	−3.88 (1.97)	0.010 (0.053)	14.55 (0.06)
2016gsn	0.01505 (0.00004)	0.01391 (0.00004)	57670.01 (0.13)	1.39 (0.81)	0.118 (0.116)	14.66 (0.18)
2016ije	0.04000 (0.01000)	0.03907 (0.01000)	57695.73 (0.14)	−0.50 (0.33)	−0.445 (0.040)	15.62 (0.09)
2016ivt	0.02707 (0.00001)	0.02826 (0.00001)	57741.02 (0.10)	0.66 (0.24)	0.062 (0.026)	15.87 (0.04)
2016ixb	0.02834 (0.00011)	0.02824 (0.00011)	57744.71 (0.29)	−1.77 (0.11)	0.142 (0.028)	16.63 (0.05)
2016iyv	0.03030 (0.00010)	0.03134 (0.00010)	57749.64 (0.54)	1.40 (0.40)	−0.014 (0.033)	15.95 (0.06)
2016jbs	0.05484 (0.00015)	0.05594 (0.00015)	57757.61 (0.27)	−0.14 (0.20)	0.158 (0.024)	18.05 (0.04)
2017aaa	0.04681 (0.00001)	0.04776 (0.00001)	57799.05 (0.15)	1.06 (0.13)	−0.027 (0.018)	16.99 (0.03)
2017aac	0.02696 (0.00001)	0.02780 (0.00001)	57797.16 (0.20)	−0.45 (0.09)	0.003 (0.018)	15.96 (0.02)
2017adj	0.03165 (0.00010)	0.03261 (0.00010)	57794.92 (0.52)	0.44 (0.11)	−0.015 (0.024)	16.13 (0.07)
2017cal	0.02069 (0.00012)	0.02063 (0.00012)	57819.01 (0.29)	−0.64 (0.10)	0.169 (0.019)	15.68 (0.04)
2017cfc	0.02403 (0.00016)	0.02497 (0.00016)	57837.98 (0.13)	−1.10 (0.12)	0.064 (0.026)	15.90 (0.04)
2017cne	0.03377 (0.00001)	0.03439 (0.00001)	57847.71 (0.96)	−1.55 (0.32)	0.190 (0.017)	16.69 (0.05)
2017cpu	0.05440 (0.00001)	0.05525 (0.00001)	57848.61 (0.11)	1.61 (0.61)	0.140 (0.077)	17.39 (0.11)
2017djl	0.04453 (0.00027)	0.04564 (0.00027)	57877.04 (1.33)	−1.96 (1.20)	0.191 (0.080)	17.06 (0.27)
2017drh	0.00555 (0.00000)	0.00543 (0.00000)	57890.22 (0.10)	−1.93 (0.12)	1.000 (0.014)	16.04 (0.04)
2017dys	0.02926 (0.00015)	0.02823 (0.00015)	57885.80 (0.47)	0.60 (0.13)	0.288 (0.024)	16.55 (0.04)
2017erp	0.00617 (0.00000)	0.00682 (0.00000)	57934.07 (0.63)	0.78 (0.20)	0.183 (0.034)	13.20 (0.08)
2017euz	0.05016 (0.00010)	0.04954 (0.00010)	57924.88 (2.04)	0.37 (0.46)	−0.021 (0.072)	17.10 (0.15)
2017evc	0.04887 (0.00010)	0.04796 (0.00010)	57930.14 (1.96)	2.25 (0.85)	0.259 (0.191)	17.65 (0.31)
2017fgc	0.00774 (0.00013)	0.00669 (0.00013)	57960.74 (0.12)	1.06 (0.18)	0.011 (0.026)	13.33 (0.04)
2017fms	0.03036 (0.00006)	0.02929 (0.00006)	57959.79 (0.13)	−1.43 (0.57)	0.043 (0.028)	16.50 (0.05)
2017fmz	0.02803 (0.00015)	0.02686 (0.00015)	57958.88 (0.34)	−2.13 (0.48)	0.028 (0.030)	16.38 (0.07)
2017fnz	0.08100 (0.00500)	0.07979 (0.00500)	57958.00 (0.85)	1.01 (0.36)	0.052 (0.028)	18.12 (0.05)
2017fzw	0.00537 (0.00006)	0.00576 (0.00006)	57983.77 (0.52)	−2.38 (0.17)	0.220 (0.056)	13.41 (0.10)
2017gdg	0.08880 (0.00030)	0.08775 (0.00030)	57983.57 (0.93)	0.10 (0.23)	−0.017 (0.030)	18.60 (0.07)
2017gfa	0.07760 (0.00030)	0.07657 (0.00030)	57985.71 (0.07)	−0.06 (0.14)	0.037 (0.024)	17.85 (0.03)
2017gfl	0.08080 (0.00030)	0.07983 (0.00030)	57992.86 (0.60)	0.87 (0.31)	0.022 (0.023)	18.32 (0.03)
2017gjd	0.02002 (0.00015)	0.01935 (0.00015)	58001.48 (0.10)	−0.85 (0.11)	0.076 (0.024)	15.46 (0.06)
2017glb	0.03709 (0.00015)	0.03703 (0.00015)	57991.07 (0.47)	−0.75 (0.12)	0.039 (0.024)	16.78 (0.05)
2017gvp	0.02278 (0.00002)	0.02157 (0.00002)	58029.57 (0.13)	−0.70 (0.09)	0.066 (0.020)	15.78 (0.03)
2017gwy	0.02983 (0.00002)	0.02862 (0.00002)	58027.48 (0.18)	−2.40 (0.14)	0.191 (0.021)	17.06 (0.05)
2017hdv	0.05644 (0.00010)	0.05527 (0.00010)	58047.08 (0.13)	0.95 (0.12)	−0.008 (0.019)	17.37 (0.03)
2017hfv	0.02820 (0.00010)	0.02886 (0.00010)	58041.73 (0.41)	0.22 (0.10)	0.084 (0.018)	16.14 (0.04)
2017hhi	0.05370 (0.01000)	0.05269 (0.01000)	58039.81 (0.48)	−0.68 (0.17)	−0.159 (0.023)	17.33 (0.04)
2017hmf	0.05995 (0.00001)	0.05880 (0.00001)	58055.00 (0.13)	0.35 (0.15)	0.048 (0.020)	17.79 (0.05)
2017hoo	0.06228 (0.00001)	0.06182 (0.00001)	58055.07 (0.19)	0.08 (0.11)	−0.002 (0.021)	17.97 (0.03)
2017hou	0.01691 (0.00001)	0.01657 (0.00001)	58035.96 (0.06)	−1.20 (0.26)	−0.082 (0.049)	15.55 (0.11)
2017hpa	0.01563 (0.00000)	0.01544 (0.00000)	58066.27 (0.06)	0.29 (0.06)	0.049 (0.029)	14.66 (0.10)
2017hpj	0.03703 (0.00012)	0.03592 (0.00012)	58062.16 (0.13)	1.28 (0.12)	−0.097 (0.021)	16.18 (0.03)
2017hqc	0.03988 (0.00027)	0.03865 (0.00027)	58064.34 (0.07)	0.41 (0.07)	−0.010 (0.019)	16.62 (0.05)
2017htb	0.02685 (0.00002)	0.02568 (0.00002)	58068.84 (0.14)	1.06 (0.23)	0.159 (0.018)	16.19 (0.03)
2017hxc	0.05895 (0.00015)	0.05779 (0.00015)	58065.54 (0.34)	0.33 (0.15)	−0.002 (0.018)	17.40 (0.04)
2017hxo	0.06171 (0.00001)	0.06104 (0.00001)	58073.67 (0.20)	0.97 (0.15)	0.029 (0.031)	17.62 (0.08)
2017hyx	0.03815 (0.00015)	0.03806 (0.00015)	58076.24 (0.19)	−1.77 (0.11)	0.110 (0.020)	17.06 (0.04)
2017ilf	0.02970 (0.00004)	0.03067 (0.00004)	58080.28 (0.02)	−0.36 (0.22)	−0.060 (0.043)	16.23 (0.07)
2017iln	0.07519 (0.00010)	0.07468 (0.00010)	58083.91 (0.44)	1.51 (0.27)	0.039 (0.040)	18.06 (0.13)
2017isj	0.01935 (0.00001)	0.02056 (0.00001)	58092.14 (0.34)	0.16 (0.09)	0.050 (0.024)	15.18 (0.05)
2017iws	0.09455 (0.00003)	0.09546 (0.00003)	58104.25 (0.02)	0.73 (0.11)	0.044 (0.015)	18.66 (0.02)
2017iye	0.04639 (0.00015)	0.04756 (0.00015)	58111.23 (0.14)	−0.79 (0.09)	−0.004 (0.020)	17.16 (0.04)
2017jgi	0.13000 (0.01000)	0.13097 (0.01000)	58117.27 (0.49)	−0.55 (0.37)	0.014 (0.024)	19.62 (0.03)

Table 3.5 (cont'd)

SN	$z_{\rm helio}$	$z_{\rm CMB}$	Peak MJD	x_1	c	m_B (mag)
2017lb	0.05278 (0.00011)	0.05395 (0.00011)	57773.00 (0.59)	0.42 (0.23)	0.013 (0.023)	17.46 (0.05)
2017lc	0.06000 (0.01000)	0.06113 (0.01000)	57770.51 (0.95)	−1.71 (0.28)	−0.235 (0.057)	17.59 (0.10)
2017nk	0.03445 (0.00001)	0.03479 (0.00001)	57759.64 (2.79)	−4.64 (0.35)	−1.005 (0.651)	14.78 (0.37)
2017ux	0.07000 (0.01000)	0.07110 (0.01000)	57788.01 (0.43)	0.69 (0.20)	−0.025 (0.022)	17.92 (0.04)
2017yk	0.04644 (0.00015)	0.04758 (0.00015)	57789.45 (0.25)	−0.78 (0.09)	0.273 (0.019)	18.04 (0.03)
2017yn	0.07000 (0.01000)	0.07117 (0.01000)	57782.19 (1.54)	1.09 (0.56)	−0.053 (0.030)	17.69 (0.07)
2018aay	0.03090 (0.00021)	0.03212 (0.00021)	58185.97 (0.21)	−0.32 (0.11)	0.217 (0.017)	16.95 (0.03)
2018abz	0.05486 (0.00013)	0.05606 (0.00013)	58184.41 (0.16)	−0.73 (0.10)	0.128 (0.019)	18.40 (0.03)
2018ael	0.13800 (0.01000)	0.13906 (0.01000)	58177.73 (1.57)	1.83 (0.72)	−0.049 (0.074)	19.50 (0.17)
2018agk	0.02613 (0.00015)	0.02720 (0.00015)	58204.17 (0.08)	−0.14 (0.11)	0.186 (0.017)	16.80 (0.03)
2018aoz	0.00603 (0.00015)	0.00716 (0.00015)	58222.30 (0.10)	−1.36 (0.07)	−0.018 (0.021)	12.40 (0.05)
2018aqh	0.02373 (0.00003)	0.02480 (0.00003)	58220.29 (0.46)	0.22 (0.21)	−0.067 (0.022)	15.79 (0.03)
2018bfr	0.07175 (0.00015)	0.07297 (0.00015)	58248.78 (0.05)	−0.49 (0.14)	0.225 (0.018)	18.11 (0.03)
2018bfs	0.10200 (0.00500)	0.10301 (0.00500)	58246.76 (0.84)	0.66 (0.33)	0.156 (0.030)	19.55 (0.06)
2018bgz	0.03415 (0.00001)	0.03473 (0.00001)	58262.32 (0.11)	1.32 (0.12)	−0.007 (0.018)	16.27 (0.03)
2018bq	0.02558 (0.00015)	0.02681 (0.00015)	58134.00 (0.27)	1.32 (0.31)	0.290 (0.025)	15.90 (0.03)
2018bs	0.06703 (0.00010)	0.06656 (0.00010)	58134.26 (0.19)	0.29 (0.14)	−0.015 (0.020)	17.83 (0.02)
2018bsn	0.05862 (0.00001)	0.05928 (0.00001)	58259.88 (0.01)	1.55 (0.12)	0.069 (0.015)	17.64 (0.02)
2018cjy	0.06409 (0.00015)	0.06515 (0.00015)	58292.81 (0.39)	1.76 (0.21)	0.065 (0.020)	17.73 (0.05)
2018cqw	0.00977 (0.00018)	0.00940 (0.00018)	58300.60 (0.06)	−0.09 (0.11)	0.064 (0.027)	13.89 (0.08)
2018feb	0.01476 (0.00006)	0.01471 (0.00006)	58363.10 (0.11)	−0.24 (0.06)	0.051 (0.018)	14.89 (0.04)
2018ghb	0.00731 (0.00015)	0.00787 (0.00015)	58381.93 (0.24)	−2.11 (0.20)	0.121 (0.038)	14.04 (0.09)
2018gl	0.01803 (0.00013)	0.01915 (0.00013)	58138.68 (0.11)	−2.33 (0.17)	0.076 (0.024)	15.86 (0.04)
2018gv	0.00537 (0.00015)	0.00623 (0.00015)	58150.61 (0.05)	0.55 (0.06)	0.007 (0.016)	12.52 (0.04)
2018hfp	0.02909 (0.00015)	0.02814 (0.00015)	58405.66 (0.42)	0.33 (0.14)	0.113 (0.019)	16.08 (0.04)
2018hfr	0.02260 (0.00015)	0.02372 (0.00015)	58406.94 (0.35)	0.98 (0.15)	0.118 (0.016)	15.50 (0.02)
2018hhn	0.02876 (0.00052)	0.02753 (0.00052)	58417.01 (0.06)	0.39 (0.10)	0.065 (0.018)	16.10 (0.04)
2018how	0.05130 (0.00030)	0.05026 (0.00030)	58422.98 (0.71)	0.63 (0.23)	−0.078 (0.032)	17.00 (0.05)
2018hzx	0.04654 (0.00052)	0.04548 (0.00052)	58430.94 (3.74)	1.64 (1.40)	0.065 (0.147)	19.00 (0.31)
2018ilu	0.01790 (0.00030)	0.01667 (0.00030)	58450.32 (0.05)	0.73 (0.08)	−0.042 (0.020)	14.90 (0.04)
2018jeo	0.01843 (0.00015)	0.01946 (0.00015)	58454.60 (0.20)	0.28 (0.09)	0.022 (0.031)	15.13 (0.11)
2018kav	0.03250 (0.00500)	0.03244 (0.00500)	58481.35 (0.05)	−0.03 (0.06)	0.024 (0.017)	16.38 (0.03)
2018km	0.04800 (0.00500)	0.04746 (0.00500)	58150.58 (0.13)	−0.49 (0.16)	0.206 (0.024)	18.13 (0.04)
2018oh	0.01095 (0.00002)	0.01189 (0.00002)	58162.99 (0.07)	0.68 (0.05)	−0.066 (0.017)	13.92 (0.03)
2018ph	0.03040 (0.00022)	0.03125 (0.00022)	58160.88 (0.25)	−1.95 (0.09)	0.047 (0.018)	16.20 (0.03)
2018tt	0.06001 (0.00015)	0.06116 (0.00015)	58170.00 (0.32)	0.72 (0.14)	0.015 (0.017)	17.86 (0.03)
2019aox	0.03160 (0.00015)	0.03130 (0.00015)	58533.41 (0.07)	0.86 (0.13)	0.020 (0.020)	16.21 (0.05)
2019bka	0.02400 (0.01000)	0.02509 (0.01000)	58555.32 (0.24)	−1.30 (0.21)	−0.018 (0.047)	15.41 (0.07)
2019cpe	0.04878 (0.00010)	0.04994 (0.00010)	58583.87 (0.09)	−0.26 (0.07)	0.029 (0.016)	17.27 (0.03)
2019dfa	0.02639 (0.00001)	0.02745 (0.00001)	58597.28 (0.06)	−0.07 (0.07)	0.133 (0.018)	16.30 (0.03)
2019dwq	0.02765 (0.00019)	0.02833 (0.00019)	58610.07 (0.07)	0.05 (0.07)	−0.026 (0.016)	15.88 (0.03)
2019fzm	0.02315 (0.00001)	0.02384 (0.00001)	58640.91 (0.29)	−0.10 (0.10)	0.117 (0.018)	15.87 (0.04)
2019gbx	0.01310 (0.00010)	0.01422 (0.00010)	58647.49 (0.08)	−1.83 (0.09)	−0.042 (0.020)	14.33 (0.03)
2019gcw	0.03500 (0.00008)	0.03557 (0.00008)	58645.54 (0.14)	−2.44 (0.19)	0.060 (0.019)	16.94 (0.03)
2019gf	0.06683 (0.00015)	0.06768 (0.00015)	58498.77 (0.17)	1.19 (0.14)	−0.046 (0.018)	17.64 (0.04)
2019jf	0.04138 (0.00015)	0.04235 (0.00015)	58501.61 (0.07)	−2.03 (0.09)	0.026 (0.018)	17.20 (0.03)
2019kcx	0.02484 (0.00001)	0.02603 (0.00001)	58676.10 (0.41)	0.65 (0.20)	−0.216 (0.030)	15.72 (0.05)
2019lqv	0.03357 (0.00016)	0.03261 (0.00016)	58693.36 (0.17)	−1.52 (0.15)	0.424 (0.030)	17.33 (0.03)
2019lrc	0.03426 (0.00009)	0.03305 (0.00009)	58692.63 (0.17)	−2.26 (0.13)	0.153 (0.023)	17.27 (0.06)
2019nhy	0.05497 (0.00010)	0.05474 (0.00010)	58717.59 (0.30)	−1.45 (0.24)	0.075 (0.027)	17.82 (0.06)
2019ons	0.03701 (0.00015)	0.03594 (0.00015)	58735.18 (0.07)	1.61 (0.10)	0.168 (0.017)	16.81 (0.03)
2019teo	0.03724 (0.00001)	0.03608 (0.00001)	58793.12 (0.06)	0.04 (0.09)	−0.010 (0.019)	16.63 (0.04)
2019vju	0.01287 (0.00002)	0.01408 (0.00002)	58819.93 (0.02)	−0.38 (0.05)	0.568 (0.017)	16.48 (0.03)
2019vnj	0.02470 (0.00001)	0.02593 (0.00001)	58819.53 (0.13)	0.80 (0.10)	0.013 (0.019)	15.90 (0.04)
2020dhj	0.04417 (0.00001)	0.04479 (0.00001)	58920.96 (0.73)	3.04 (0.84)	0.023 (0.031)	16.96 (0.03)

Table 3.5 (cont'd)

SN	$z_{\rm helio}$	$z_{\rm CMB}$	Peak MJD	x_1	c	m_B (mag)

Note. — SSS DR1 light-curve parameters. All data are fit with SALT3. Three SNe Ia were not able to be fit due to the large fitting errors.

3.8 Discussion and Conclusions

We have presented the first data release of the Swope Supernova Survey, corresponding to 111 SNe Ia and 5759 total photometric measurements. CSP-I (Krisciunas et al. 2017) has published light curves for 134 low-redshift SNe Ia, and thus, there are 245 Swope-observed SNe Ia now in the literature.

The SSS continues to observe SNe Ia, and as of March 2024, we have observed 342 SNe Ia.

We primarily draw the SSS SN Ia sample from untargeted SN discovery surveys, such as ASASSN, ATLAS, *Gaia*, PSST, YSE, and ZTF. This selection is similar to those of the high-redshift surveys, which will reduce systematic biases due to selection effects during cosmology analyses. Additionally, we obtain host-galaxy redshift measurements and SN Ia spectra for almost all of the DR1 SNe to have more precise measurements of the cosmic expansion history and to ensure a pure sample.

Most of the 111 SNe Ia in this work have been observed in the *BVgri* filters, providing broad wavelength coverage. Our five photometric bands are, along with CSP and CfA data, the most bands published for a low-redshift SN survey (Scolnic et al. 2022). Even though we possess observations in all five bands for all 111 SNe Ia in this

data release, six are published with just $Vgri$ data, while 14 are with Vri data. The missing bands do not have enough stars to build a PSF, but we release the remaining bands nonetheless since they may be helpful for cosmology analyses. Future work will include photometry in all five bands for all SNe Ia. For the SN Ia light curves presented here, we derive light-curve parameters and distance estimates, and we create a Hubble diagram with 76 SN Ia after several quality cuts, with an intrinsic scatter of 0.110 mag.

Additionally, Phillips et al. (2019) describe the CSP-II survey and the 125 low-redshift SNe Ia it observed (however, the light curves have not yet been made publicly available). Swope has thus observed ∼342 SNe Ia in recent years using the same camera and filters, and through the legacy of CSP, we will produce a large and homogenous sample of SNe Ia that will be useful for cosmology, and present high-fidelity, high-cadence, six-band photometry for these objects. These objects, many of which were inaccessible to Northern telescopes, will be a critical contribution to the total cosmological sample of SNe Ia, which currently has ∼1000 SNe Ia (Scolnic et al. 2022). This homogenous sample from the same telescope will provide ∼75% of the low-redshift SN Ia mission success; however, other samples are also available and could supplement the dataset. Since CSP reported their photometry in Vega magnitudes, we note that a prior application of AB offsets between data sets is necessary before combining all the Swope SN observations, and will be performed in future work.

A focus of SSS is the calibration of the data. CSP already went to great lengths to characterize the Swope photometric system, including in-situ measurements of the filter throughput (Rheault et al. 2014). We have attempted to further improve the calibration by performing photometry with a spatially varying PSF, unique to SSS

among low-redshift samples, and tying Swope to the Pan-STARRS and CALSPEC systems.

Our implementation of a spatially varying PSF was necessitated by the correlation of the extendedness of a star (as measured by a fixed PSF) with its position on the detector. We have updated the `photutils` photometry package to calculate a varying PSF. We find that this method reduces the photometric scatter by 31% compared to that of a fixed PSF.

However, this method requires sufficient isolated stars to determine the PSF, and 26 SNe Ia were not included in DR1 because of a lack of sufficient stars. In future work, we will further tune this method and explore options for fields with relatively few appropriate stars. Additionally, the inclusion of the other three amplifiers for each image will quadruple the number of stars on the image, likely increasing the number of SNe that can be included with our current criteria and number of grids over which one can calculate the PSF for those already in DR1.

Our calibration method, SuperCal, determines transformations from the PS1 system to the Swope natural system. We are then able to use the PS1 catalog (Flewelling et al. 2020) to measure the zeropoint of each system. This technique is now the standard in the field and allows for a consistent treatment of different SNe Ia observed by different facilities.

When performing the SuperCal method, one generally uses PS1 as the reference catalog since it has superb internal calibration and covers the majority of the sky in five bands. We have also chosen PS1 as our calibrating catalog. However, the lack of PS1 u band and observations with $\delta < -30^\circ$ restrict what data can be calibrated. As a result,

we excluded *all* u-band data and 42 SNe Ia that were not in the PS1 survey footprint. Future work will examine ways to calibrate these data at the level required to make them cosmologically useful. For instance, calibrating to Southern surveys such as DES or SkyMapper (even as a bootstrap to PS1) or using photometric nights to bootstrap using Swope data in the PS1 footprint or of standard stars could both yield reasonable results.

The efforts performed in this work should lead to smaller systematic uncertainties for cosmological parameters (Brout et al. 2022a; DES Collaboration et al. 2024). We aim to re-observe CSP SNe Ia fields in the future to further improve the calibration of CSP-observed SNe.

The SSS is in continual operation. We are observing newly discovered SNe Ia, ensuring measurements of possible calibrator SNe in the Southern hemisphere, and continuing to obtain template observations for previously observed SNe. Future work will present these new data as well as the u band data for the DR1 sample and light curves for low-declination SNe. These data will represent one of the largest and best-calibrated low-redshift SN Ia samples, providing a path to maximizing the investments in the Rubin Observatory and *Roman Space Telescope*. Finally, the SN Ia data presented here and in future work can be used to study the physics of SN Ia progenitors and explosions, simulate future transient surveys, and train photometric classification algorithms.

Chapter 4

i-band Diversity and Spectral Parameters

4.1 Introduction

Observations of Type Ia supernovae (SNe Ia) have played a pivotal role in understanding the Universe's accelerated expansion (Riess et al. 1998; Perlmutter et al. 1999). To obtain precise cosmological distance measurements from SN Ia observations, these objects have been studied in detail to achieve standardization in their light curves. SN Ia luminosity correlates with their shape and color at optical wavelengths at maximum light (Pskovskii 1978; Phillips 1993; Hamuy et al. 1996; Riess et al. 1996; Tripp 1998); their light curves are powered primarily by the radioactive decay of ^{56}Ni to ^{56}Co and thereafter to ^{56}Fe (Colgate & McKee 1969; Mazzali et al. 2001), where the bolometric luminosity at peak light is proportional to the amount of synthesized ^{56}Ni (Arnett 1982).

However, the near-infrared (NIR) light curves of SNe Ia have a different morphology than those at optical wavelengths: while B-band light curves achieve maximum brightness approximately 20 days after explosion, followed by a slow decline rate (determined by the amount of ^{56}Ni (Phillips 1993; Nugent et al. 1995; Kasen & Woosley 2007)), the NIR light curves (i to K bands) possess a secondary maximum after the initial peak light (Elias et al. 1981; Meikle 2000; Krisciunas et al. 2003).

Using time-dependent radiative transfer calculations, Kasen (2006) showed that the timing and strength of the NIR secondary maximum in SNe Ia arise from the ionization evolution of iron-peak elements in the ejecta. Specifically, the recombination of doubly ionized species such as Fe III and Co III into their singly ionized states (Fe II and Co II) plays a pivotal role. At temperatures near 7000 K, the ejecta become highly efficient at redistributing ultraviolet (UV) and blue photons to longer wavelengths, causing a strong increase in NIR emissivity. This process creates a "fluorescent shell" at the 2→1 ionization edge, which moves inward as a "recombination wave." Once this wave reaches the iron-rich core of the ejecta, the NIR emission increases, leading to the secondary maximum in the luminosity.

Furthermore, Kasen (2006) showed that the NIR light curves are influenced by several factors, such as mixing of ^{56}Ni (earlier interaction with the recombination wave causes the secondary maximum to happen earlier), ^{56}Ni mass (larger size of iron core causes more luminous secondary maxima), and electron-capture elements and the progenitor's metallicity (more iron produced by electron-capture or from progenitor metallicity causes a larger iron core, the recombination wave encounters iron earlier, hastening the secondary maximum).

The i band (7000 Å $< \lambda <$ 8500 Å) has been widely studied to understand its behavior. The timing and strength of the i-band secondary maximum are generally correlated with its decline rate (Hamuy et al. 1996; Riess et al. 1996; Krisciunas et al. 2001; Burns et al. 2014; Dhawan et al. 2015; Phillips et al. 2024). However, SNe Ia with similar decline rates have differences in i-band secondary maximum brightness (Folatelli et al. 2010; Krisciunas et al. 2011; Phillips et al. 2024). This discrepancy causes a problem for SN Ia template fitters, which assume the strength of the secondary maximum is a function of the decline-rate parameter Δm_{15} in B band. In fact, fitting errors can be a function of the strength of the secondary maximum (Folatelli et al. 2010).

Folatelli et al. (2010) also found that while the timing of the secondary maximum strongly correlates with the decline-rate parameter $\Delta m_{15}(B)$, there is no apparent correlation of strength of the secondary maximum and the primary peak or the local minimum between the two maxima. Similarly, Deckers et al. (2024) found that there is a strong correlation between Δm_{15} in the g band and the time of the i-band secondary maximum, but no significant correlation between Δm_{15} in g and the normalized i secondary maximum flux.

There is evidence of an intrinsic i-band secondary maximum luminosity difference between low-mass and high-mass galaxies (Grayling et al. 2024; Grayling & Popovic 2024). Specifically, the authors find there is a magnitude offset in i 20 days post-peak of 0.139 mag at a $> 3\sigma$ significance for galaxies at a mass step of $10^{10} M_{\odot}$. However, Pessi et al. (2022) do not find a correlation between the timing, value, and sign of the i-band light-curve curvature between the primary and secondary maxima

and the host-galaxy masses. Similarly, Rigault et al. (2024) find that the data minus light-curve model residuals are not correlated with host environment.

The SN Ia i-band light curve is the result of the convolution between the SN's spectral energy distribution (SED) and the i-band throughput. If the filter remains the same, any variations in the observed i-band light curve must originate from changes in the SED. The key absorption spectral features in the i-band wavelength range (see Figure 4.1) are the O I triplet (rest wavelength 7773 Å) and the Ca II NIR triplet (rest wavelength 8579 Å) (Kasen 2006; Silverman et al. 2012). Changes in these features, such as in their velocities or equivalent widths, could directly influence the brightness and timing of the i-band light curve, particularly its secondary maximum. In fact, Pessi et al. (2022) found a strong correlation between the change of the i-band light curve concavity between the primary and secondary maxima and the pseudo-equivalent width of the Ca II NIR triplet at maximum light. This conclusion agrees with the theoretical models from Kasen (2006), where the absorbing Ca II NIR lines increase the i-band first and secondary maximum brightness while also delaying the first peak.

The i-band light curve, through its first and secondary maxima and the minimum in between, has been studied using several parametrizations, such as a normalization of the secondary maximum flux to the primary peak's flux (Krisciunas et al. 2001), a direct comparison between the magnitudes and times between these three epochs (Folatelli et al. 2010), a "kink" in curvature between the primary peak and secondary maximum (Pessi et al. 2022), and examining the depth of the region between the minimum and the secondary maximum (Phillips et al. 2024). This work proposes an alternative approach by analyzing model residuals around the minimum and secondary

maximum and comparing them with several spectral measurements.

This chapter is structured as follows. In Section 4.2, we describe the photometric observations analyzed, the individual source surveys, and the combined sample. In Section 4.3, we describe the i-band morphological characteristics and describe the different quality cuts we apply to our sample. Section 4.4 presents the spectral measurements used in our analysis, and Section 4.5 describes the results of combining our photometric and spectral observations. Finally, a discussion of our analysis's results and conclusions are presented in Sections 4.6 and 4.7, respectively.

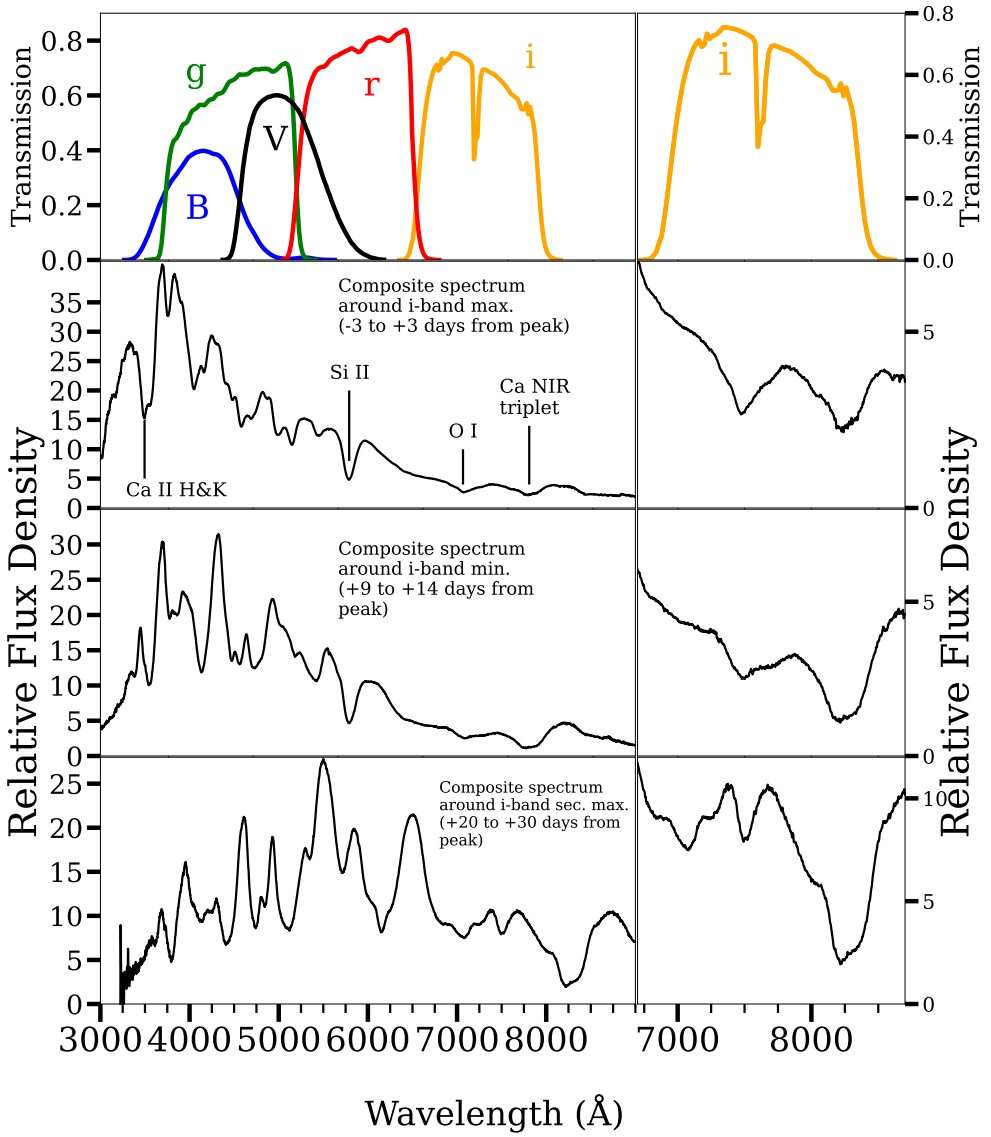

Figure 4.1 Composite spectra of SNe Ia at different phases relative to the i-band light curve, alongside filter transmission curves. The top panel shows the transmission curves for $BVgri$ filters. The bottom three left-hand side panels present the composite spectra near key phases: i-band maximum (-3 to +3 days from i-band peak), i-band minimum (+9 to +14 days), and i-band secondary maximum (+14 to +20 days). Prominent features like Ca II H&K, Si II, O I, and the Ca NIR triplet are labeled to highlight their evolution. The right-hand side panels zoom in on the wavelengths corresponding to the i-band filter, showcasing the temporal evolution of the spectra at these wavelengths.

4.2 Photometric Observations

We utilize data from past and current low-redshift SN Ia surveys, selecting only those with well-calibrated i-band observations and data in at least three additional optical bands, ensuring good wavelength coverage. The surveys used in this paper are the ongoing Swope Supernova Survey, the Carnegie Supernova Project I, and the Harvard-Smithsonian Center for Astrophysics. Details of each survey are presented below.

4.2.1 Swope Supernova Survey (SSS)

The Swope Supernova Survey (SSS, Rojas-Bravo et al., submitted) is an ongoing (starting in the year 2016) low-redshift survey using the 1m Swope telescope at Las Campanas Observatory (see Chapter 2 for a full overview of the survey, and Chapter 3 for the SN Ia data-release details). SSS has observed almost 350 SNe Ia using the same telescope as Carnegie Supernova Project I, of which 111 have been published in Rojas-Bravo et al. (SSS DR1); the remaining SNe Ia will be published in future data releases. SSS uses the Sloan $ugri$ filters and Johnson BV filters (see Figure 2.1). In this work, we only use the $BVgri$ filters since the u-band observations have not been published.

SSS draws most of its observations from untargeted searches, such as the All-Sky Automated Survey for Supernovae (Shappee et al. 2014), Asteroid Terrestrial-impact Last Alert System (ATLAS) (Tonry et al. 2018), *Gaia* Photometric Science Alerts (Hodgkin et al. 2021), Distance Less Than 40 Mpc survey (DLT40) (Tartaglia

et al. 2018), Pan-STARRS Survey for Transients (PSST) (Chambers et al. 2016), Young Supernova Experiment (YSE) (Jones et al. 2021; Aleo et al. 2023), and Zwicky Transient Facility (ZTF) (Bellm et al. 2019). Reductions and calibration are described in Rojas-Bravo et al. (see also Chapter 3). The SNe Ia in SSSDR1 have a redshift range of $0.005 \lesssim z \lesssim 0.130$, and a median redshift of 0.034.

4.2.2 The Carnegie Supernova Project I

The Carnegie Supernova Project I (CSP-I) (Hamuy et al. 2006) observed 134 SNe at low redshift ($0.004 \lesssim z \lesssim 0.08$) through 2004-2009 in optical ($uBVgri$) and near-infrared (YJH) wavelengths using the 1m Swope (same as SSS) and 2.5m du Pont telescopes at Las Campanas Observatory, La Serena, Chile.

Most (55%) of the CSP-I SNe were discovered by two targeted (observations of bright, nearby galaxies) searches: the Lick Observatory Supernova Search (LOSS; Li et al. (2000); Filippenko et al. (2001b); Leaman et al. (2011); Li et al. (2011)) and the Chilean Automatic Supernova Search (Pignata et al. 2009). The remaining CSP-I SNe Ia come from discoveries made by amateur astronomers (36%) and by untargeted surveys (no focus on specific galaxies, 19%).

The filters used by the CSP-I in the Swope telescope were the Sloan Digital Sky Survey (SDSS) $ugri$ and the Johnson B and V filters (Fukugita et al. 1996; Bessell 1990; Rheault et al. 2014). Details of the CSP-I reductions and calibration are described in Krisciunas et al. (2017).

The CSP-I observations were published in three data releases (Contreras et al. 2010; Stritzinger et al. 2011; Krisciunas et al. 2017). In this work, we use the CSP Data

Release 3 (DR3) $BVgri$ light curves originally published in Krisciunas et al. (2017), which contains the final light curves and supersedes all previous CSP-I data releases[13]. From the 134 white dwarf SNe observed, 123 are SNe Ia, 5 are Type Iax SNe (less luminous than normal SNe Ia, high-ionization lines, lower maximum-light velocities Foley et al. (2013), 2 are super-Chandraskhar SNe (Howell et al. 2006), 2 are Type Ia-CSM SNe (Silverman et al. 2013), and 2 are SN 2006bt-like (Foley et al. 2010) objects. This work only analyzes the data from the SNe Ia.

4.2.3 Harvard-Smithsonian Center for Astrophysics (CfA3, CfA4)

The Harvard-Smithsonian Center for Astrophysics SN group[14] observed over 200 low-redshift SNe Ia from 2001-2011 at the F. L. Whipple Observatory (FLWO) in Arizona, United States, published through several data releases. In this work, we employ their third (CfA3, Hicken et al. (2009)) and fourth (CfA4, Hicken et al. (2012)) data releases.

CfA3 consists of 185 SNe Ia observed with the FLWO 1.2 m telescope with three different detectors. In this work, we use the 116 SNe observed on the single-chip CCD KeplerCam[15] detector. This work uses the Johnson B and V filters and the SDSS ri filters. We do not use the other SNe observed by other detectors since they used the Krons-Cousins RI filters. Most CfA3 SNe come from targeted searches, such as LOSS, and amateur astronomers. However, some SNe come from untargeted searches, such as SDSS-II. Most of the discovery surveys used by CfA3 have a limiting magnitude of 19.5

[13] https://csp.obs.carnegiescience.edu/news-items/csp-dr3-photometry-released
[14] https://lweb.cfa.harvard.edu/supernova/index.html
[15] http://linmax.sao.arizona.edu/FLWO/48/kepccd.html

mag. The median redshift of the CfA3 data is 0.027, and the limiting peak magnitude is $\simeq$ 18.5 mag. Detailed information on the calibration and reduction is presented in Hicken et al. (2009).

CfA4 consists of 94 SNe Ia using the same 1.2 m telescope as CfA3. All CfA4 observations were taken with the same $BVri$ filters and the same KeplerCam detector as CfA3. Calibration and reduction details are similar to CfA3 and are described in detail in Hicken et al. (2012). The SN sources are similar to the same search surveys used by CfA3, with most observations coming from targeted searches. The CfA4 objects have a redshift range of $0.0055 \lesssim z \lesssim 0.073$ and a median redshift of 0.029.

4.2.4 The Pantheon+ Supernova Analysis

The Pantheon+ Supernova Analysis (Scolnic et al. (2022) is a recent effort to compile the largest SN Ia dataset. Using SNe Ia from 18 different surveys and a total of 1701 light curves of 1550 unique SNe Ia, the Pantheon+ SN Analysis's primary goal is to infer cosmological parameters. For this reason, they have significantly improved SN redshift measurements and photometric calibration of the different surveys (Brout et al. 2022b).

The CfA3, CfA4, and CSPDR3 light curves are incorporated into the Pantheon+ data set. In this work, we use the Pantheon+ recalibrated light curves and calibration files for these surveys[16], ensuring that we have the most up-to-date and consistent light curves and redshifts available (the SSS data are not included in the Pantheon+ analysis, since their release occurred after the publication of the Pantheon+

[16] https://github.com/PantheonPlusSH0ES/DataRelease

dataset.).

4.2.5 Combined Sample

Our combined sample comprises 386 unique SNe Ia, with 455 SNe accounting for repeated objects across surveys. Specifically, we analyze 111 SNe Ia from the Swope Supernova Survey, 134 from CSP-I, 116 from Cfa3, and 94 from CfA4. In case of duplicate observations, we select the SN from the survey with the best light curve (determined by the number of data points from -10 to +40 from B peak magnitude).

We use SALT (Spectral Adaptive Light-curve Template) (Guy et al. 2007, 2010; Betoule et al. 2014), a widely used empirical spectrophotometric SN Ia model, to fit our light-curve data. SALT represents SN Ia light curves as a combination of spectral energy distribution (SED) components (flux surfaces dependent on wavelength and time), scaled by a color-dependent term governed by a color law similar to that of the Milky Way.

The SALT model is defined by three parameters: x_0 (or m_B, proportional to the log of x_0), the overall flux normalization; x_1, light curve "stretch", representing time-dependent variations as a change in the decline rate from peak brightness in visual wavelengths, and c, a time-independent shift in colors across the entire wavelength range (Taylor et al. 2023). In this work, we fit our data to obtain these three parameters with SALT3, the most recent implementation of the SALT model (Kenworthy et al. 2021a; Taylor et al. 2023), which has significantly more training data (2.5 times larger than SALT2), improved uncertainty estimation, and improved separation of color and light-curve stretch. Additionally, the SALT3 wavelength range spans from 2000 to 11,000 Å,

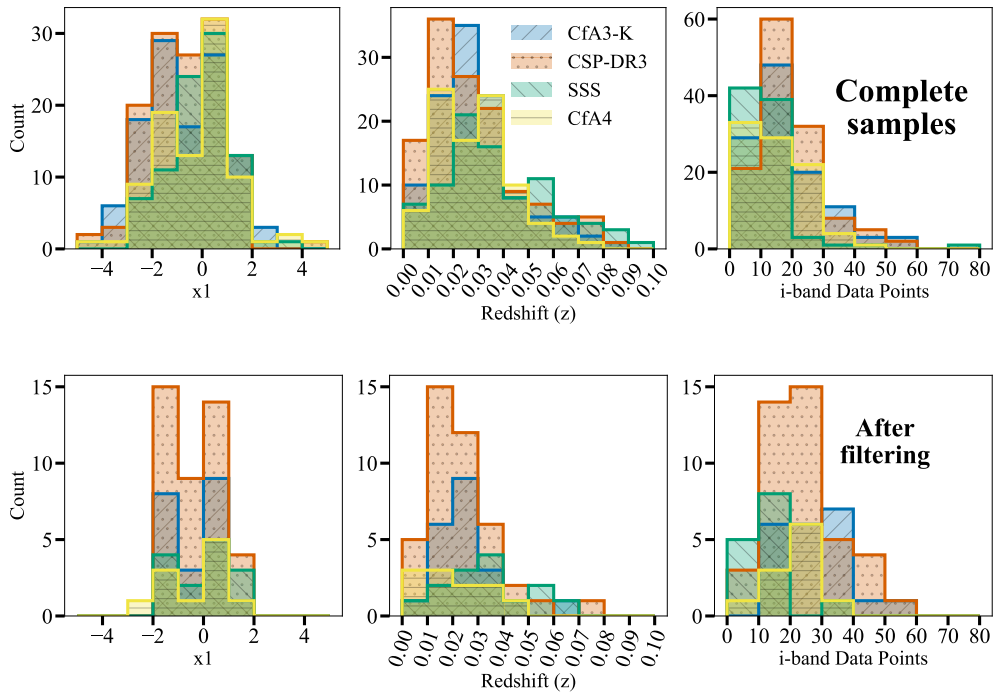

Figure 4.2 Distribution of x_1, redshift, and number of i-band data points for the complete CSP DR3, CfA3-Keplercam, SSS, and CfA4 samples (top panel), and the same samples after the filtering process described in Section 4.3.4 (bottom panel).

1800 Å redder than SALT2.

In Figure 4.2, we show the distributions of the SALT3 parameter x_1, the redshift z, and the number of i-band data points of our combined sample (top panel), and after quality cuts (see Section 4.3.4). We present the complete sample in Table 4.1, with the SALT3 fit parameters x_1, x_0, c, heliocentric redshift, peak Modified Julian Date (MJD) in the B band, and survey source for each SN.

Table 4.1. Summary of SALT3 Fit Parameters for All SNe

SN	x1	c	x0	z_{helio}	Peak MJD	Source
2004dt	-0.9836 (0.0784)	-0.0705 (0.0185)	0.0234 (0.0006)	0.0194 (0.0000)	53239.3160 (0.1990)	CSPDR3
2004ef	-1.3458 (0.2355)	0.0816 (0.0285)	0.0039 (0.0001)	0.0310 (0.0000)	53264.0270 (0.6730)	CfA3-Kepler
2004ef	-1.4146 (0.0427)	0.1037 (0.0137)	0.0041 (0.0001)	0.0310 (0.0000)	53264.7150 (0.0530)	CSPDR3
2004eo	-1.2218 (0.0439)	0.0363 (0.0153)	0.0206 (0.0004)	0.0152 (0.0001)	53278.9020 (0.0570)	CSPDR3
2004ey	0.1677 (0.0445)	-0.0724 (0.0145)	0.0284 (0.0007)	0.0158 (0.0000)	53305.0780 (0.0570)	CSPDR3
2004gc	-0.6745 (0.0658)	0.1429 (0.0177)	0.0043 (0.0002)	0.0319 (0.0001)	53326.5620 (0.2610)	CSPDR3
2004gs	-1.8901 (0.0524)	0.1676 (0.0159)	0.0031 (0.0000)	0.0274 (0.0000)	53356.3010 (0.1350)	CSPDR3
2004gu	1.3338 (0.0947)	0.0905 (0.0146)	0.0025 (0.0000)	0.0456 (0.0000)	53363.0660 (0.1680)	CSPDR3
2005a	-0.4058 (0.0415)	1.0000 (0.0070)	0.0012 (0.0000)	0.0192 (0.0000)	53380.6880 (0.0950)	CSPDR3
2005ag	0.3754 (0.0753)	-0.0378 (0.0142)	0.0009 (0.0000)	0.0795 (0.0000)	53415.4450 (0.0840)	CSPDR3
2005al	-1.2254 (0.0595)	-0.1242 (0.0157)	0.0261 (0.0004)	0.0154 (0.0001)	53431.1760 (0.1740)	CSPDR3
2005am	-1.8233 (0.0658)	0.0239 (0.0190)	0.0801 (0.0018)	0.0073 (0.0001)	53436.1680 (0.2720)	CfA3-Kepler
2005am	-1.8856 (0.0641)	0.0206 (0.0181)	0.0803 (0.0014)	0.0073 (0.0001)	53436.6520 (0.1720)	CSPDR3
2005be	-1.7848 (0.1052)	-0.0631 (0.0298)	0.0041 (0.0002)	0.0336 (0.0000)	53460.7930 (0.4540)	CSPDR3
2005bg	0.5305 (0.1300)	-0.0304 (0.0144)	0.0105 (0.0002)	0.0230 (0.0000)	53470.1910 (0.2900)	CSPDR3
2005bl	-4.5489 (0.7601)	0.5739 (0.0349)	0.0009 (0.0000)	0.0239 (0.0000)	53483.2420 (0.2050)	CSPDR3
2005bo	-1.0965 (0.1202)	0.2297 (0.0159)	0.0126 (0.0002)	0.0139 (0.0000)	53479.1990 (0.1640)	CSPDR3
2005cf	0.0346 (0.0981)	-0.0100 (0.0175)	0.1086 (0.0026)	0.0064 (0.0001)	53534.1800 (0.0680)	CfA3-Kepler
2005dv	-1.1065 (0.7276)	-0.2034 (0.0479)	0.1066 (0.0133)	0.0101 (0.0001)	53590.3520 (0.0670)	CfA3-Kepler
2005el	-1.3002 (0.0930)	-0.1527 (0.0201)	0.0267 (0.0007)	0.0148 (0.0001)	53647.3440 (0.1180)	CSPDR3
2005el	-1.2619 (0.0625)	-0.1304 (0.0196)	0.0262 (0.0007)	0.0148 (0.0001)	53646.4920 (0.1410)	CfA3-Kepler
2005eq	1.3982 (0.1006)	0.0133 (0.0150)	0.0069 (0.0001)	0.0289 (0.0000)	53655.4020 (0.1730)	CSPDR3
2005eq	1.2520 (0.1073)	-0.0002 (0.0177)	0.0069 (0.0001)	0.0289 (0.0000)	53654.7930 (0.1310)	CfA3-Kepler
2005eu	0.8541 (0.1281)	-0.1092 (0.0271)	0.0060 (0.0002)	0.0345 (0.0050)	53660.5860 (0.1370)	CfA3-Kepler
2005ew	1.8865 (0.4218)	-0.2016 (0.0387)	0.1327 (0.0133)	0.0091 (0.0001)	53636.0780 (0.8480)	CfA3-Kepler
2005hc	0.5481 (0.1257)	-0.0070 (0.0175)	0.0025 (0.0000)	0.0459 (0.0000)	53668.2540 (0.0740)	CfA3-Kepler
2005hc	0.8306 (0.0920)	-0.0208 (0.0145)	0.0027 (0.0000)	0.0459 (0.0000)	53668.2770 (0.1190)	CSPDR3
2005hf	-1.7522 (0.1968)	-0.0636 (0.0351)	0.0027 (0.0001)	0.0431 (0.0002)	53664.3790 (0.1460)	CfA3-Kepler
2005hj	1.8731 (0.2859)	-0.0367 (0.0233)	0.0018 (0.0000)	0.0574 (0.0000)	53673.9570 (0.3160)	CfA3-Kepler
2005hj	1.4156 (0.1895)	-0.0022 (0.0179)	0.0019 (0.0000)	0.0574 (0.0000)	53674.9690 (0.3160)	CSPDR3
2005iq	-1.0984 (0.1442)	-0.0783 (0.0185)	0.0043 (0.0001)	0.0340 (0.0001)	53687.8200 (0.1330)	CfA3-Kepler
2005iq	-1.0673 (0.0776)	-0.1015 (0.0152)	0.0045 (0.0001)	0.0340 (0.0001)	53688.3630 (0.0910)	CSPDR3
2005ir	0.7280 (0.2046)	0.0013 (0.0172)	0.0010 (0.0000)	0.0760 (0.0000)	53685.8010 (0.2810)	CSPDR3
2005ir	2.9541 (0.6606)	-0.0408 (0.0316)	0.0009 (0.0000)	0.0760 (0.0000)	53684.2850 (0.2680)	CfA3-Kepler
2005kc	-0.6729 (0.0708)	0.2028 (0.0160)	0.0135 (0.0003)	0.0151 (0.0000)	53698.1950 (0.0650)	CSPDR3
2005kc	-0.3441 (0.0910)	0.2507 (0.0210)	0.0121 (0.0004)	0.0151 (0.0000)	53697.8320 (0.1100)	CfA3-Kepler
2005ke	-2.5212 (0.1464)	0.5332 (0.0415)	0.0251 (0.0012)	0.0049 (0.0000)	53699.3360 (0.1770)	CfA3-Kepler
2005ke	-1.9155 (0.1094)	0.5080 (0.0233)	0.0267 (0.0006)	0.0049 (0.0000)	53699.9450 (0.1220)	CSPDR3
2005ki	-1.4204 (0.0639)	-0.0890 (0.0164)	0.0140 (0.0002)	0.0195 (0.0000)	53705.8320 (0.1240)	CSPDR3
2005ki	-1.6260 (0.1049)	-0.0870 (0.0259)	0.0135 (0.0004)	0.0195 (0.0000)	53705.2810 (0.1620)	CfA3-Kepler
2005ku	0.0203 (0.1965)	0.0915 (0.0176)	0.0021 (0.0000)	0.0452 (0.0000)	53699.5230 (0.3070)	CSPDR3
2005ls	0.6424 (0.1772)	0.3535 (0.0213)	0.0069 (0.0002)	0.0212 (0.0002)	53715.4300 (0.2170)	CfA3-Kepler
2005lu	0.7543 (0.5273)	0.0652 (0.0959)	0.0034 (0.0005)	0.0322 (0.0001)	53710.1800 (1.7560)	CfA3-Kepler
2005lu	1.0953 (0.1254)	0.1848 (0.0191)	0.0029 (0.0001)	0.0322 (0.0001)	53711.8480 (0.4420)	CSPDR3
2005lz	-1.2667 (0.1610)	0.0811 (0.0235)	0.0020 (0.0001)	0.0462 (0.0001)	53736.4410 (0.0880)	CfA3-Kepler
2005m	1.2927 (0.0571)	-0.0081 (0.0133)	0.0098 (0.0001)	0.0248 (0.0001)	53406.6880 (0.0570)	CSPDR3
2005mc	-2.7217 (0.1672)	0.2506 (0.0262)	0.0028 (0.0001)	0.0251 (0.0000)	53734.0230 (0.2530)	CfA3-Kepler
2005mc	-1.9752 (0.0650)	0.2354 (0.0215)	0.0035 (0.0001)	0.0251 (0.0000)	53731.5590 (0.3130)	CSPDR3
2005ms	0.4939 (0.1283)	-0.0438 (0.0205)	0.0080 (0.0002)	0.0252 (0.0000)	53744.0780 (0.1130)	CfA3-Kepler
2005mz	-2.8563 (0.1703)	0.2447 (0.0330)	0.0056 (0.0002)	0.0176 (0.0000)	53745.6050 (0.2410)	CfA3-Kepler
2005na	-0.2449 (0.1085)	-0.0346 (0.0222)	0.0083 (0.0002)	0.0267 (0.0001)	53741.2930 (0.0370)	CfA3-Kepler
2005na	-0.4144 (0.0700)	-0.0659 (0.0144)	0.0093 (0.0002)	0.0267 (0.0001)	53741.5310 (0.1460)	CSPDR3
2005w	-0.4207 (0.0893)	0.1461 (0.0143)	0.0479 (0.0008)	0.0095 (0.0000)	53412.7810 (0.0600)	CSPDR3
2006ac	-0.9984 (0.0998)	0.0522 (0.0196)	0.0078 (0.0002)	0.0231 (0.0000)	53782.0000 (0.1400)	CfA3-Kepler

Table 4.1 (cont'd)

SN	x1	c	x0	z_{helio}	Peak MJD	Source
2006ah	-0.4065 (0.3951)	0.0648 (0.0666)	0.0012 (0.0001)	0.0530 (0.0001)	53774.5430 (0.1610)	CfA3-Kepler
2006ak	-1.1786 (0.1679)	0.0200 (0.0280)	0.0029 (0.0002)	0.0379 (0.0000)	53781.9300 (0.7780)	CfA3-Kepler
2006al	-1.4221 (0.3561)	-0.0984 (0.0342)	0.0010 (0.0001)	0.0678 (0.0000)	53787.3050 (0.9420)	CfA3-Kepler
2006an	0.3565 (0.2078)	-0.0463 (0.0219)	0.0015 (0.0000)	0.0640 (0.0001)	53789.1560 (0.0670)	CfA3-Kepler
2006ar	-0.0283 (0.4421)	0.1548 (0.0234)	0.0058 (0.0001)	0.0225 (0.0000)	53814.3830 (0.3450)	CfA3-Kepler
2006ax	0.3017 (0.0603)	-0.1078 (0.0143)	0.0228 (0.0003)	0.0165 (0.0001)	53827.9840 (0.0560)	CSPDR3
2006ax	0.3910 (0.0707)	-0.0828 (0.0164)	0.0216 (0.0004)	0.0165 (0.0001)	53827.3280 (0.0820)	CfA3-Kepler
2006az	-1.3100 (0.0684)	-0.0740 (0.0169)	0.0059 (0.0001)	0.0310 (0.0000)	53826.8870 (0.1220)	CfA3-Kepler
2006b	-1.0241 (0.1674)	0.3474 (0.0730)	0.0068 (0.0010)	0.0164 (0.0000)	53732.4960 (1.2350)	CfA3-Kepler
2006bb	-2.1882 (0.2861)	-0.0467 (0.0781)	0.0067 (0.0009)	0.0247 (0.0000)	53814.1410 (0.8870)	CfA3-Kepler
2006bd	-2.7417 (0.3681)	0.6335 (0.0878)	0.0006 (0.0000)	0.0255 (0.0001)	53824.1800 (0.7060)	CSPDR3
2006bd	-2.8624 (0.1691)	0.1984 (0.0820)	0.0023 (0.0003)	0.0255 (0.0001)	53812.9880 (0.7470)	CfA3-Kepler
2006bh	-1.5995 (0.0581)	-0.0643 (0.0169)	0.0429 (0.0006)	0.0108 (0.0001)	53833.7070 (0.0170)	CSPDR3
2006bk	0.6328 (0.1331)	0.1493 (0.0283)	0.0037 (0.0002)	0.0494 (0.0000)	53824.8870 (0.5270)	CfA3-Kepler
2006bq	-1.5314 (0.1016)	0.0536 (0.0197)	0.0076 (0.0002)	0.0227 (0.0001)	53847.9410 (0.2960)	CfA3-Kepler
2006br	-0.4059 (0.1621)	0.8337 (0.0273)	0.0006 (0.0000)	0.0247 (0.0000)	53850.9020 (0.4080)	CSPDR3
2006br	3.0376 (2.1746)	-0.0262 (0.0351)	0.0033 (0.0008)	0.0247 (0.0000)	53824.0200 (1.2910)	CfA3-Kepler
2006bt	-0.2007 (0.0955)	0.1576 (0.0167)	0.0039 (0.0001)	0.0321 (0.0000)	53858.9220 (0.1180)	CSPDR3
2006bt	0.1269 (0.0955)	0.1083 (0.0167)	0.0038 (0.0001)	0.0321 (0.0000)	53858.5080 (0.1770)	CfA3-Kepler
2006bu	3.0529 (0.7584)	-0.1075 (0.0375)	0.0012 (0.0001)	0.0840 (0.0060)	53850.6250 (1.5230)	CfA3-Kepler
2006bw	-1.7512 (0.1961)	-0.0117 (0.0556)	0.0046 (0.0004)	0.0300 (0.0000)	53847.8950 (0.7310)	CfA3-Kepler
2006bz	-4.0574 (0.3647)	0.5382 (0.0285)	0.0011 (0.0000)	0.0281 (0.0002)	53862.6760 (0.0380)	CfA3-Kepler
2006cc	0.3303 (0.0797)	0.3591 (0.0165)	0.0017 (0.0000)	0.0330 (0.0002)	53873.9880 (0.0690)	CfA3-Kepler
2006cf	-0.4378 (0.2893)	-0.0815 (0.0324)	0.0034 (0.0001)	0.0415 (0.0000)	53874.4060 (0.6130)	CfA3-Kepler
2006cg	-2.1196 (0.5120)	0.1136 (0.0509)	0.0058 (0.0006)	0.0279 (0.0000)	53865.9180 (1.1240)	CfA3-Kepler
2006cj	1.9520 (0.8465)	-0.0729 (0.0219)	0.0013 (0.0000)	0.0677 (0.0000)	53877.0080 (1.4330)	CfA3-Kepler
2006cm	0.4460 (0.1471)	0.9245 (0.0203)	0.0014 (0.0000)	0.0163 (0.0000)	53884.5350 (0.2630)	CfA3-Kepler
2006cp	0.3933 (0.1207)	0.0698 (0.0233)	0.0092 (0.0002)	0.0223 (0.0000)	53897.6520 (0.1100)	CfA3-Kepler
2006cq	0.2270 (0.5831)	0.0167 (0.0229)	0.0021 (0.0000)	0.0484 (0.0000)	53890.2270 (0.5250)	CfA3-Kepler
2006cs	-3.7253 (0.5897)	-0.1231 (0.3816)	0.0046 (0.0025)	0.0237 (0.0000)	53880.4140 (1.8250)	CfA3-Kepler
2006ct	-2.2820 (0.8857)	-0.3019 (0.2232)	0.0060 (0.0020)	0.0314 (0.0000)	53883.2850 (2.1680)	CfA4-p1
2006cz	1.5668 (0.2778)	0.1743 (0.0346)	0.0034 (0.0001)	0.0418 (0.0002)	53906.1410 (0.4170)	CfA3-Kepler
2006d	-1.5788 (0.0582)	0.0241 (0.0163)	0.0508 (0.0008)	0.0085 (0.0001)	53758.0160 (0.1160)	CSPDR3
2006d	-1.5404 (0.0924)	0.0039 (0.0201)	0.0507 (0.0011)	0.0085 (0.0001)	53757.4300 (0.1500)	CfA3-Kepler
2006dd	0.6670 (1.6578)	-0.1079 (0.1307)	0.0285 (0.0050)	0.0059 (0.0000)	53986.4570 (1.0210)	CSPDR3
2006ef	-1.4284 (0.1118)	-0.0473 (0.0260)	0.0152 (0.0006)	0.0178 (0.0000)	53970.4690 (0.3660)	CSPDR3
2006ef	-1.0312 (0.2163)	-0.0566 (0.0419)	0.0150 (0.0013)	0.0178 (0.0000)	53969.2270 (0.7730)	CfA3-Kepler
2006ej	-1.4180 (0.0839)	-0.0390 (0.0243)	0.0120 (0.0003)	0.0204 (0.0000)	53976.5900 (0.3690)	CSPDR3
2006ej	-1.0453 (0.0883)	0.0038 (0.0221)	0.0113 (0.0003)	0.0204 (0.0000)	53975.6020 (0.2420)	CfA3-Kepler
2006em	-2.0607 (0.2026)	0.2959 (0.0662)	0.0026 (0.0003)	0.0192 (0.0001)	53965.1170 (0.1590)	CfA3-Kepler
2006en	-0.0184 (0.1598)	0.0358 (0.0239)	0.0044 (0.0002)	0.0320 (0.0000)	53972.5740 (0.6110)	CfA3-Kepler
2006eq	-1.9667 (0.1000)	0.0935 (0.0316)	0.0012 (0.0001)	0.0494 (0.0000)	53974.9340 (0.4930)	CSPDR3
2006et	0.7528 (0.1600)	0.1502 (0.0229)	0.0093 (0.0003)	0.0224 (0.0001)	53994.5980 (0.1750)	CfA3-Kepler
2006et	0.8023 (0.0670)	0.1477 (0.0146)	0.0093 (0.0001)	0.0224 (0.0001)	53994.7540 (0.0650)	CSPDR3
2006eu	-1.2559 (0.2083)	0.0347 (0.0391)	0.0114 (0.0008)	0.0236 (0.0002)	53974.2420 (0.0500)	CfA3-Kepler
2006ev	-1.3186 (0.1000)	0.1091 (0.0223)	0.0034 (0.0001)	0.0287 (0.0000)	53990.0160 (0.3700)	CSPDR3
2006ev	-1.3855 (0.2293)	0.0227 (0.0642)	0.0040 (0.0005)	0.0287 (0.0000)	53988.4920 (1.2390)	CfA3-Kepler
2006fw	-1.3776 (0.2025)	0.0241 (0.0289)	0.0006 (0.0000)	0.0836 (0.0000)	54004.5200 (0.1470)	CSPDR3
2006gj	-2.1646 (0.1052)	0.2849 (0.0200)	0.0020 (0.0000)	0.0283 (0.0001)	54000.1800 (0.2290)	CSPDR3
2006gj	-2.1620 (0.2001)	0.3389 (0.0322)	0.0019 (0.0001)	0.0283 (0.0001)	53999.5160 (0.3350)	CfA3-Kepler
2006gr	0.8299 (0.0985)	0.0899 (0.0175)	0.0036 (0.0001)	0.0347 (0.0000)	54013.3710 (0.0960)	CfA3-Kepler
2006h	-3.0556 (0.1932)	-0.1355 (0.0959)	0.0119 (0.0018)	0.0144 (0.0001)	53743.0660 (0.6730)	CfA3-Kepler
2006ha	2.5218 (1.6671)	0.9975 (1.8162)	0.0003 (0.0000)	0.0308 (0.0000)	54013.0820 (1.0380)	CfA3-Kepler
2006hb	-2.3731 (0.1254)	0.0595 (0.0351)	0.0155 (0.0008)	0.0150 (0.0001)	54001.5270 (0.3980)	CfA3-Kepler

Table 4.1 (cont'd)

SN	x1	c	x0	z_{helio}	Peak MJD	Source
2006hb	-2.1259 (0.1013)	0.0143 (0.0282)	0.0173 (0.0007)	0.0150 (0.0001)	54001.0000 (0.3480)	CSPDR3
2006hx	-0.3987 (0.1317)	0.0374 (0.0227)	0.0024 (0.0001)	0.0454 (0.0000)	54022.5350 (0.1260)	CSPDR3
2006is	2.3757 (0.2502)	-0.0211 (0.0278)	0.0072 (0.0004)	0.0314 (0.0001)	54007.4770 (0.8010)	CfA3-Kepler
2006is	1.8478 (0.1563)	-0.0591 (0.0191)	0.0081 (0.0002)	0.0314 (0.0001)	54007.4570 (0.1700)	CSPDR3
2006je	-2.2540 (0.2712)	0.0536 (0.0968)	0.0021 (0.0003)	0.0379 (0.0000)	54010.8160 (0.8830)	CfA3-Kepler
2006ke	-2.5025 (0.2090)	0.5271 (0.0968)	0.0013 (0.0002)	0.0172 (0.0000)	54018.4140 (0.7940)	CfA3-Kepler
2006kf	-2.3187 (0.1371)	-0.0579 (0.0316)	0.0095 (0.0005)	0.0200 (0.0000)	54041.2460 (0.2840)	CfA3-Kepler
2006kf	-2.0817 (0.1003)	0.0011 (0.0225)	0.0095 (0.0004)	0.0200 (0.0000)	54041.7270 (0.1520)	CSPDR3
2006le	0.9390 (0.0778)	-0.0609 (0.0242)	0.0224 (0.0015)	0.0174 (0.0000)	54048.4410 (0.0720)	CfA3-Kepler
2006lf	-1.4124 (0.0909)	-0.1421 (0.0455)	0.0436 (0.0064)	0.0132 (0.0000)	54045.2930 (0.1060)	CfA3-Kepler
2006lu	0.3245 (0.1102)	-0.0940 (0.0196)	0.0023 (0.0001)	0.0534 (0.0001)	54036.1880 (0.4900)	CSPDR3
2006mo	-2.0635 (0.1516)	0.0433 (0.0285)	0.0024 (0.0001)	0.0372 (0.0002)	54047.5590 (0.4290)	CfA3-Kepler
2006mp	0.7321 (0.2840)	0.0156 (0.0194)	0.0092 (0.0002)	0.0230 (0.0050)	54054.1170 (0.1750)	CfA3-Kepler
2006mr	-2.6714 (0.2228)	0.4531 (0.0349)	0.0159 (0.0005)	0.0059 (0.0000)	54050.8710 (0.5100)	CSPDR3
2006n	-1.9719 (0.1045)	-0.0342 (0.0200)	0.0205 (0.0006)	0.0142 (0.0001)	53760.6130 (0.2570)	CfA3-Kepler
2006nz	-4.5929 (1.2006)	0.2379 (0.0552)	0.0013 (0.0001)	0.0382 (0.0000)	54058.2030 (0.4400)	CfA3-Kepler
2006oa	1.4843 (0.3022)	0.0015 (0.0202)	0.0016 (0.0000)	0.0626 (0.0000)	54067.0660 (0.1760)	CfA3-Kepler
2006ob	-2.0537 (0.1460)	-0.0065 (0.0244)	0.0012 (0.0000)	0.0586 (0.0000)	54063.7620 (0.2910)	CSPDR3
2006ob	-2.5100 (0.2364)	0.0129 (0.0236)	0.0012 (0.0000)	0.0586 (0.0000)	54063.4650 (0.2160)	CfA3-Kepler
2006on	0.7185 (0.7498)	0.1010 (0.0442)	0.0009 (0.0000)	0.0719 (0.0000)	54064.3440 (0.7510)	CfA3-Kepler
2006or	-1.1519 (0.4659)	0.1947 (0.1448)	0.0044 (0.0010)	0.0210 (0.0000)	54056.7700 (1.7900)	CfA3-Kepler
2006os	-0.7689 (0.0891)	0.3428 (0.0167)	0.0020 (0.0001)	0.0328 (0.0002)	54065.5940 (0.1820)	CSPDR3
2006os	-1.5700 (0.2179)	0.4004 (0.0310)	0.0019 (0.0001)	0.0328 (0.0002)	54065.5390 (0.1650)	CfA3-Kepler
2006ot	-1.4762 (1.3777)	0.2878 (0.0321)	0.0012 (0.0000)	0.0531 (0.0001)	54067.8200 (1.2030)	CSPDR3
2006ot	-1.7394 (0.3309)	0.1612 (0.0511)	0.0014 (0.0001)	0.0531 (0.0001)	54066.0120 (0.0350)	CfA3-Kepler
2006ou	2.8397 (1.1541)	0.1684 (0.1110)	0.0025 (0.0004)	0.0135 (0.0000)	54082.7110 (0.5400)	CfA4-p1
2006py	0.2195 (0.2970)	0.0172 (0.0190)	0.0016 (0.0000)	0.0579 (0.0000)	54071.2890 (0.3830)	CSPDR3
2006qo	0.4837 (0.0849)	0.1908 (0.0181)	0.0041 (0.0001)	0.0284 (0.0001)	54083.0390 (0.1060)	CfA3-Kepler
2006s	0.9494 (0.1046)	0.0428 (0.0179)	0.0042 (0.0001)	0.0322 (0.0000)	53770.4300 (0.1360)	CfA3-Kepler
2006sr	-1.3160 (0.1461)	-0.0037 (0.0200)	0.0078 (0.0002)	0.0243 (0.0000)	54092.7810 (0.2240)	CfA3-Kepler
2006td	-1.3829 (0.1737)	0.1137 (0.0198)	0.0113 (0.0003)	0.0159 (0.0001)	54099.0230 (0.3180)	CfA3-Kepler
2006te	-0.0156 (0.1302)	-0.0653 (0.0242)	0.0054 (0.0002)	0.0316 (0.0000)	54097.2190 (0.5010)	CfA3-Kepler
2006x	-0.8277 (0.0817)	1.0000 (0.0211)	0.0213 (0.0002)	0.0053 (0.0000)	53786.8520 (0.0790)	CSPDR3
2006x	-0.6097 (0.0991)	1.0000 (0.0040)	0.0217 (0.0002)	0.0053 (0.0000)	53786.3480 (0.0620)	CfA3-Kepler
2007a	0.6061 (0.1830)	0.1434 (0.0168)	0.0120 (0.0002)	0.0176 (0.0001)	54113.8010 (0.1220)	CSPDR3
2007a	0.4826 (0.2673)	0.0780 (0.0302)	0.0125 (0.0005)	0.0176 (0.0001)	54113.2970 (0.1880)	CfA4-p1
2007ae	1.7655 (0.3477)	0.0162 (0.0249)	0.0017 (0.0001)	0.0650 (0.0004)	54153.2700 (0.8700)	CfA3-Kepler
2007af	-0.5598 (0.0499)	0.0503 (0.0146)	0.1253 (0.0018)	0.0055 (0.0000)	54175.1210 (0.0530)	CSPDR3
2007af	-0.3838 (0.0463)	0.0561 (0.0154)	0.1235 (0.0020)	0.0055 (0.0000)	54174.5660 (0.0660)	CfA3-Kepler
2007ai	1.2181 (0.2452)	0.1862 (0.0280)	0.0033 (0.0002)	0.0318 (0.0001)	54174.3480 (0.3720)	CfA3-Kepler
2007ai	0.9435 (0.1220)	0.2107 (0.0206)	0.0034 (0.0002)	0.0318 (0.0001)	54174.4220 (0.2220)	CSPDR3
2007aj	-0.3388 (0.1110)	-0.0606 (0.0261)	0.0055 (0.0003)	0.0300 (0.0050)	54160.5700 (0.4960)	CfA4-p1
2007al	-2.9404 (0.2490)	-0.0754 (0.1195)	0.0116 (0.0020)	0.0122 (0.0001)	54157.3950 (0.9240)	CfA3-Kepler
2007al	-2.4946 (0.1820)	0.2039 (0.0528)	0.0067 (0.0006)	0.0122 (0.0001)	54160.4530 (0.5180)	CSPDR3
2007ap	-1.7213 (0.1139)	-0.1023 (0.0289)	0.0176 (0.0008)	0.0157 (0.0000)	54167.4220 (0.3450)	CfA3-Kepler
2007ar	-1.5653 (0.2744)	-0.0380 (0.0514)	0.0016 (0.0001)	0.0528 (0.0000)	54165.3870 (0.1520)	CfA3-Kepler
2007as	-0.9109 (0.0737)	0.0532 (0.0170)	0.0148 (0.0004)	0.0176 (0.0005)	54182.0860 (0.1720)	CSPDR3
2007au	-3.4307 (0.2200)	0.1785 (0.0254)	0.0054 (0.0002)	0.0196 (0.0000)	54184.2540 (0.1740)	CfA3-Kepler
2007ax	-3.2398 (0.2305)	-0.0483 (0.1177)	0.0327 (0.0055)	0.0067 (0.0000)	54174.1520 (0.6540)	CfA3-Kepler
2007ax	-2.8208 (0.4906)	0.6108 (0.1291)	0.0071 (0.0003)	0.0067 (0.0000)	54187.8950 (0.4330)	CSPDR3
2007ba	-2.8489 (0.3186)	-0.2791 (0.1291)	0.0047 (0.0008)	0.0347 (0.0000)	54189.6480 (0.1360)	CfA3-Kepler
2007ba	-2.9620 (0.1981)	0.3214 (0.0221)	0.0017 (0.0000)	0.0347 (0.0000)	54197.7850 (0.1550)	CSPDR3
2007bc	-1.2635 (0.0985)	0.0129 (0.0202)	0.0098 (0.0002)	0.0208 (0.0000)	54200.5310 (0.2240)	CfA3-Kepler
2007bc	-1.0732 (0.0669)	0.0114 (0.0159)	0.0105 (0.0001)	0.0208 (0.0000)	54200.9060 (0.1680)	CSPDR3

Table 4.1 (cont'd)

SN	x1	c	x0	z_{helio}	Peak MJD	Source
2007bd	-0.9939 (0.0706)	-0.0758 (0.0172)	0.0058 (0.0001)	0.0304 (0.0001)	54207.2620 (0.0910)	CSPDR3
2007bd	-1.3337 (0.0989)	-0.0296 (0.0190)	0.0053 (0.0001)	0.0304 (0.0001)	54206.5120 (0.1320)	CfA3-Kepler
2007bj	1.2585 (0.2134)	-0.2105 (0.0264)	0.0327 (0.0015)	0.0168 (0.0001)	54199.4530 (0.5540)	CfA4-p1
2007bm	-0.8860 (0.0619)	0.4125 (0.0159)	0.0395 (0.0007)	0.0062 (0.0001)	54225.3090 (0.1980)	CSPDR3
2007bm	-0.6535 (0.0568)	0.4380 (0.0169)	0.0360 (0.0007)	0.0062 (0.0001)	54224.6250 (0.0690)	CfA3-Kepler
2007bz	1.0541 (0.1746)	0.1195 (0.0243)	0.0049 (0.0001)	0.0222 (0.0000)	54214.2270 (0.2030)	CfA3-Kepler
2007ca	0.6749 (0.0618)	0.2278 (0.0149)	0.0102 (0.0002)	0.0141 (0.0000)	54228.1410 (0.0770)	CSPDR3
2007ca	0.5189 (0.1085)	0.2224 (0.0181)	0.0095 (0.0002)	0.0141 (0.0000)	54227.7110 (0.1180)	CfA3-Kepler
2007cb	1.0597 (0.4689)	-0.0781 (0.0671)	0.0052 (0.0006)	0.0366 (0.0001)	54214.7230 (0.9690)	CfA4-p1
2007cc	1.1592 (0.7762)	0.0379 (0.0888)	0.0083 (0.0011)	0.0291 (0.0000)	54215.8750 (0.6980)	CfA4-p1
2007cf	-3.0238 (0.3214)	-0.1818 (0.1605)	0.0029 (0.0007)	0.0329 (0.0001)	54213.4840 (0.9350)	CfA4-p1
2007cg	0.8913 (0.1042)	0.6089 (0.0214)	0.0013 (0.0000)	0.0332 (0.0001)	54228.0310 (0.3990)	CSPDR3
2007cg	-0.2020 (0.4720)	-0.2230 (0.0448)	0.0067 (0.0007)	0.0332 (0.0001)	54209.7460 (0.1590)	CfA3-Kepler
2007ci	-2.7462 (0.1562)	0.0608 (0.0279)	0.0099 (0.0003)	0.0218 (0.0000)	54246.7380 (0.1060)	CfA3-Kepler
2007cn	5.0000 (1.2228)	0.3408 (0.1230)	0.0005 (0.0001)	0.0253 (0.0006)	54255.2930 (0.8870)	CfA4-p1
2007co	-0.1394 (0.0943)	0.0889 (0.0166)	0.0056 (0.0001)	0.0270 (0.0001)	54265.1990 (0.1010)	CfA3-Kepler
2007cq	-0.2300 (0.2189)	-0.0068 (0.0195)	0.0101 (0.0003)	0.0260 (0.0001)	54281.0660 (0.1170)	CfA3-Kepler
2007cs	1.6037 (0.9523)	1.0000 (0.2932)	0.0019 (0.0001)	0.0175 (0.0000)	54275.5940 (1.1970)	CfA4-p1
2007ev	1.5013 (0.4956)	0.3764 (0.0660)	0.0009 (0.0001)	0.0428 (0.0007)	54281.0900 (1.2820)	CfA4-p1
2007f	0.6312 (0.0762)	-0.0438 (0.0160)	0.0101 (0.0002)	0.0236 (0.0000)	54123.9140 (0.0880)	CfA3-Kepler
2007fb	-1.8301 (0.3167)	-0.1161 (0.0273)	0.0142 (0.0005)	0.0180 (0.0000)	54288.4140 (0.5570)	CfA4-p1
2007fq	-1.7658 (2.6854)	0.3206 (0.1820)	0.0006 (0.0002)	0.0425 (0.0001)	54293.7420 (4.7670)	CfA4-p1
2007fs	-0.8855 (2.9051)	-0.0603 (0.0449)	0.0211 (0.0013)	0.0174 (0.0001)	54296.5620 (1.2180)	CfA4-p1
2007h	0.0734 (0.2105)	0.3207 (0.0358)	0.0011 (0.0000)	0.0426 (0.0002)	54109.0310 (0.2060)	CfA3-Kepler
2007hg	0.6298 (0.8416)	-0.1921 (0.0521)	0.0087 (0.0012)	0.0293 (0.0002)	54320.7070 (1.7840)	CfA4-p1
2007hj	-2.3804 (0.0921)	0.1623 (0.0195)	0.0136 (0.0003)	0.0141 (0.0001)	54349.0080 (0.2170)	CSPDR3
2007hj	-2.2274 (0.1059)	0.1379 (0.0205)	0.0137 (0.0004)	0.0141 (0.0001)	54349.1840 (0.2500)	CfA4-p1
2007hu	-1.2991 (0.3648)	0.2157 (0.0567)	0.0019 (0.0001)	0.0352 (0.0000)	54352.6330 (0.0390)	CfA4-p1
2007hx	0.5279 (0.1974)	0.1134 (0.0199)	0.0005 (0.0000)	0.0794 (0.0000)	54354.2930 (0.4540)	CSPDR3
2007if	0.9293 (0.2274)	-0.0584 (0.0379)	0.0042 (0.0003)	0.0745 (0.0001)	54343.7030 (0.7630)	CSPDR3
2007if	1.2753 (0.3321)	-0.0311 (0.0345)	0.0041 (0.0002)	0.0745 (0.0001)	54342.4380 (0.0740)	CfA4-p1
2007ir	-1.1353 (0.6563)	0.2768 (0.1682)	0.0008 (0.0002)	0.0353 (0.0002)	54343.3480 (2.3700)	CfA4-p1
2007is	-0.4623 (0.2031)	0.0321 (0.0261)	0.0061 (0.0002)	0.0295 (0.0000)	54366.9220 (0.5640)	CfA4-p1
2007jd	-0.8086 (0.1534)	0.1131 (0.0194)	0.0006 (0.0000)	0.0727 (0.0000)	54362.2070 (0.3930)	CSPDR3
2007jg	-0.4336 (0.0976)	0.0076 (0.0159)	0.0028 (0.0001)	0.0371 (0.0000)	54366.9840 (0.1560)	CSPDR3
2007jh	-2.1410 (0.1908)	0.2459 (0.0300)	0.0011 (0.0000)	0.0408 (0.0000)	54365.7190 (0.3880)	CSPDR3
2007kd	1.6426 (0.3771)	0.1856 (0.0500)	0.0048 (0.0002)	0.0242 (0.0000)	54364.2190 (0.1010)	CfA4-p1
2007kf	5.0000 (2.0610)	0.6544 (0.0951)	0.0006 (0.0001)	0.0467 (0.0050)	54364.4180 (1.7770)	CfA4-p1
2007kg	4.7970 (2.0972)	0.1130 (0.1051)	0.0187 (0.0031)	0.0067 (0.0050)	54373.8200 (2.7020)	CfA4-p1
2007kh	1.5302 (0.4034)	0.1465 (0.0528)	0.0017 (0.0001)	0.0500 (0.0050)	54364.6210 (0.0750)	CfA4-p1
2007kk	0.9092 (0.1657)	-0.0097 (0.0212)	0.0037 (0.0001)	0.0418 (0.0002)	54383.9650 (0.3230)	CfA4-p1
2007le	0.3400 (0.0535)	0.2755 (0.0144)	0.0638 (0.0009)	0.0067 (0.0000)	54399.8790 (0.0590)	CSPDR3
2007le	0.3970 (0.0679)	0.2560 (0.0162)	0.0659 (0.0011)	0.0067 (0.0000)	54399.2770 (0.0690)	CfA4-p1
2007mm	-3.9075 (0.3632)	0.4488 (0.0311)	0.0003 (0.0000)	0.0665 (0.0000)	54392.2500 (0.2560)	CSPDR3
2007n	-3.0049 (0.1690)	0.3371 (0.0804)	0.0044 (0.0005)	0.0129 (0.0000)	54113.3320 (0.6120)	CSPDR3
2007n	-3.5223 (0.1609)	0.3577 (0.0911)	0.0048 (0.0006)	0.0129 (0.0000)	54113.3090 (0.5980)	CfA3-Kepler
2007nq	-1.8150 (0.0857)	-0.0136 (0.0187)	0.0025 (0.0000)	0.0439 (0.0001)	54398.8200 (0.2040)	CSPDR3
2007nq	-1.7375 (0.2014)	-0.0608 (0.0306)	0.0026 (0.0001)	0.0439 (0.0001)	54398.2730 (0.5530)	CfA4-p1
2007o	-0.4057 (0.1052)	-0.0303 (0.0215)	0.0043 (0.0001)	0.0369 (0.0000)	54125.3670 (0.0730)	CfA3-Kepler
2007ob	-0.4333 (0.2874)	0.2419 (0.0353)	0.0028 (0.0002)	0.0339 (0.0000)	54402.0620 (1.0660)	CfA4-p1
2007ol	-2.6462 (0.6035)	-0.0816 (0.0262)	0.0014 (0.0000)	0.0559 (0.0000)	54413.6210 (0.2720)	CSPDR3
2007on	-2.9620 (0.2077)	0.0853 (0.0243)	0.1411 (0.0030)	0.0049 (0.0001)	54420.1990 (0.1540)	CSPDR3
2007qe	0.8015 (0.0786)	0.0587 (0.0159)	0.0085 (0.0001)	0.0240 (0.0001)	54429.7270 (0.0700)	CfA3-Kepler
2007r	-1.4399 (0.1266)	-0.0918 (0.0248)	0.0048 (0.0001)	0.0308 (0.0000)	54129.5350 (0.1050)	CfA3-Kepler

Table 4.1 (cont'd)

SN	x1	c	x0	z_{helio}	Peak MJD	Source
2007rx	0.8826 (0.2528)	-0.2332 (0.0386)	0.0119 (0.0008)	0.0323 (0.0040)	54440.1410 (0.8220)	CfA4-p1
2007s	1.0776 (0.0729)	0.3884 (0.0159)	0.0110 (0.0002)	0.0139 (0.0000)	54145.1600 (0.0670)	CSPDR3
2007s	1.2133 (0.0715)	0.3839 (0.0154)	0.0104 (0.0002)	0.0139 (0.0000)	54144.9300 (0.0630)	CfA3-Kepler
2007so	-1.2302 (0.1787)	-0.0503 (0.0299)	0.0061 (0.0003)	0.0298 (0.0002)	54429.8120 (0.2110)	CSPDR3
2007sr	0.0909 (0.0695)	0.0763 (0.0158)	0.1841 (0.0038)	0.0054 (0.0000)	54449.6520 (0.2280)	CSPDR3
2007sr	0.1699 (0.0605)	0.0894 (0.0157)	0.1776 (0.0032)	0.0054 (0.0000)	54448.8790 (0.0860)	CfA3-Kepler
2007ss	-1.2110 (0.1051)	0.2694 (0.0257)	0.0071 (0.0002)	0.0156 (0.0000)	54453.6560 (0.3900)	CfA4-p1
2007st	-1.6290 (0.0771)	0.1045 (0.0197)	0.0108 (0.0002)	0.0211 (0.0000)	54454.7230 (0.0310)	CSPDR3
2007su	0.4473 (0.3662)	0.1981 (0.0311)	0.0040 (0.0002)	0.0278 (0.0000)	54460.0390 (0.7410)	CfA4-p1
2007sw	0.2799 (0.1462)	0.0785 (0.0232)	0.0070 (0.0002)	0.0243 (0.0001)	54468.7810 (0.3190)	CfA4-p1
2007ux	-2.5347 (0.1279)	0.1575 (0.0360)	0.0026 (0.0001)	0.0307 (0.0000)	54465.3050 (0.3690)	CfA4-p1
2007ux	-2.1414 (0.0839)	0.1019 (0.0184)	0.0027 (0.0000)	0.0307 (0.0000)	54465.2030 (0.0120)	CSPDR3
2008a	0.4820 (0.1547)	0.1713 (0.0274)	0.0077 (0.0002)	0.0165 (0.0000)	54480.4220 (0.1800)	CfA4-p1
2008ac	0.2084 (0.4399)	-0.0459 (0.0443)	0.0018 (0.0001)	0.0528 (0.0001)	54503.5550 (0.1380)	CfA4-p1
2008ae	-1.2817 (0.3077)	0.3779 (0.0349)	0.0009 (0.0000)	0.0300 (0.0000)	54512.2230 (0.4070)	CfA4-p1
2008ae	5.0000 (1.3548)	0.7428 (0.1196)	0.0006 (0.0001)	0.0300 (0.0000)	54523.1250 (0.0690)	CSPDR3
2008af	-1.5007 (0.2138)	0.0191 (0.0430)	0.0039 (0.0004)	0.0334 (0.0000)	54502.8120 (1.1210)	CfA3-Kepler
2008ai	-1.7344 (0.8467)	0.5918 (0.0836)	0.0006 (0.0001)	0.0351 (0.0000)	54507.3240 (0.2870)	CfA4-p1
2008ar	-0.0894 (0.0664)	-0.0234 (0.0149)	0.0076 (0.0001)	0.0262 (0.0000)	54535.2460 (0.0900)	CSPDR3
2008ar	0.0224 (0.1030)	-0.0477 (0.0178)	0.0074 (0.0001)	0.0262 (0.0000)	54534.6560 (0.1280)	CfA4-p1
2008at	-1.5398 (0.1831)	0.2380 (0.0448)	0.0020 (0.0001)	0.0347 (0.0002)	54526.7540 (0.8530)	CfA4-p1
2008bc	0.6487 (0.0664)	-0.0756 (0.0179)	0.0294 (0.0013)	0.0151 (0.0001)	54550.4840 (0.0700)	CSPDR3
2008bd	-0.5252 (0.3162)	0.6625 (0.1442)	0.0007 (0.0002)	0.0301 (0.0001)	54531.6950 (2.6780)	CSPDR3
2008bf	0.5255 (0.0631)	-0.1137 (0.0140)	0.0123 (0.0002)	0.0234 (0.0010)	54555.5470 (0.0670)	CSPDR3
2008bf	0.4108 (0.1031)	-0.0208 (0.0174)	0.0116 (0.0002)	0.0234 (0.0010)	54555.0700 (0.1330)	CfA3-Kepler
2008bi	-3.0626 (0.2335)	-0.0324 (0.1423)	0.0092 (0.0020)	0.0135 (0.0007)	54536.1910 (1.1030)	CfA4-p1
2008bi	-2.8844 (0.1246)	0.1130 (0.0586)	0.0079 (0.0007)	0.0135 (0.0007)	54537.0940 (0.4380)	CSPDR3
2008bq	0.2912 (0.0785)	0.0587 (0.0144)	0.0047 (0.0001)	0.0323 (0.0001)	54564.2660 (0.1620)	CSPDR3
2008bt	-2.6243 (0.2102)	0.4331 (0.0229)	0.0047 (0.0001)	0.0153 (0.0001)	54571.2930 (0.3070)	CSPDR3
2008bw	-1.6439 (0.2938)	-0.1665 (0.0611)	0.0050 (0.0004)	0.0327 (0.0000)	54566.3360 (0.0690)	CfA4-p1
2008by	0.5588 (0.3814)	-0.1597 (0.0317)	0.0034 (0.0003)	0.0450 (0.0001)	54574.8790 (1.1250)	CfA4-p1
2008bz	-0.4805 (0.1316)	-0.1084 (0.0173)	0.0015 (0.0000)	0.0602 (0.0000)	54579.8240 (0.2940)	CSPDR3
2008bz	0.0028 (0.3753)	-0.1295 (0.0300)	0.0016 (0.0001)	0.0602 (0.0000)	54577.9570 (0.9430)	CfA4-p1
2008c	-0.6610 (0.0973)	0.1386 (0.0171)	0.0122 (0.0002)	0.0166 (0.0000)	54467.9260 (0.0290)	CSPDR3
2008c	-0.6615 (0.1461)	0.1169 (0.0235)	0.0129 (0.0005)	0.0166 (0.0000)	54467.0510 (0.3790)	CfA4-p1
2008cc	-1.7212 (0.1150)	0.0302 (0.0309)	0.0481 (0.0023)	0.0103 (0.0001)	54573.7070 (0.3350)	CSPDR3
2008cd	-0.9648 (0.1934)	1.0000 (0.0091)	0.0029 (0.0001)	0.0075 (0.0002)	54562.6170 (0.1580)	CfA4-p1
2008cd	-0.6567 (0.3849)	1.0000 (0.0350)	0.0024 (0.0001)	0.0075 (0.0002)	54567.9880 (1.2530)	CSPDR3
2008cf	1.2835 (0.4521)	-0.1295 (0.0242)	0.0036 (0.0001)	0.0460 (0.0001)	54594.9920 (0.8540)	CfA4-p1
2008cf	1.4064 (0.1859)	-0.1058 (0.0188)	0.0036 (0.0001)	0.0460 (0.0001)	54594.7030 (0.4770)	CSPDR3
2008cm	-1.6323 (0.1480)	-0.1798 (0.0199)	0.0126 (0.0003)	0.0111 (0.0001)	54612.7340 (0.2090)	CfA4-p1
2008dr	-2.6745 (0.5942)	-0.4099 (0.2173)	0.0035 (0.0010)	0.0412 (0.0000)	54651.5550 (2.0440)	CfA4-p1
2008ds	1.0782 (0.4506)	-0.1064 (0.0560)	0.0178 (0.0017)	0.0211 (0.0000)	54652.8200 (0.7150)	CfA4-p1
2008dt	-1.3417 (0.2876)	0.1627 (0.0925)	0.0029 (0.0004)	0.0352 (0.0000)	54639.5310 (1.4590)	CfA4-p1
2008ff	1.0867 (0.5298)	0.0272 (0.0232)	0.0173 (0.0006)	0.0192 (0.0001)	54704.5940 (1.0480)	CSPDR3
2008fl	-1.1585 (0.0568)	0.0061 (0.0177)	0.0128 (0.0004)	0.0199 (0.0001)	54721.5510 (0.2450)	CSPDR3
2008fp	0.3356 (0.0548)	0.3842 (0.0167)	0.0642 (0.0022)	0.0057 (0.0001)	54731.3830 (0.0720)	CSPDR3
2008fr	0.4984 (0.0997)	-0.0805 (0.0181)	0.0043 (0.0001)	0.0390 (0.0020)	54734.3160 (0.3680)	CSPDR3
2008fr	0.6166 (0.1409)	-0.0947 (0.0198)	0.0044 (0.0001)	0.0390 (0.0020)	54732.6130 (0.4570)	CfA4-p1
2008fu	-1.4887 (0.1077)	-0.0900 (0.0323)	0.0019 (0.0001)	0.0520 (0.0001)	54733.9100 (0.0770)	CSPDR3
2008fw	0.8917 (0.1230)	-0.0092 (0.0198)	0.0606 (0.0021)	0.0084 (0.0001)	54732.5590 (0.4010)	CSPDR3
2008gb	0.1525 (0.2655)	-0.0140 (0.0249)	0.0034 (0.0001)	0.0370 (0.0001)	54746.9020 (0.5720)	CfA4-p1
2008gg	0.9550 (0.0670)	0.0798 (0.0148)	0.0057 (0.0001)	0.0320 (0.0001)	54749.8480 (0.0180)	CSPDR3
2008gl	-1.2645 (0.0685)	-0.0047 (0.0154)	0.0044 (0.0001)	0.0335 (0.0002)	54768.6520 (0.1450)	CSPDR3

Table 4.1 (cont'd)

SN	x1	c	x0	$z_{\rm helio}$	Peak MJD	Source
2008gl	-1.4379 (0.1357)	-0.0210 (0.0226)	0.0044 (0.0001)	0.0335 (0.0002)	54768.5430 (0.1650)	CfA4-p1
2008go	-0.7166 (0.4156)	0.0232 (0.0173)	0.0014 (0.0000)	0.0623 (0.0001)	54766.5350 (0.3060)	CSPDR3
2008gp	-0.0816 (0.0545)	-0.0908 (0.0149)	0.0063 (0.0001)	0.0330 (0.0002)	54779.7930 (0.0730)	CSPDR3
2008ha	-2.4275 (0.1901)	-0.1863 (0.0854)	0.0054 (0.0008)	0.0046 (0.0000)	54770.7890 (0.8920)	CSPDR3
2008hj	0.2734 (0.0713)	-0.0439 (0.0138)	0.0045 (0.0001)	0.0376 (0.0001)	54802.3790 (0.0720)	CSPDR3
2008hj	0.1014 (0.3767)	-0.0663 (0.0305)	0.0045 (0.0001)	0.0376 (0.0001)	54801.9300 (0.9290)	CfA4-p1
2008hm	0.1871 (0.1326)	0.0054 (0.0271)	0.0118 (0.0008)	0.0197 (0.0001)	54805.2380 (0.2050)	CfA4-p1
2008hs	-2.3796 (0.1514)	0.0403 (0.0364)	0.0081 (0.0004)	0.0191 (0.0001)	54812.6250 (0.1520)	CfA4-p1
2008hu	-1.7104 (0.0964)	-0.0134 (0.0196)	0.0017 (0.0000)	0.0498 (0.0001)	54806.8120 (0.2300)	CSPDR3
2008hv	-1.1660 (0.0607)	-0.0917 (0.0162)	0.0300 (0.0004)	0.0126 (0.0001)	54817.4650 (0.0690)	CSPDR3
2008hv	-1.3461 (0.1067)	-0.1314 (0.0215)	0.0302 (0.0007)	0.0126 (0.0001)	54817.0430 (0.0590)	CfA4-p1
2008ia	-1.2363 (0.0874)	-0.0612 (0.0190)	0.0103 (0.0004)	0.0219 (0.0001)	54813.3240 (0.1760)	CSPDR3
2008j	4.7871 (2.1358)	1.0000 (0.1327)	0.0045 (0.0001)	0.0160 (0.0001)	54494.8050 (1.1790)	CSPDR3
2008l	-1.4800 (0.1605)	-0.1142 (0.0328)	0.0193 (0.0009)	0.0179 (0.0001)	54492.6130 (0.5110)	CfA3-Kepler
2008o	-1.8862 (0.1015)	0.2909 (0.0188)	0.0013 (0.0000)	0.0389 (0.0001)	54491.0310 (0.2460)	CSPDR3
2008q	-1.7739 (1.2390)	-0.1024 (0.0360)	0.0994 (0.0042)	0.0083 (0.0000)	54505.9060 (0.4520)	CfA4-p1
2008r	-2.5327 (0.1098)	0.0525 (0.0212)	0.0188 (0.0004)	0.0132 (0.0001)	54494.4340 (0.1170)	CSPDR3
2008y	-0.4794 (0.2745)	0.0891 (0.0313)	0.0009 (0.0000)	0.0697 (0.0000)	54504.0590 (0.9040)	CfA4-p1
2008z	1.1260 (0.1326)	0.0895 (0.0194)	0.0062 (0.0001)	0.0206 (0.0000)	54515.3980 (0.1020)	CfA4-p1
2009aa	-0.7467 (0.0516)	-0.0399 (0.0144)	0.0070 (0.0001)	0.0271 (0.0002)	54878.9060 (0.0580)	CSPDR3
2009ab	-0.9601 (0.0826)	0.0075 (0.0188)	0.0305 (0.0011)	0.0122 (0.0001)	54883.9020 (0.0930)	CSPDR3
2009ad	0.2204 (0.1045)	-0.0563 (0.0185)	0.0077 (0.0002)	0.0284 (0.0000)	54886.5430 (0.1900)	CfA4-p1
2009ad	0.3493 (0.0758)	-0.0366 (0.0157)	0.0079 (0.0002)	0.0284 (0.0000)	54887.0940 (0.0720)	CSPDR3
2009ag	-0.2230 (0.0571)	0.1592 (0.0185)	0.0338 (0.0015)	0.0087 (0.0000)	54890.1880 (0.1580)	CSPDR3
2009al	-0.5286 (0.0629)	0.1045 (0.0169)	0.0076 (0.0001)	0.0221 (0.0001)	54897.7970 (0.0630)	CSPDR3
2009al	-0.2685 (0.1548)	0.1248 (0.0208)	0.0072 (0.0002)	0.0221 (0.0001)	54897.1880 (0.1470)	CfA4-p1
2009an	-1.3947 (0.1139)	0.0356 (0.0228)	0.0365 (0.0010)	0.0089 (0.0000)	54898.4840 (0.1610)	CfA4-p1
2009bv	0.4404 (0.1540)	-0.0690 (0.0207)	0.0040 (0.0001)	0.0367 (0.0001)	54927.5000 (0.1330)	CfA4-p1
2009cz	0.6841 (0.1091)	0.0006 (0.0163)	0.0121 (0.0002)	0.0223 (0.0000)	54943.9960 (0.0960)	CSPDR3
2009d	0.7253 (0.0657)	-0.0466 (0.0140)	0.0118 (0.0002)	0.0251 (0.0001)	54841.8360 (0.0900)	CSPDR3
2009d	0.4353 (0.1512)	-0.0374 (0.0217)	0.0116 (0.0003)	0.0251 (0.0001)	54841.9800 (0.3860)	CfA4-p1
2009dc	1.8791 (0.2158)	0.0527 (0.0221)	0.0223 (0.0005)	0.0215 (0.0000)	54948.2770 (0.2130)	CSPDR3
2009dc	3.4376 (0.2152)	-0.0092 (0.0194)	0.0205 (0.0005)	0.0215 (0.0000)	54947.7580 (0.2260)	CfA4-p1
2009do	-1.0038 (0.1287)	-0.0294 (0.0205)	0.0032 (0.0001)	0.0396 (0.0000)	54946.4410 (0.3070)	CfA4-p1
2009ds	0.6416 (0.1680)	-0.0412 (0.0252)	0.0145 (0.0004)	0.0191 (0.0001)	54961.0820 (0.2640)	CfA4-p1
2009ds	1.0807 (0.1888)	0.0809 (0.0161)	0.0146 (0.0002)	0.0191 (0.0001)	54962.1330 (0.1450)	CSPDR3
2009f	5.0000 (0.0975)	-0.0979 (0.0710)	0.0119 (0.0011)	0.0129 (0.0001)	54816.5470 (0.8500)	CSPDR3
2009fv	-0.3311 (0.1623)	0.0934 (0.0465)	0.0061 (0.0005)	0.0306 (0.0000)	54988.0980 (0.8420)	CfA4-p1
2009gf	-4.2365 (0.9061)	0.0909 (0.0315)	0.0086 (0.0003)	0.0184 (0.0000)	55002.3710 (0.4200)	CfA4-p1
2009i	1.2454 (0.2086)	0.7009 (0.0182)	0.0011 (0.0000)	0.0262 (0.0000)	54852.5550 (0.1820)	CSPDR3
2009ig	1.3566 (0.2172)	-0.0429 (0.0249)	0.1046 (0.0030)	0.0088 (0.0000)	55079.8120 (0.4490)	CfA4-p2
2009j	-2.0383 (0.2305)	-0.2027 (0.0588)	0.0021 (0.0002)	0.0159 (0.0001)	54837.2500 (0.0610)	CSPDR3
2009jr	0.8193 (0.1156)	0.3682 (0.0196)	0.0070 (0.0002)	0.0166 (0.0002)	55119.8090 (0.2390)	CfA4-p2
2009kk	-1.2637 (0.1070)	-0.0940 (0.0258)	0.0310 (0.0011)	0.0129 (0.0001)	55126.7970 (0.0650)	CfA4-p2
2009kq	-0.0047 (0.1986)	-0.0248 (0.0283)	0.0366 (0.0012)	0.0117 (0.0001)	55155.3440 (0.2830)	CfA4-p2
2009le	0.6597 (0.0924)	0.0795 (0.0157)	0.0169 (0.0002)	0.0181 (0.0001)	55166.4140 (0.0110)	CSPDR3
2009le	0.2040 (0.2870)	0.0389 (0.0369)	0.0174 (0.0008)	0.0181 (0.0001)	55165.9530 (0.1330)	CfA4-p2
2009lf	-1.7761 (0.1139)	-0.0139 (0.0252)	0.0038 (0.0001)	0.0450 (0.0020)	55150.5000 (0.1620)	CfA4-p2
2009na	-0.5666 (0.1358)	-0.0282 (0.0207)	0.0112 (0.0002)	0.0210 (0.0000)	55201.9800 (0.1520)	CfA4-p2
2009nq	-0.5975 (0.9171)	0.0273 (0.0419)	0.0178 (0.0009)	0.0165 (0.0000)	55203.9300 (0.7170)	CfA4-p2
2009p	1.5469 (0.1400)	0.3570 (0.0165)	0.0036 (0.0001)	0.0251 (0.0001)	54868.0040 (0.2470)	CSPDR3
2009y	0.3346 (0.0843)	0.0661 (0.0194)	0.0595 (0.0016)	0.0097 (0.0001)	54876.3630 (0.1740)	CfA4-p1
2009y	0.2642 (0.0583)	0.1243 (0.0152)	0.0585 (0.0012)	0.0097 (0.0001)	54877.4260 (0.0790)	CSPDR3
2010a	0.8430 (0.2197)	0.0366 (0.0399)	0.0112 (0.0004)	0.0216 (0.0000)	55212.6250 (0.1850)	CfA4-p2

Table 4.1 (cont'd)

SN	x1	c	x0	z_{helio}	Peak MJD	Source
2010ag	0.8953 (0.1938)	0.1035 (0.0227)	0.0047 (0.0001)	0.0334 (0.0000)	55271.1170 (0.3860)	CfA4-p2
2010ai	-1.5993 (0.1293)	-0.0914 (0.0277)	0.0092 (0.0003)	0.0183 (0.0000)	55277.0350 (0.1120)	CfA4-p2
2010cr	-2.7637 (1.1083)	-0.2129 (0.3980)	0.0079 (0.0054)	0.0227 (0.0000)	55308.3160 (3.4840)	CfA4-p2
2010dt	-0.3562 (0.6168)	-0.1112 (0.0606)	0.0021 (0.0002)	0.0529 (0.0000)	55361.6950 (0.2170)	CfA4-p2
2010dw	0.8247 (0.2564)	0.0656 (0.0242)	0.0032 (0.0001)	0.0381 (0.0001)	55358.2270 (0.4780)	CfA4-p2
2010h	-1.3130 (0.2074)	-0.1012 (0.0453)	0.0204 (0.0020)	0.0152 (0.0001)	55215.6720 (1.5910)	CfA4-p2
2010y	-2.6065 (0.1379)	-0.0374 (0.0347)	0.0233 (0.0009)	0.0111 (0.0000)	55247.7770 (0.1530)	CfA4-p2
2011iv	-1.9892 (0.0773)	-0.0161 (0.0178)	0.2451 (0.0035)	0.0063 (0.0001)	55905.0740 (0.2130)	CSPDR3
2016cvn	-0.7664 (0.4180)	1.0000 (0.0635)	0.0028 (0.0003)	0.0137 (0.0001)	57553.8790 (1.4010)	SSS
2016cyt	-1.4357 (0.2116)	0.0620 (0.0311)	0.0054 (0.0003)	0.0307 (0.0001)	57580.6370 (0.1760)	SSS
2016gsn	2.2132 (1.1505)	0.2200 (0.0068)	0.0207 (0.0010)	0.0150 (0.0000)	57670.0740 (1.9610)	SSS
2016ivt	0.5824 (0.2804)	0.0400 (0.0064)	0.0083 (0.0004)	0.0271 (0.0000)	57740.7620 (0.6640)	SSS
2016ixb	-1.7141 (0.1168)	0.1468 (0.0306)	0.0039 (0.0002)	0.0283 (0.0001)	57744.7700 (0.3430)	SSS
2016iyv	1.0978 (0.5663)	0.0005 (0.0383)	0.0075 (0.0006)	0.0303 (0.0001)	57750.0430 (0.5710)	SSS
2016jbs	-0.3217 (0.2905)	0.1395 (0.0296)	0.0011 (0.0000)	0.0548 (0.0001)	57757.8520 (0.3350)	SSS
2017aaa	0.9000 (0.1570)	0.0024 (0.0202)	0.0028 (0.0001)	0.0468 (0.0000)	57799.2380 (0.1730)	SSS
2017aac	-0.4365 (0.1003)	-0.0068 (0.0186)	0.0074 (0.0002)	0.0270 (0.0000)	57797.1880 (0.2400)	SSS
2017adj	0.3626 (0.1356)	-0.0079 (0.0267)	0.0062 (0.0004)	0.0316 (0.0001)	57795.1840 (0.6900)	SSS
2017cal	-0.7275 (0.1064)	0.2233 (0.0191)	0.0090 (0.0003)	0.0207 (0.0001)	57819.4960 (0.2760)	SSS
2017cne	-0.4978 (0.3552)	0.6353 (0.0523)	0.0018 (0.0001)	0.0338 (0.0000)	57852.2190 (0.2270)	SSS
2017cpu	0.7843 (0.7169)	0.0830 (0.0821)	0.0021 (0.0003)	0.0544 (0.0000)	57849.0470 (0.0460)	SSS
2017djl	-1.9312 (1.3918)	0.1456 (0.1266)	0.0028 (0.0008)	0.0445 (0.0003)	57877.3750 (1.6370)	SSS
2017drh	-1.5743 (0.2110)	1.0000 (0.0190)	0.0064 (0.0004)	0.0056 (0.0000)	57890.5000 (0.1580)	SSS
2017dys	0.4793 (0.1786)	0.2891 (0.0319)	0.0042 (0.0002)	0.0293 (0.0001)	57886.4450 (0.8300)	SSS
2017erp	-0.2087 (0.2949)	0.1842 (0.0405)	0.0946 (0.0072)	0.0062 (0.0000)	57937.0080 (0.8340)	SSS
2017euz	0.2820 (0.3307)	-0.0313 (0.0474)	0.0027 (0.0002)	0.0502 (0.0001)	57924.7620 (0.2190)	SSS
2017fgc	0.5034 (0.1620)	0.1446 (0.0281)	0.0822 (0.0030)	0.0077 (0.0001)	57960.6560 (0.1050)	SSS
2017fms	-0.4674 (0.8124)	0.0842 (0.0312)	0.0043 (0.0002)	0.0304 (0.0001)	57960.0390 (0.1830)	SSS
2017fmz	-2.0603 (0.7126)	0.0562 (0.0394)	0.0048 (0.0004)	0.0280 (0.0001)	57958.7890 (0.3610)	SSS
2017fnz	1.6120 (2.0051)	0.0622 (0.0535)	0.0010 (0.0001)	0.0810 (0.0050)	57958.7930 (3.1850)	SSS
2017fzw	-2.0059 (0.1392)	0.3729 (0.0504)	0.0622 (0.0052)	0.0054 (0.0001)	57984.6840 (0.5880)	SSS
2017gdg	0.1392 (0.2999)	-0.0524 (0.0480)	0.0007 (0.0001)	0.0888 (0.0003)	57983.2270 (1.3270)	SSS
2017gfl	0.1935 (0.1705)	0.1064 (0.0261)	0.0008 (0.0000)	0.0808 (0.0003)	57994.1090 (0.1350)	SSS
2017gjd	-0.7965 (0.1087)	0.0634 (0.0239)	0.0117 (0.0007)	0.0200 (0.0001)	58001.4650 (0.1170)	SSS
2017glb	-0.8791 (0.1281)	0.0475 (0.0271)	0.0033 (0.0002)	0.0371 (0.0001)	57991.8050 (0.5760)	SSS
2017gwy	-2.2287 (0.1655)	0.1804 (0.0279)	0.0027 (0.0001)	0.0298 (0.0000)	58027.4380 (0.2720)	SSS
2017hdv	0.8326 (0.1406)	0.0043 (0.0235)	0.0020 (0.0001)	0.0564 (0.0001)	58047.0430 (0.1530)	SSS
2017hfv	0.1888 (0.1114)	0.1072 (0.0203)	0.0060 (0.0002)	0.0282 (0.0001)	58042.3050 (0.4420)	SSS
2017hhi	-0.4992 (0.1645)	-0.1495 (0.0227)	0.0020 (0.0001)	0.0537 (0.0100)	58040.1520 (0.1410)	SSS
2017hmf	0.0378 (0.1530)	0.0519 (0.0215)	0.0014 (0.0001)	0.0600 (0.0000)	58055.1410 (0.1350)	SSS
2017hou	1.3718 (0.0908)	0.6623 (0.0262)	0.0017 (0.0001)	0.0169 (0.0000)	58055.4530 (0.1370)	SSS
2017hpa	0.2934 (0.0736)	0.0449 (0.0299)	0.0242 (0.0022)	0.0156 (0.0000)	58066.2380 (0.0840)	SSS
2017hqc	0.4208 (0.0826)	-0.0173 (0.0217)	0.0041 (0.0002)	0.0399 (0.0003)	58064.3240 (0.0810)	SSS
2017htb	1.4949 (0.2690)	0.1639 (0.0207)	0.0060 (0.0002)	0.0268 (0.0000)	58068.6410 (0.1630)	SSS
2017hxc	0.2059 (0.1778)	-0.0006 (0.0201)	0.0020 (0.0001)	0.0590 (0.0001)	58065.6760 (0.3930)	SSS
2017hyx	-1.5199 (0.1083)	0.1657 (0.0254)	0.0025 (0.0001)	0.0382 (0.0001)	58076.0270 (0.0150)	SSS
2017ilf	-1.7687 (0.2039)	0.0508 (0.0246)	0.0042 (0.0002)	0.0297 (0.0000)	58087.4730 (0.3150)	SSS
2017iln	0.8146 (0.2819)	0.0440 (0.0398)	0.0011 (0.0001)	0.0752 (0.0001)	58084.4650 (0.4630)	SSS
2017iws	0.3199 (0.1374)	0.0410 (0.0172)	0.0006 (0.0000)	0.0945 (0.0000)	58104.8120 (0.1960)	SSS
2017iye	-0.8221 (0.0996)	-0.0101 (0.0228)	0.0025 (0.0001)	0.0464 (0.0001)	58111.3120 (0.1860)	SSS
2017jgi	-0.9272 (0.4221)	0.0101 (0.0295)	0.0003 (0.0000)	0.1300 (0.0100)	58117.6880 (0.5200)	SSS
2017lb	0.2918 (0.2473)	-0.0017 (0.0272)	0.0018 (0.0001)	0.0528 (0.0001)	57773.4450 (0.8000)	SSS
2017lc	-1.5508 (0.2434)	-0.0764 (0.0633)	0.0013 (0.0001)	0.0600 (0.0100)	57772.2270 (1.2750)	SSS
2017ux	0.5181 (0.2944)	-0.0299 (0.0312)	0.0012 (0.0001)	0.0700 (0.0100)	57787.9650 (0.8200)	SSS

Table 4.1 (cont'd)

SN	x1	c	x0	z_{helio}	Peak MJD	Source
2017yk	-0.8577 (0.1055)	0.2795 (0.0238)	0.0011 (0.0000)	0.0464 (0.0001)	57789.5780 (0.2980)	SSS
2017yn	0.4712 (0.4371)	-0.0269 (0.0411)	0.0015 (0.0001)	0.0700 (0.0100)	57783.1020 (1.1610)	SSS
2018aay	-0.4313 (0.1197)	0.2159 (0.0201)	0.0030 (0.0001)	0.0309 (0.0002)	58186.0940 (0.2380)	SSS
2018abz	-0.8048 (0.1024)	0.1371 (0.0215)	0.0008 (0.0000)	0.0549 (0.0001)	58184.3750 (0.0250)	SSS
2018agk	-0.0562 (0.1341)	0.1558 (0.0202)	0.0035 (0.0001)	0.0261 (0.0001)	58204.1760 (0.0970)	SSS
2018aoz	-1.3470 (0.0812)	-0.0132 (0.0254)	0.1953 (0.0091)	0.0060 (0.0001)	58222.3200 (0.1500)	SSS
2018bfr	-0.2132 (0.1925)	0.1934 (0.0212)	0.0011 (0.0000)	0.0717 (0.0001)	58248.0310 (0.3860)	SSS
2018bq	3.4600 (0.7173)	0.1542 (0.0309)	0.0080 (0.0003)	0.0256 (0.0001)	58131.1130 (1.0400)	SSS
2018bs	0.2529 (0.1814)	-0.0332 (0.0266)	0.0013 (0.0000)	0.0670 (0.0001)	58134.3200 (0.2240)	SSS
2018bsn	1.2094 (0.1943)	0.0790 (0.0176)	0.0016 (0.0000)	0.0586 (0.0000)	58260.3120 (0.2850)	SSS
2018cjy	1.9547 (0.2274)	0.0718 (0.0238)	0.0014 (0.0001)	0.0641 (0.0001)	58292.6640 (0.2570)	SSS
2018cqw	-0.0269 (0.1298)	0.0523 (0.0292)	0.0501 (0.0038)	0.0098 (0.0002)	58300.5270 (0.0780)	SSS
2018feb	-0.2763 (0.0740)	0.0631 (0.0190)	0.0197 (0.0007)	0.0148 (0.0001)	58363.0510 (0.1440)	SSS
2018gv	0.5073 (0.0690)	0.0064 (0.0172)	0.1758 (0.0057)	0.0054 (0.0001)	58150.6760 (0.0650)	SSS
2018hfp	-0.2715 (0.0705)	0.1397 (0.0203)	0.0065 (0.0003)	0.0291 (0.0001)	58407.1880 (0.0820)	SSS
2018hfr	0.9155 (0.2069)	0.1330 (0.0190)	0.0111 (0.0002)	0.0226 (0.0001)	58407.2230 (0.4460)	SSS
2018hhn	0.2741 (0.1119)	0.0800 (0.0195)	0.0065 (0.0003)	0.0288 (0.0005)	58416.9100 (0.0690)	SSS
2018ilu	0.7887 (0.0937)	-0.0336 (0.0221)	0.0192 (0.0007)	0.0179 (0.0003)	58450.3010 (0.0610)	SSS
2018jeo	0.1855 (0.1003)	0.0255 (0.0320)	0.0158 (0.0016)	0.0184 (0.0001)	58454.6050 (0.2270)	SSS
2018kav	-0.0416 (0.0686)	0.0068 (0.0193)	0.0051 (0.0001)	0.0325 (0.0050)	58481.3440 (0.0620)	SSS
2018oh	0.6819 (0.0657)	-0.0802 (0.0194)	0.0484 (0.0014)	0.0109 (0.0000)	58163.0230 (0.0880)	SSS
2018ph	-2.1301 (0.1198)	0.0501 (0.0190)	0.0056 (0.0001)	0.0304 (0.0002)	58161.8750 (0.1960)	SSS
2018tt	0.5160 (0.1395)	0.0310 (0.0198)	0.0013 (0.0000)	0.0600 (0.0001)	58170.2700 (0.2770)	SSS
2019bka	-0.8449 (0.2812)	0.0071 (0.0571)	0.0116 (0.0009)	0.0240 (0.0100)	58555.5350 (0.2980)	SSS
2019cpe	-0.3200 (0.0804)	0.0349 (0.0171)	0.0022 (0.0001)	0.0488 (0.0001)	58583.9380 (0.0980)	SSS
2019dfa	-0.0492 (0.0794)	0.1135 (0.0212)	0.0055 (0.0001)	0.0264 (0.0000)	58597.3010 (0.0830)	SSS
2019dwq	-0.0074 (0.0801)	-0.0185 (0.0182)	0.0079 (0.0002)	0.0277 (0.0002)	58610.0740 (0.0810)	SSS
2019fzm	-0.1477 (0.1079)	0.1042 (0.0207)	0.0080 (0.0003)	0.0232 (0.0000)	58640.9220 (0.3330)	SSS
2019gbx	-1.6701 (0.1198)	-0.0339 (0.0294)	0.0325 (0.0012)	0.0131 (0.0001)	58647.4570 (0.1230)	SSS
2019gcw	-2.3419 (0.1765)	0.0860 (0.0271)	0.0029 (0.0001)	0.0350 (0.0001)	58645.7300 (0.2120)	SSS
2019gf	0.9991 (0.1665)	-0.0375 (0.0205)	0.0016 (0.0001)	0.0668 (0.0001)	58498.8200 (0.2140)	SSS
2019jf	-1.8742 (0.1266)	0.0094 (0.0264)	0.0024 (0.0001)	0.0414 (0.0001)	58501.6170 (0.1080)	SSS
2019lqv	-1.3670 (0.1029)	0.2832 (0.0195)	0.0022 (0.0001)	0.0336 (0.0002)	58693.1950 (0.0940)	SSS
2019lrc	-2.1916 (0.1592)	0.1600 (0.0079)	0.0022 (0.0001)	0.0343 (0.0001)	58692.6410 (0.2550)	SSS
2019nhy	-0.7613 (0.1412)	0.1149 (0.0243)	0.0013 (0.0001)	0.0550 (0.0001)	58717.2190 (0.2830)	SSS
2019ons	1.5520 (0.1345)	0.1576 (0.0205)	0.0034 (0.0001)	0.0370 (0.0001)	58735.1800 (0.0980)	SSS
2019teo	-0.0642 (0.1011)	-0.0260 (0.0208)	0.0040 (0.0001)	0.0372 (0.0000)	58793.0860 (0.0730)	SSS
2019vju	-0.4708 (0.0601)	0.5300 (0.0187)	0.0047 (0.0001)	0.0129 (0.0000)	58820.1370 (0.0820)	SSS
2019vnj	0.7065 (0.1204)	0.0559 (0.0197)	0.0076 (0.0002)	0.0247 (0.0000)	58819.4880 (0.1480)	SSS
2020dhj	3.2744 (0.9188)	-0.0019 (0.0356)	0.0030 (0.0001)	0.0442 (0.0000)	58921.1760 (0.7010)	SSS
iptf13ebh	-2.7275 (0.0889)	0.1092 (0.0185)	0.0213 (0.0004)	0.0132 (0.0001)	56623.0040 (0.0790)	CSPDR3
ptf10bjs	0.9184 (0.2318)	0.3592 (0.1809)	0.0048 (0.0011)	0.0300 (0.0000)	55261.7700 (0.1810)	CfA4-p2

Note. — SALT3 fit parameters generated for the SNe Ia in the CSPDR3, Cfa3-Kepler, CfA4, and SSS surveys. The fits were performed on the $BVgr$ filters for the CSPDR3 and SSS data and the BVr filters for the Cfa3-Kepler and CfA4 data.

4.3 i-band Light-Curve Measurements

4.3.1 The $\Delta m_1 - \Delta m_2$ Parameter

Throughout this chapter, we will refer to the i-band secondary maximum as m_2, and the local i-band minimum occurring between the primary i-band peak and m_2 as m_1. We define the parameter $\Delta m_1 - \Delta m_2$ as the difference between the observed i-band magnitudes and the SALT3 model magnitudes at two specific epochs: the local minimum (m_1) and the secondary maximum (m_2) (see Figure 4.3). Notice the significant difference between the m_1 and m_2 magnitudes for the two example SNe.

The i-band light curves of SNe Ia exhibit significant dispersion compared to the more uniform B- and V-band light curves for SNe with similar decline rates (Δm_{15}) (Folatelli et al. 2010). Figure 4.4 shows seven SNe Ia with nearly identical Δm_{15} B-band values (1.05-1.08 mag). While the B-band light curves possess consistent behavior when aligned by their maximum brightness, the i-band light curves show significant variability in the timing and strength of the secondary maxima and local minima.

The timing and strength of m_1 and m_2 are influenced by x_1 and redshift z. In Figure 4.5, we show the variations in i-band light-curve shape, m_1 and m_2 when altering x_1 and redshift for nominal SALT3 models with $c = 0$, $z = 0.023$ (for varying x_1) and $x_1 = 0$ (for varying redshift).

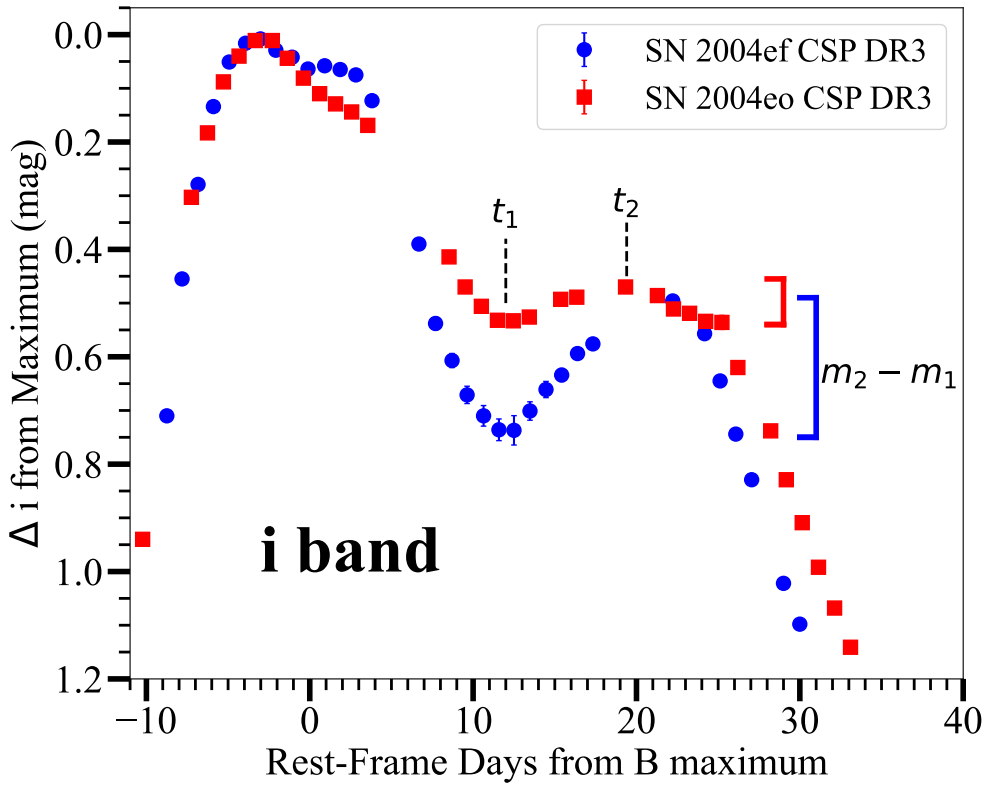

Figure 4.3 Illustration of the i-band light curves for SN 2004ef (blue circles) and SN 2004eo (red squares) from CSP DR3. The points t_1 and t_2 correspond to the i-band minimum and secondary maximum, respectively, with m_1 and m_2 representing the magnitudes at these epochs. The difference in magnitudes, $m_2 - m_1$, is also marked, highlighting the diversity in i-band light-curve features between these SNe.

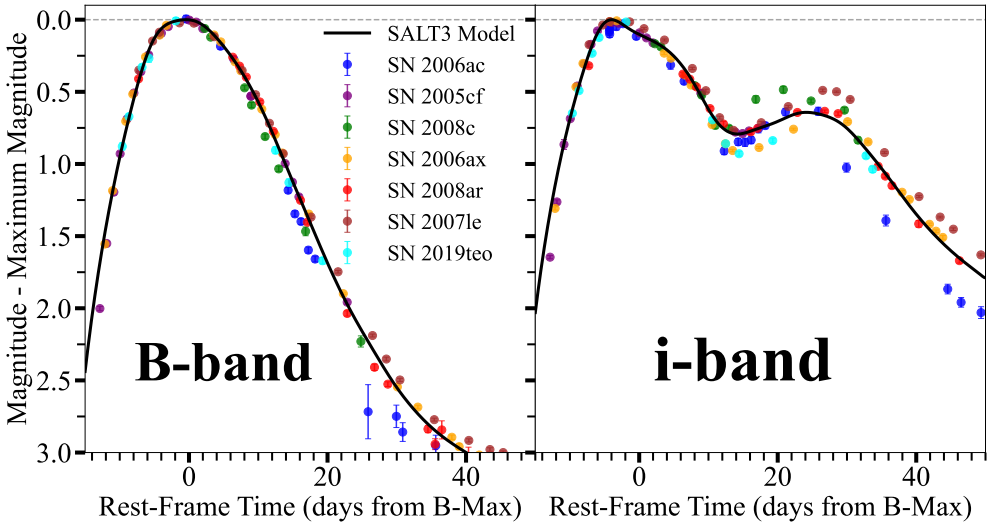

Figure 4.4 B- and i-band plots with SNe of similar Δm_{15} (B). The B-band data (left panel) show minimal diversity, whereas the i-band (right panel) displays significantly greater variation.

4.3.2 SALT3 model fits

We fit our data using the most recent version of SALT, the SALT3-K21[17] model (Kenworthy et al. 2021b; Taylor et al. 2023) as implemented in SNANA, a public software package for SN analysis[18] (Kessler et al. 2009). As a means to study the generation of the i band from the SALT3 model, we use all the filters except i to generate the SALT3 fits. For surveys utilizing $BVri$ filters (CfA3, CfA4), the SN light curves are fit using only the BVr bands, with the i-band model derived from these fits. Likewise, for surveys with $BVgri$ filters (CSPDR3, SSS), the i-band model is generated based on fits to the $BVgr$ bands.

[17] https://saltshaker.readthedocs.io/en/latest/
[18] https://github.com/RickKessler/SNANA

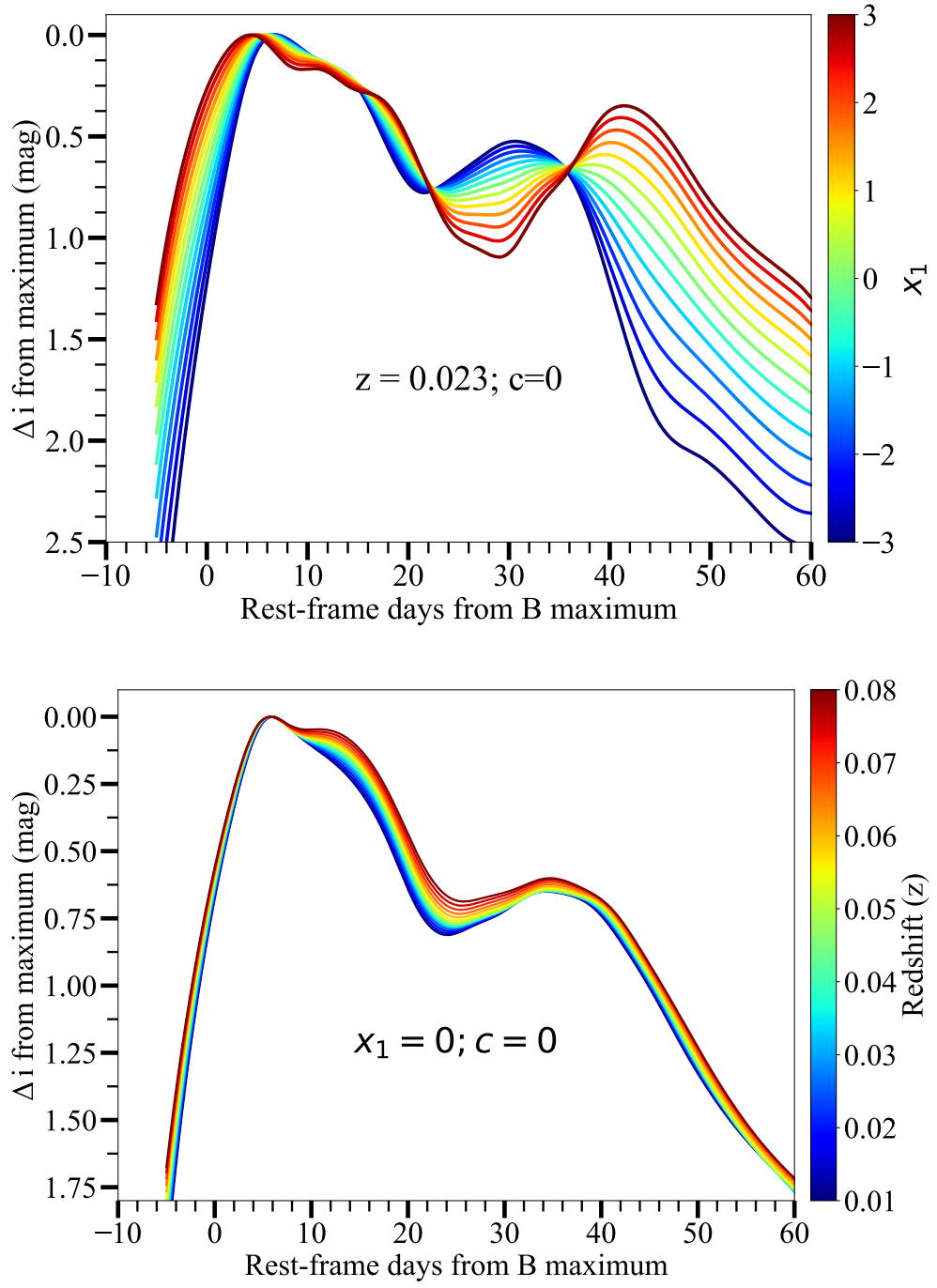

Figure 4.5 Impact of x_1 variations while keeping a fixed redshift and c (top panel), and redshift variations while keeping a fixed x_1 and c (lower panel) on the i-band light curves. In both cases, there is a significant i-band diversity, especially around the strength of the i-band secondary maximum and the i-band minimum.

4.3.3 Data minus Model residuals

In order to compare the i-band data to the generated SALT3 i-band model, we first select a light-curve phase where the diversity of i-band light curves is not as strong as in the minimum (m_1) or secondary maximum (m_2), and where the residuals (light-curve data minus model) are mostly consistent within each SN. After analyzing the data across different phases, we chose the window between -3 to $+4$ days from maximum light in the B band since this window presented the least residual scatter while having at least 100 SNe with at least two data points for the subsequent analysis.

Then, we calculate the offset that minimizes the data minus model residuals in this window (see Figure 4.6). A minimum of two data points is required for a more robust offset calculation. We apply this shift to the entire i-band light curve. These "optimized" magnitudes are now compared to the generated i-band model. We refer to the resulting residuals as Δm_x, where x represents the comparison phase of interest.

We then calculate the weighted mean data minus model residuals around two key i-band light-curve features: the i-band minimum between maxima (m_1) and the i-band secondary maximum (m_2). We choose a period of -5 to $+5$ days around m_1 and m_2 to calculate the weighted mean residual for each SN. This range is narrow enough to focus on these specific light-curve features while ensuring enough data coverage around them to calculate the weighted mean, while avoiding points farther from these epochs that could introduce additional noise. Finally, we calculate the difference between each SN's data minus model weighted mean residuals at m_1 and m_2 ($\Delta m_1 - \Delta m_2$).

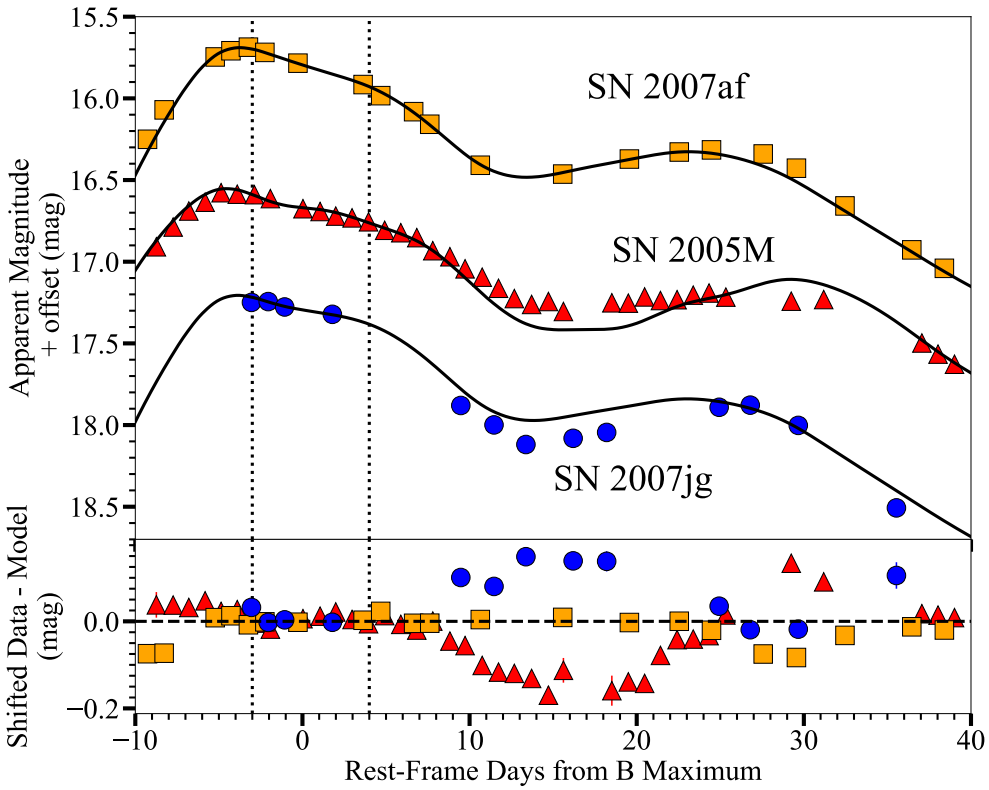

Figure 4.6 Comparison of observed i-band light curves (symbols) and SALT3 model fits (solid lines) for three SNe: SN 2007af (orange squares), SN 2005M (red triangles), and SN 2007jg (blue circles). The top panel shows the apparent magnitudes with an applied offset for clarity, while the bottom panel displays residuals (data minus model), highlighting deviations between observations and model predictions. The observed light curves have been shifted to align with the SALT3 model within the region defined by the dashed lines (-3 to +4 days from peak B-band light).

4.3.4 Sample cuts

To ensure our results are reliable, we perform a series of sample cuts to select SNe Ia with well-sampled light curves, accurate SALT3 fits, and spectral measurements for our analysis. These cuts are implemented to eliminate outliers and poorly observed events, assuring our sample is representative and suitable for studying i-band light curve diversity.

The criteria are the following:

1. Initial successful SALT3 fit with SNANA (uncertainty on $x_1 < 3$).

2. The SN is a normal or SN 1991T-like SNe Ia, subtypes on which the SALT3 model is successfully trained (Kenworthy et al. 2021b).

3. $B - V$ SN color measured at the time of B-band maximum light $(B - V)_{\max} <$ 0.3 mag.

4. $-2.1 < x_1 < 1.5$ to remove fast- and slow-declining SNe. Foley et al. (2011) found that over the $1.0 - 1.5$ $\Delta m_{15}(B)$ mag range, spectral properties such as Si II and Ca velocity and equivalent width (EW) are uncorrelated with light-curve shape. This range approximately corresponds to $-2.6 < x_1 < 0.5$ (Siebert et al. 2019). With the aim be more conservative with the fast-declining SNe (higher Δm_{15}) and explore a larger parameter space with slow-declining SNe such as SN 1991T-like transients (which are modeled accurately by SALT3), we adjusted the decline rate range to $0.9 < \Delta m_{15}(B) < 1.45$ mag, which approximately corresponds to the final x_1 range used in this work.

Table 4.2. Sample cuts

Criterion	No. SNe NP	Cum. SNe NP	SNe Rem.
Initial Sample	···	···	455
Valid SALT3 fit	31	31	424
Valid $(B-V)_{\max} < 0.3$ mag	253	288	171
Normal/91T-like	18	306	153
$-2.1 < x_1 < 1.5$	12	318	141
Number of datapoints in window ≥ 2	37	355	104
m_1 and m_2 measurements	50	405	54
$\mathrm{pEW}_0(\mathrm{Ca\,II})$ or $v^0_{\mathrm{Si\,II}}$ measurements	14	419	40

5. At least two data points in the -3 to $+4$ days from the B-maximum light window for a robust offset calculation between the i-band light curve data and the generated SALT3 model (see section 4.3.3).

6. A Ca pseudo equivalent width (pEW) or Si velocity measurement near peak brightness (see Section 4.4).

The number of SNe Ia removed by each cut and the total number of SNe Ia remaining after each step in the selection process is presented in Table 4.2.

4.4 Spectral measurements

To measure velocities in our sample, we first generate a smoothed spectrum using an inverse-variance Gaussian filter (Blondin et al. 2006) and a kernel with width automatically set by the spectrum signal-to-noise ratio. We then take the wavelength of maximum absorption (i.e., the wavelength of the local minimal flux value) in the smoothed spectrum to measure the velocity. We select this method as opposed to fitting the entire line profile because it does not assume a particular functional form.

We then visually inspect every spectral measurement to ensure that the minimum is not being fit to noise, and resmooth if needed (see Fig. 4.7).

Although smoothing cannot shift the minimum if the spectral feature is symmetric about the minimum, this is not always the case for Si II λ 6355. Similar to Blondin et al. (2011), we rerun our velocity measurements while varying the kernel width through 1000 iterations to estimate the systematic uncertainty introduced by smoothing. In almost all cases, the width of the distribution of the consequent velocities (which we take as an estimate of the uncertainty) is lower than the 200 km/s uncertainty floor set by the random motion of the SNe in their host galaxies.

To measure pseudo-equivalent widths, we follow a generally similar procedure. Again, we first generate a smoothed spectrum to determine the pseudo-continuum above our features of interest. We find local maxima in the continuum region around our spectral lines (one maximum on each side) and take the line through these points as the continuum. We then visually inspect each fit, ensuring that (1) the maxima found provide a reasonable estimate of the pseudo-continuum and (2) the smoothing is not artificially lowering the maxima, which can occur if the continuum regions are narrow relative to the width of the kernel used. We manually refit in all cases where either criterion is not met. When comparing automatic and manual measurements, the samples are consistent. To measure the pseudo-equivalent width, we then calculate the area between the pseudo-continuum and the unsmoothed spectrum. Similarly to the velocities, we estimate the systematic uncertainties introduced by smoothing by varying the smoothing kernel width through 1000 iterations (which will shift the continuum location) and measuring the resulting pseudo-equivalent widths.

In order to convert Si II λ 6355 velocity and Ca H&K pEW to values at peak light, we use Equations (5) and (9) in Foley et al. (2011), which we reproduce here:

$$v^0_{\mathrm{Si\,II}} = \frac{v_{\mathrm{Si\,II}} + 0.285 t_{\mathrm{Si\,II}}}{1 - 0.0322 t_{\mathrm{Si\,II}}}, \tag{4.1}$$

$$\mathrm{pEW}_0(\mathrm{Ca\,II}) = \frac{\mathrm{pEW(Ca\,II)} + 0.708 t_{\mathrm{pEW(Ca\,II)}}}{1 - 0.0210 t_{\mathrm{pEW(Ca\,II)}}}, \tag{4.2}$$

where

- $v^0_{\mathrm{Si\,II}}$ is the Si II λ 6355 velocity at peak,
- $v_{\mathrm{Si\,II}}$ is the Si II λ 6355 velocity measured at phase, $t_{\mathrm{Si\,II}}$,
- $t_{\mathrm{Si\,II}}$ is only within $-6 \leq t_{\mathrm{Si\,II}} \leq +10$ days from peak,
- $\mathrm{pEW}_0(\mathrm{Ca\,II})$ is the Ca H&K pseudo-equivalent width at peak,
- $\mathrm{pEW(Ca\,II)}$ is the Ca H&K pseudo-equivalent width measured at phase $t_{\mathrm{pEW(Ca\,II)}}$,
- $t_{\mathrm{pEW(Ca\,II)}}$ is only within $-7 \leq t_{\mathrm{pEW(Ca\,II)}} \leq +9$ days from peak,
- both $v^0_{\mathrm{Si\,II}}$ and $\mathrm{pEW}_0(\mathrm{Ca\,II})$ are calculated for the measurement closest to $t_{\mathrm{Si\,II}} = 0$ and $t_{\mathrm{pEW(Ca\,II)}} = 0$ days, respectively.

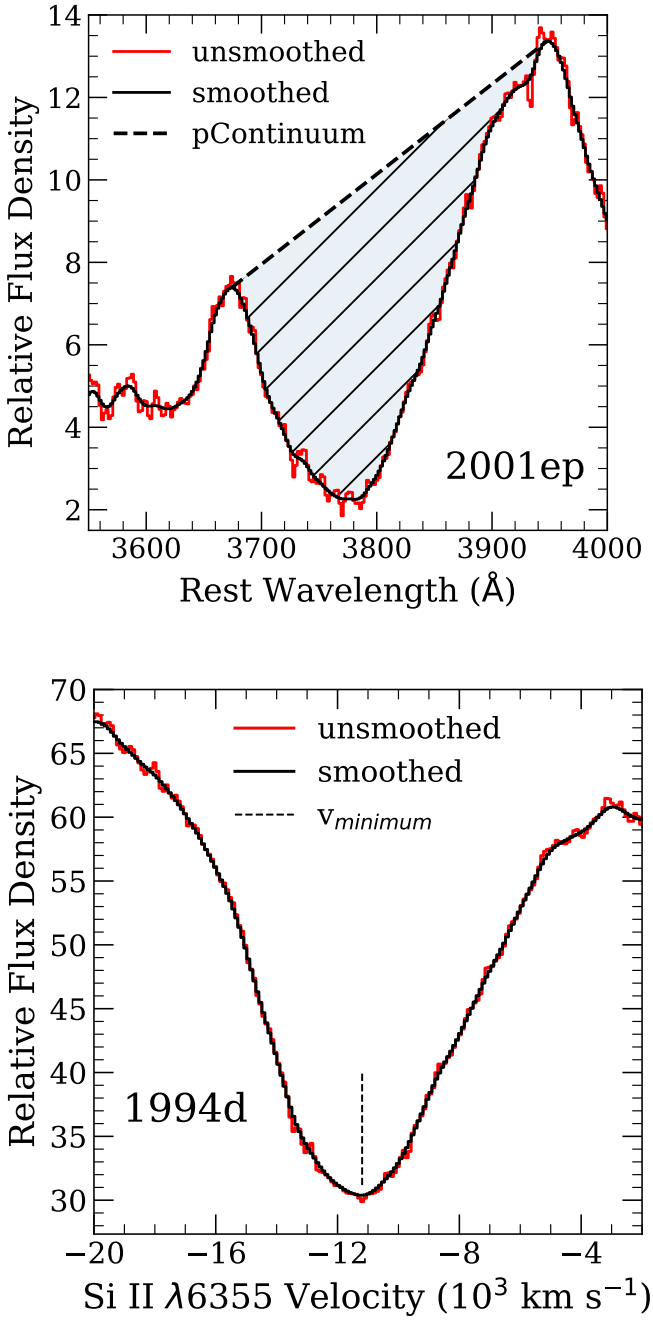

Figure 4.7 Top panel: Demonstration of a pseudo-equivalent width (pEW) measurement. The unsmoothed spectrum (red) and smoothed spectrum (black) are shown, along with the pseudo-continuum (dashed line). The shaded region represents the area used to calculate the pEW. Bottom panel: Illustration of a velocity measurement for the Si II 6355 Å line. The unsmoothed spectrum (red) and smoothed spectrum (black) are plotted, with the dashed line indicating the wavelength of maximum absorption (local flux minimum) used to determine the velocity. These methods involve smoothing and systematic uncertainty estimation to ensure robust measurements.

4.5 Relationship between the i-band secondary maximum, minimum, and spectral measurements

We compare the weighted mean data minus model residuals $\Delta m_1 - \Delta m_2$ (see Section 4.3.3) with the Ca pEW$_0$ and Si v_0 measurements for each SN (section 4.4). The final sample of SNe Ia with Ca pEW$_0$, Si v_0, Δm_1, Δm_2 and $\Delta m_1 - \Delta m_2$ measurements is presented in Table 4.3.

We evaluate the relationship between the parameter $\Delta m_1 - \Delta m_2$ and the Ca pEW$_0$ and Si v_0 spectral measurements in Figure 4.8. The top panel shows a strong, positive correlation between the i-band parameter $\Delta m_1 - \Delta m_2$ and the pseudo-equivalent width of Ca II H&K at maximum light (Ca pEW$_0$), where larger values of Ca pEW$_0$ correspond to larger $\Delta m_1 - \Delta m_2$ values. This indicates that stronger calcium absorption is associated with a more significant difference between the i-band data minus SALT3 model residuals at the minimum and secondary maximum. The bottom panel also displays a strong, positive correlation between $\Delta m_1 - \Delta m_2$ and the velocity of Si II at maximum light (Si v_0). SNe Ia with higher Si v_0 show larger $\Delta m_1 - \Delta m_2$. The color coding of both panels represents the SALT3 light-curve stretch parameter x_1, with a range of values from low (blue) to high (red).

In these relationships, there is no clear trend of x_1 with either Ca pEW$_0$ or Si v_0. For the Ca pEW$_0$ relationship, SNe with both low and high x_1 values show a spread in $\Delta m_1 - \Delta m_2$ and Ca pEW$_0$, with no clear trend. In contrast, for the Si v_0 relationship, SNe with extreme Si $v_0$values show different behaviors: low Si v_0 and high

Table 4.3. Final sample

SN	Source	$\mathrm{pEW}_0(\mathrm{Ca\,II})$	$v^0_{\mathrm{Si\,II}}$	Δm_1	Δm_2	$\Delta m_1 - \Delta m_2$
2004ef	CSPDR3	158.020 (7.000)	12.339 (0.240)	0.011 (0.032)	-0.009 (0.032)	0.021 (0.046)
2004eo	CSPDR3	109.368 (7.000)	10.934 (0.240)	-0.191 (0.032)	-0.081 (0.032)	-0.110 (0.045)
2004ey	CSPDR3	–	11.074 (0.240)	0.050 (0.032)	0.017 (0.032)	0.033 (0.046)
2004gs	CSPDR3	83.487 (7.000)	11.528 (0.240)	-0.094 (0.033)	-0.056 (0.033)	-0.038 (0.046)
2005ag	CSPDR3	–	11.431 (0.240)	0.008 (0.036)	0.003 (0.037)	0.005 (0.051)
2005am	CSPDR3	140.694 (7.000)	12.568 (0.240)	-0.010 (0.033)	-0.041 (0.032)	0.031 (0.046)
2005el	CfA3-Kepler	98.476 (7.000)	11.036 (0.240)	0.172 (0.035)	0.057 (0.033)	0.116 (0.048)
2005eq	CSPDR3	78.369 (7.000)	9.637 (0.240)	-0.013 (0.033)	0.111 (0.034)	-0.125 (0.047)
2005hc	CSPDR3	134.735 (7.000)	11.449 (0.240)	0.013 (0.035)	0.030 (0.034)	-0.017 (0.049)
2005hj	CSPDR3	–	10.967 (0.240)	0.079 (0.040)	0.082 (0.037)	-0.004 (0.055)
2005kc	CSPDR3	–	10.352 (0.240)	-0.026 (0.033)	-0.025 (0.033)	-0.001 (0.046)
2005ki	CSPDR3	105.769 (7.000)	11.079 (0.240)	0.127 (0.033)	0.017 (0.033)	0.110 (0.046)
2005m	CSPDR3	–	8.094 (0.231)	-0.124 (0.033)	0.061 (0.033)	-0.184 (0.046)
2005na	CSPDR3	98.708 (7.000)	10.673 (0.240)	0.046 (0.033)	-0.024 (0.032)	0.070 (0.046)
2006ac	CfA3-Kepler	123.399 (7.000)	13.888 (0.240)	0.057 (0.034)	-0.028 (0.035)	0.085 (0.049)
2006ax	CfA3-Kepler	118.827 (7.000)	10.571 (0.240)	0.085 (0.034)	-0.001 (0.034)	0.086 (0.048)
2006az	CfA3-Kepler	77.429 (7.000)	10.673 (0.240)	-0.100 (0.034)	-0.065 (0.034)	-0.035 (0.048)
2006bh	CSPDR3	–	11.451 (0.240)	0.082 (0.032)	0.072 (0.032)	0.010 (0.046)
2006bq	CfA3-Kepler	171.675 (7.000)	15.353 (0.240)	0.203 (0.034)	0.032 (0.035)	0.172 (0.049)
2006d	CSPDR3	89.580 (7.000)	10.619 (0.240)	0.111 (0.032)	0.108 (0.032)	0.003 (0.046)
2006kf	CSPDR3	106.568 (7.000)	11.410 (0.240)	-0.011 (0.033)	0.089 (0.033)	-0.100 (0.047)
2006le	CfA3-Kepler	131.986 (7.000)	11.704 (0.240)	0.055 (0.035)	0.027 (0.034)	0.028 (0.049)
2006lf	CfA3-Kepler	90.795 (7.000)	11.333 (0.240)	0.109 (0.035)	0.042 (0.035)	0.067 (0.049)
2006n	CfA3-Kepler	103.995 (7.000)	11.448 (0.240)	0.063 (0.034)	0.090 (0.033)	-0.027 (0.047)
2006s	CfA3-Kepler	125.488 (7.000)	10.794 (0.240)	0.014 (0.038)	0.051 (0.034)	-0.036 (0.051)
2007af	CSPDR3	121.437 (7.000)	11.077 (0.240)	0.007 (0.032)	-0.026 (0.032)	0.032 (0.046)
2007as	CSPDR3	186.984 (7.000)	13.265 (0.240)	0.113 (0.032)	-0.017 (0.032)	0.129 (0.046)
2007ca	CSPDR3	118.954 (7.000)	10.903 (0.240)	0.119 (0.032)	0.099 (0.033)	0.020 (0.046)
2007co	CfA3-Kepler	144.773 (7.000)	11.759 (0.240)	0.016 (0.034)	-0.114 (0.034)	0.130 (0.048)
2007f	CfA3-Kepler	98.051 (7.000)	10.944 (0.240)	0.067 (0.034)	0.026 (0.033)	0.041 (0.047)
2007jg	CSPDR3	183.297 (7.000)	12.781 (0.240)	0.116 (0.033)	0.036 (0.034)	0.080 (0.047)
2007kk	CFA4-p1	–	12.071 (0.222)	-0.135 (0.049)	-0.133 (0.038)	-0.002 (0.062)
2007le	CSPDR3	162.594 (7.000)	12.655 (0.240)	-0.010 (0.032)	-0.094 (0.032)	0.085 (0.046)
2007nq	CSPDR3	104.367 (7.000)	12.018 (0.240)	-0.007 (0.033)	0.006 (0.033)	-0.013 (0.047)
2007qe	CfA3-Kepler	154.913 (7.000)	12.386 (0.240)	0.041 (0.035)	-0.078 (0.034)	0.119 (0.049)
2008bc	CSPDR3	138.779 (7.000)	11.467 (0.240)	0.073 (0.033)	0.050 (0.032)	0.023 (0.046)
2008bf	CSPDR3	129.200 (7.000)	11.546 (0.240)	0.094 (0.033)	0.071 (0.034)	0.023 (0.047)
2008c	CSPDR3	119.989 (7.000)	10.761 (0.240)	-0.052 (0.034)	-0.111 (0.034)	0.060 (0.048)
2008hv	CSPDR3	–	10.912 (0.240)	0.112 (0.032)	0.045 (0.032)	0.067 (0.046)
2018bsn	SSS	136.832 (7.000)	12.941 (0.240)	0.021 (0.036)	-0.063 (0.039)	0.084 (0.054)

Table 4.4. Summary of correlations between $\Delta m_1 - \Delta m_2$ and Ca pEW$_0$ and Si v_0.

$\Delta m_1 - \Delta m_2$	MCMC σ	Pearson r	Pearson p	Slope	Intercept	Slope Z-score
vs. Ca pEW$_0$	3.3	0.55	1.05×10^{-3}	0.001 (0.0002)	−0.13 (0.049)	3.6
vs. Si v_0	4.6	0.64	7.70×10^{-6}	0.041 (0.008)	−0.44 (0.09)	5.1

x_1 correspond to negative $\Delta m_1 - \Delta m_2$ residuals, while high Si $v_0$and low x_1 correspond to positive $\Delta m_1 - \Delta m_2$ residuals. However, SNe with varying x_1 values are distributed across the Si v_0 and $\Delta m_1 - \Delta m_2$ axes, indicating no strong correlation.

We assess the significance of the correlations between each $\Delta m_1 - \Delta m_2$ and Ca pEW$_0$ and Si $v_0$using a Markov Chain Monte Carlo (MCMC; Speagle 2019) method, employing 300 walkers, 50,000 steps, and a burn-in of 2,000 steps. We find significant 3.29 and 4.62σ trends with Ca pEW$_0$ and Si v_0, respectively. Both relationships indicate a significant Pearson p-value and slope (see Table 4.4). Additionally, we also evaluated the possible correlation of the $\Delta m_1 - \Delta m_2$ residuals with redshift z but did not find a strong correlation (Pearson $r = -0.12$, Pearson $p = 0.47$).

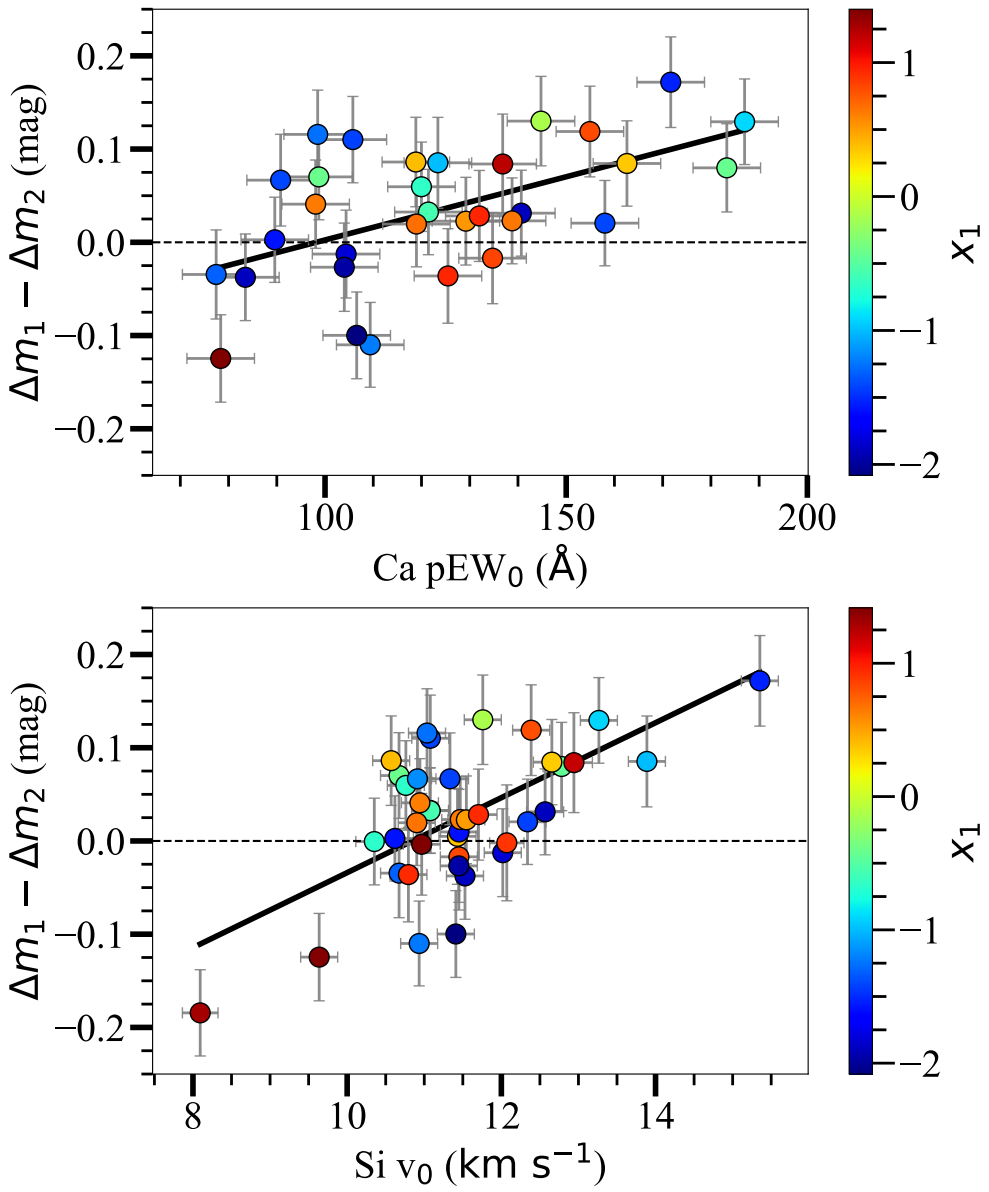

Figure 4.8 Correlation between i-band light-curve parameter $\Delta m_1 - \Delta m_2$ and spectroscopic features, color-coded by x_1. The top panel shows the relationship with the pseudo-equivalent width of Ca II (Ca pEW$_0$), while the bottom panel shows the relationship with the Si II velocity (Si v_0). Both relationships are significant (over 3σ) and could provide insights into a better understanding of the i-band diversity of SNe Ia.

4.6 Discussion

We observe a clear trend between the $\Delta m_1 - \Delta m_2$ residuals and the Ca II pEW_0 or Si II v_0 values. At the same time, these residuals vary widely in x_1 and do not show a strong trend. We also do not find a significant correlation of the $\Delta m_1 - \Delta m_2$ residuals with redshift z, which could potentially indicate the correlations shown in Figure 4.8 are not due to observational biases or evolutionary effects.

To further investigate the relationship between spectroscopic features and the $\Delta m_1 - \Delta m_2$ parameter, we explored the effect of varying the strength of the O I and Ca NIR triplet lines, which dominate the i-band wavelength region. By adjusting the strength of these lines, we investigate their impact on the synthetic photometry and the SALT3-modeled light curves. This method can provide insights into how spectral variations could influence photometric behavior.

For each daily phase of a generic SALT3 SED model with $x_1 = 0$, we identify the continuum points, calculate the continuum, normalize the spectrum relative to the continuum, and measure the depth, equivalent width, and velocity for the O I and Ca NIR triplet lines. Using these measurements, we create a spectrum with the calculated absorption features and calculate the synthetic photometry to evaluate the impact of these variations on $\Delta m_1 - \Delta m_2$.

The impact of these variations is shown in Figure 4.9. The top panels show that for the O I line, modeled variations in the velocity and pEW have a minimal effect on the light curves. In contrast, the Ca II NIR triplet shows a much stronger effect, with noticeable differences in the strength of the i-band secondary maximum and the

i-band minimum, especially at larger perturbations. The linear trend of the $\Delta m_1 - \Delta m_2$ residuals with the modeled Ca II NIR pEW values is consistent with the relationship in observational data of $\Delta m_1 - \Delta m_2$ and Ca II pEW_0 shown in Figure 4.8, supporting the connection between Ca II features and i-band light curve morphology.

This result is also consistent with the findings of Pessi et al. (2022): even though their sample is small and they use a different i-band light curve parameter (the change in the concavity in the light curve between the primary peak and the minimum), they find a strong correlation with their metric and the Ca II NIR pEW.

We also want to evaluate if SNe Ia with different $\Delta m_1 - \Delta m_2$ residuals show differences in their observed spectra. We use the open-source, relational database `kaepora` (Siebert et al. 2019, 2020) to produce composite SN Ia spectra. This tool offers an extensive collection of homogenized SN Ia spectra in a large wavelength range and their metadata. The composite spectra derived from `kaepora` offer greater insights into potential spectral feature trends than individual measurements.

In Figure 4.10, we present composite spectra of two subsamples with similar phase and $\Delta m_{15}(B)$ but differing in $\Delta m_1 - \Delta m_2$. We split the $\Delta m_1 - \Delta m_2$ samples at 0.04. The low $\Delta m_1 - \Delta m_2$ residuals composite spectrum consists of 48 spectra of 10 different SNe Ia, while the high $\Delta m_1 - \Delta m_2$ residuals composite spectrum consists of 31 spectra of 10 different SNe Ia, using phase bins between 0 and 4 days after B-band peak.

The composite spectra show notable differences between the low and high $\Delta m_1 - \Delta m_2$ residuals for the highlighted spectral features. For the Ca II H&K region, the high residuals (red) exhibit a slightly stronger absorption, as shown by the flux dip

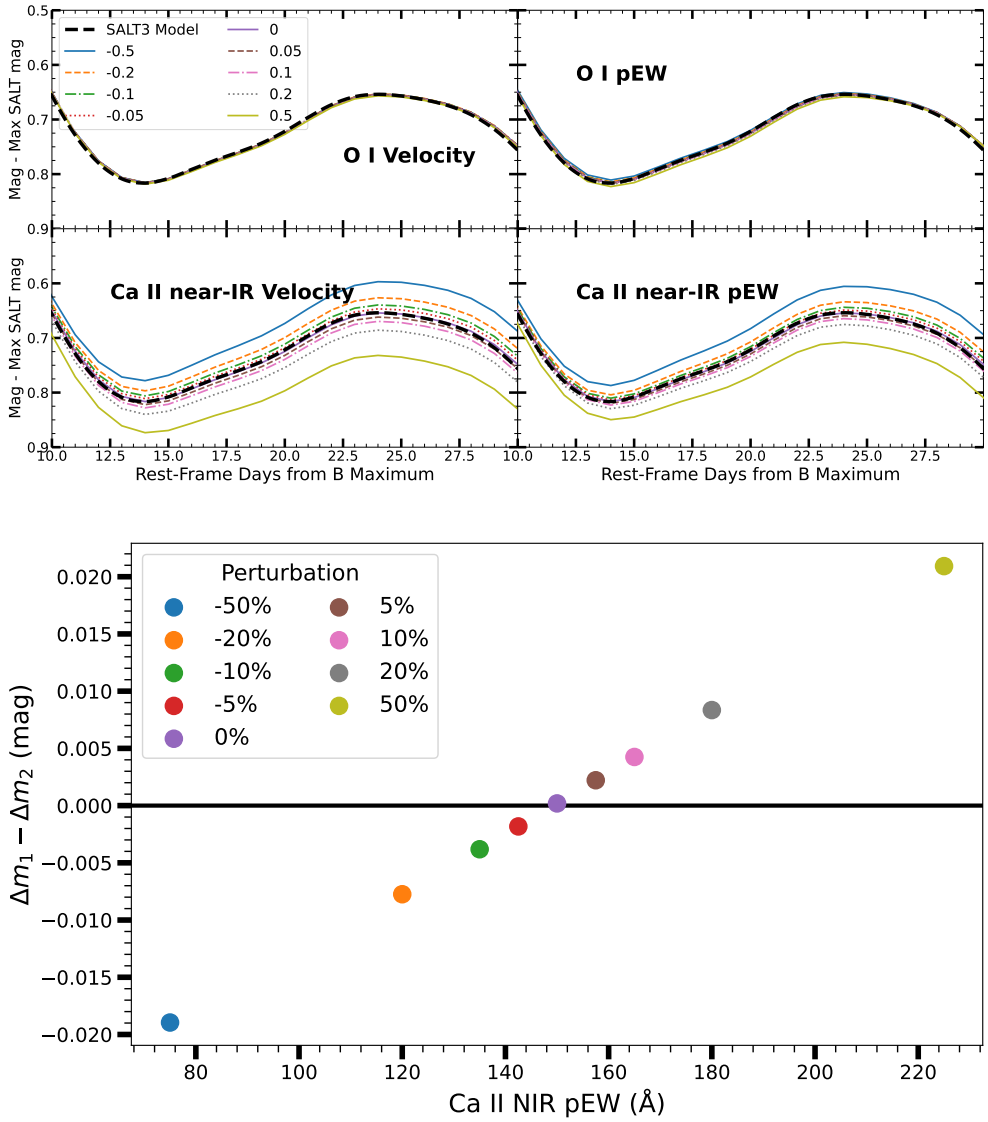

Figure 4.9 Impact of spectroscopic feature perturbations on the i-band light curve and $\Delta m_1 - \Delta m_2$ parameter. The top panels show the i-band light curves for varying modeled O I velocity, O I pseudo equivalent width (pEW), Ca II NIR velocity, and Ca II NIR pEW compared to the SALT3 model. Perturbations in spectroscopic features have a minimal effect on O I velocity and pEW, with negligible changes in the i-band light-curve morphology. In contrast, variations in Ca II NIR velocity and pEW have a noticeable impact on the i-band light-curve characteristics, especially around the secondary maximum and minimum, which we quantify as the parameter $\Delta m_1 - \Delta m_2$. The bottom panel illustrated the relationship between the $\Delta m_1 - \Delta m_2$ parameter and modeled Ca II NIR pEW values for different perturbations. The $\Delta m_1 - \Delta m_2$ are calculated relative to the nominal SALT3 model (0% perturbation), represented with a horizontal black line. Negative Ca II NIR perturbations (e.g., -50%) result in negative $\Delta m_1 - \Delta m_2$ residuals, while positive perturbations (e.g., +50%) lead to positive $\Delta m_1 - \Delta m_2$ values. These results are consistent with the trend found in observational data, as shown in Figure 4.8, supporting the connection between Ca II features and i-band light-curve morphology.

around 3800 Å compared to the low residuals (blue). A similar trend is observed in the Si II λ 6355 region, with the high $\Delta m_1 - \Delta m_2$ residuals showing a slightly stronger absorption profile, as displayed by its deeper minimum near 6150 Å. Finally, in the i-band region, which includes the O I and Ca II NIR triplet features, the high residuals show stronger absorption for Ca II NIR around 8500 Å. The O I absorption is very similar for both populations.

The differences in the strengths and profiles of Ca II, Si II, and Ca II NIR features between the two populations suggest that these spectroscopic properties are strongly tied to the i-band light-curve diversity, agreeing with the results presented previously in this work. For example, high $\Delta m_1 - \Delta m_2$ residuals show stronger Ca absorption and more pronounced differences, matching the models presented in Figure 4.9.

Finally, we note a diversity in the host-galaxy mass. SNe with low $\Delta m_1 - \Delta m_2$ residuals have a flat, high host mass, while SNe with high residuals have more diverse but lower host-galaxy masses. This diversity could imply that high-residual SNe occur in a broader range of host masses, while low-residual SNe could be associated with specific host properties. This potential dependence on the host-galaxy mass could be related to the magnitude offset in the i-band secondary maximum reported in Grayling & Popovic (2024), although its physical origin remains unknown. However, there is evidence that other progenitor properties, such as metallicity, affect the timing of the secondary maximum (higher metallicity causes an earlier secondary maximum, Kasen (2006). Deckers et al. (2024) additionally suggest that metallicity may have a stronger effect on the i-band secondary maximum than the r-band secondary maximum, explain-

ing the stronger secondary maximum in i compared to r. At the same time, Pessi et al. (2022) did not find strong correlations between the timing and strength of the downward concave shape and host-galaxy mass.

In Figure 4.11, we show a comparison between the observed spectrum of the well-sampled SN 2007le, the SALT3 model spectrum, and their respective Gaussian approximations (red dashed line for SN 2007le and blue dotted line for the SALT3 model). SN 2007le has positive $\Delta m_1 - \Delta m_2$ value and a high Ca pEW_0 (162.6 Å) measurement. The SALT3 SED is generated following the procedure for Figure 4.9.

The SALT3 model generally aligns well with the observed spectrum. However, the Ca II NIR triplet absorption feature (around 8200 Å) differs from the SALT3 model approximation, as the model underestimates the depth and width of this feature, which might suggest it may not fully capture the diversity of calcium absorption strengths observed in SNe Ia.

This discrepancy could point to limitations of the SALT3 model in accurately representing certain spectral features, particularly in regions dominated by calcium. These spectral discrepancies could have significant implications for i-band light curves since the Ca II NIR triplet and O I absorption features lie within the wavelength range of the i-band throughput curve and thus directly influence the measured flux in this band, and consequently in light curve fitting and parameter estimation.

To evaluate the effect of the spectral features on the photometry, we compare the observed i-band light curve of SN 2006D to the generated i-band SALT3 model and to the synthetic photometry data adjusted based on i-band spectral features of SN 2006D (O I and Ca II NIR), as shown in Figure 4.12.

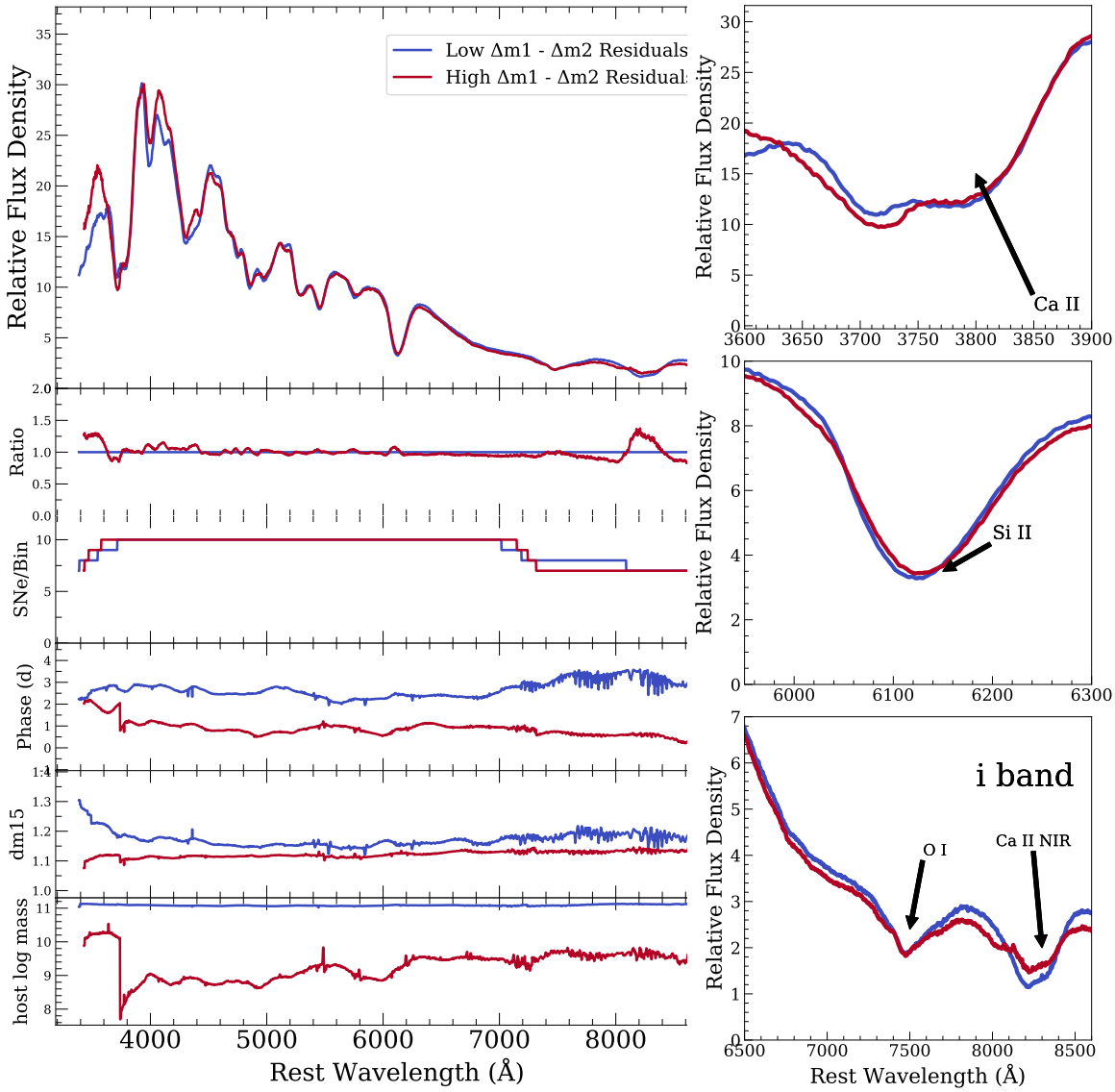

Figure 4.10 Composite spectra of a subset of the SNe Ia in Fig. 4.8 divided by low (blue) and high (red) $\Delta m_1 - \Delta m_2$ residuals. The left panels display the entire spectral range and include additional metadata such as phase Δm_{15} (B). We restrict data with similar phase and Δm_{15} (B). The right panels zoom in on key spectral regions corresponding to important features such as Ca II H&K, Si II λ6355, O I, and the Ca II NIR triplet. The differences in the strengths and profiles of Ca II, Si II, and Ca II NIR features between the two populations suggest that these spectroscopic properties are strongly tied to the i-band light-curve diversity.

The SALT3 model provides a good overall fit to the observed light curve, capturing the peak and decline behavior. However, some discrepancies are evident,

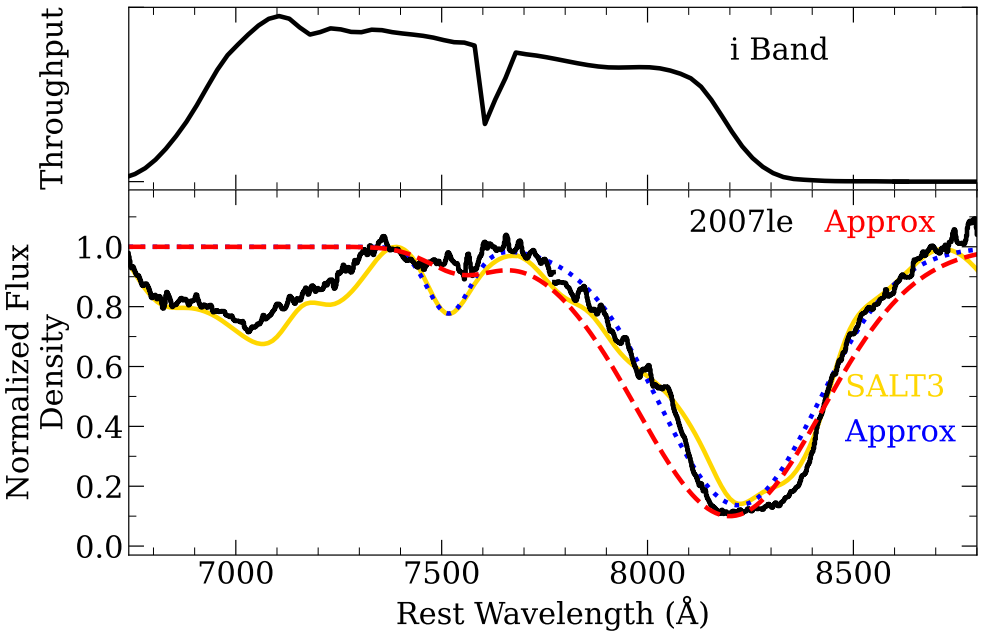

Figure 4.11 Normalized flux for SN 2007le at +22 days from B maximum light (black solid line) compared to the generated SALT3 model (gold), a Gaussian approximation of the SALT3 model (blue dotted line), and a Gaussian approximation of the SN 2007le spectrum (red dashed line). This comparison highlights differences in fitting the spectral features within the i-band region using the SALT3 model and the observed spectrum.

especially around the secondary maximum at approximately 25–30 days past the B-band maximum. The SALT3 model underestimates the observed flux in this region, showing it does not account entirely for all physical processes influencing the i-band light curve.

The shifted data, adjusted based on the Ca II NIR and O I spectroscopic features of SN 2006D, show improved alignment with the SALT3 model. The SALT3 model and the shifted data match particularly well around the first peak and the secondary maximum of the i-band light curve. This example suggests that spectroscopic features, such as the strength and velocity of calcium lines, can significantly impact the i-band light-curve morphology. However, we note that for this model for SN 2006D, there is a discrepancy between the SALT3 model and the observed and shifted data around the i-band minimum between peaks.

The impacts of calcium and silicon spectral features on light curves and spectra could have important implications for cosmology. Variations in these features could influence the standardization of SNe Ia as distance indicators, as the SALT3 model does not account for these discrepancies (Kenworthy et al. 2021b; Taylor et al. 2023). The current SALT3 parameterization, therefore, might not be entirely accurate and could potentially introduce new systematic uncertainties currently not addressed in cosmological analyses (Brout et al. 2022a; DES Collaboration et al. 2024).

Additionally, there is evidence that the Hubble residuals (the differences between the distance moduli measured from the observations and the cosmological models) have an intrinsic scatter that could be related to host-galaxy mass (Kelly et al. 2010; Lampeitl et al. 2010; Sullivan et al. 2010) or even SN ejecta velocities (Siebert et al.

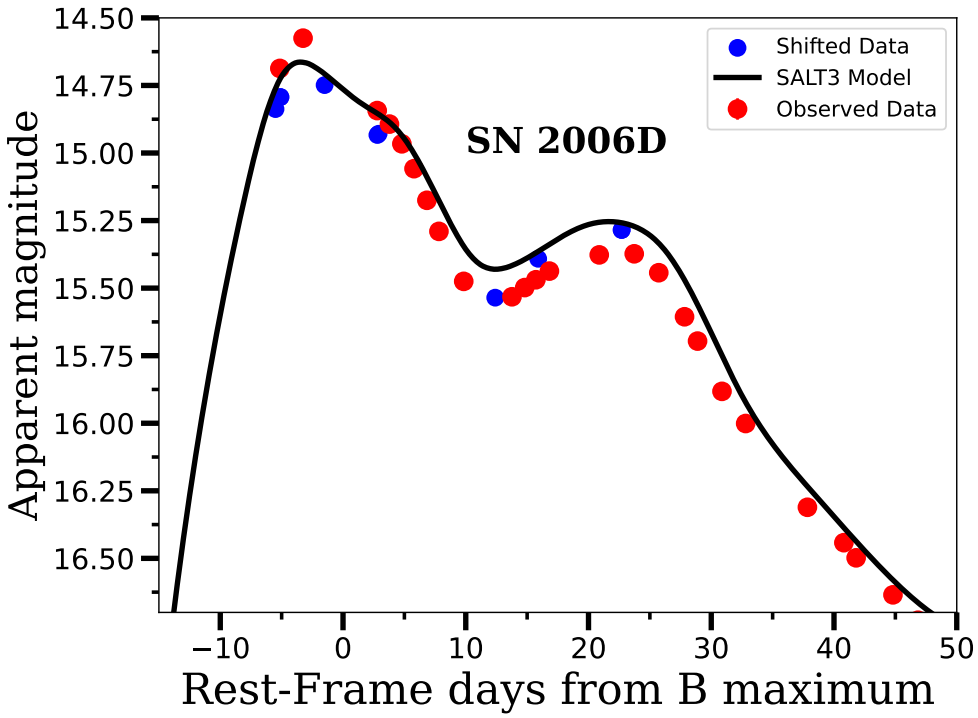

Figure 4.12 Comparison of observed photometric data (red points) with the SALT3 model (black line) and shifted model data (blue points) for SN 2006D. The data is shifted based on the SN spectrum. The shifted data align more closely with the SALT3 model, especially around the first peak and the secondary maximum. This suggests that applying the shift improves the agreement between the model and the observed data, particularly in key regions of the light curve.

2020). Pessi et al. (2022) also suggest that SNe Ia with the strongest downward concave i-band light-curve feature have smaller Hubble residuals. Future work will explore possible correlations between the $\Delta m_1 - \Delta m_2$ parameter and Hubble residuals.

4.7 Conclusion

The results presented in this work provide evidence that spectroscopic features such as Ca II pEW_0 and Si II v_0 play an important role in shaping the diversity of i-band light curves of SNe Ia. The statistically significant correlations between these spectroscopic features and the $\Delta m_1 - \Delta m_2$ residuals show a physical connection between spectral features and i-band light curves, highlighting the potential for spectroscopic measurements to improve light-curve modeling. Additionally, the strong dependence of $\Delta m_1 - \Delta m_2$ on variations in Ca II NIR velocity and pseudo equivalent width further suggest that calcium-rich ejecta directly impact opacity and flux redistribution in the NIR, agreeing with previous studies, emphasizing the sensitivity of i-band strength and morphology to the Ca II NIR features.

Composite spectra reinforce the connection between the photometric behavior and spectral variations by showing differences in Ca II H&K, Si II, and Ca II NIR features between subsamples with different $\Delta m_1 - \Delta m_2$, providing further evidence that i-band light curve diversity is possibly linked to variations in ejecta velocity and composition. However, the relative similarity in O I features between the two subsamples may suggest that oxygen is less significant in causing i-band diversity, pointing instead to calcium and silicon as the dominant contributors.

Incorporating additional spectroscopic information into light curve fitting has the potential to improve the SALT3 model, allowing it to capture better the physical diversity observed in SNe Ia and improve the accuracy of parameter estimation, SN homogenization and distance measurements. Our current dataset is small; however, future large-scale surveys, such as those conducted by the Vera C. Rubin Observatory and the respective follow-up spectra, will provide an unprecedented volume of SN Ia observations, offering new opportunities to deepen our understanding of the connections between SN Ia spectral features, i-band light-curve morphology, physical processes, environmental dependency, and the accuracy of SNe Ia as precise cosmological distance indicators.

Chapter 5

Summary and Future Directions

In this dissertation, I have presented the Swope Supernova Survey, detailing its motivation, characteristics, and scientific contributions across a wide range of transient astrophysics, emphasizing the SN Ia data release, and introduced a new parametrization of SN Ia i-band light curves, revealing a strong correlation with spectral parameters.

In Chapter 2, I provided a comprehensive overview of the Swope Supernova Survey. Since its beginning in 2016, the survey has become an important photometric resource for following interesting transients below $+30^\circ$ declination. Its wide wavelength range (3000-8000 Å, u band to i band), precise calibration, and high observing cadence have led the survey to make a significant impact on the transient science community, contributing to over 30 papers in a wide variety of topics, such as (1) SN cosmology (Rojas-Bravo et al., submitted; Burns et al. (2020); (2) SN Ia physics (Dimitriadis et al. 2019a,b; Li et al. 2019; Wang et al. 2021b, 2024; Pearson et al. 2024); (3) young non-SN Ia transients (Kilpatrick et al. 2018b; Tartaglia et al. 2018; Armstrong et al. 2021; Gagliano et al. 2021; Jacobson-Galán et al. 2024); (4) exotic transients (Nicholl et al.

2019; Hung et al. 2020, 2021; Holoien et al. 2020; Neustadt et al. 2020; Jacobson-Galán et al. 2020c; Barna et al. 2021b; Hinkle et al. 2021; Jencson et al. 2021; Pastorello et al. 2022; Chen et al. 2023a,b); (5) SN progenitors (Kilpatrick et al. 2018a,c, 2022b; Vazquez et al. 2023); and (6) gravitational-wave counterpart observations and searches (Abbott et al. 2017; Coulter et al. 2017; Drout et al. 2017a; Kilpatrick et al. 2017; Murguia-Berthier et al. 2017b; Siebert et al. 2017; Shappee et al. 2017; Piro & Kollmeier 2018; Kilpatrick et al. 2021b; Coulter et al. 2024). My contributions have been fundamental to these efforts. I have reduced most of the Swope Supernova Survey data and coordinated and scheduled all its observations since 2017 for approximately 1000 nights. The Swope Supernova Survey is currently ongoing, with multiple transient light curves still to be analyzed and published, further cementing the survey's legacy and impact on the SN community.

In Chapter 3, I describe in detail the Swope Supernova Survey's first SN Ia data release, which I led. With over 100 high-cadence SN Ia light curves in five photometric bands ($BVgri$) and the development of a new photometric reduction pipeline taking into account the PSF variations across the Swope detector, this data release will contribute to the overall low-redshift SN Ia samples currently published (Filippenko et al. 2001a; Ganeshalingam et al. 2010; Stahl et al. 2019; Hicken et al. 2009, 2012; Krisciunas et al. 2017; Foley et al. 2018; Scolnic et al. 2022; DES Collaboration et al. 2024). Future data releases of the Swope Supernova Survey are particularly exciting. While the first data release published $\approx$ 100 SN Ia, over 350 total SNe Ia have been observed in this program, of which approximately 80% currently have template observations. We are presently striving to reach 100%. Additionally, since the Swope Supernova Survey uses

the same photometric system as the Carnegie Supernova Project I, once we recalibrate the CSP-I data, and combine the CSP-I data, the Swope Supernova Survey data, and the CSP-II data (Phillips et al. 2019) into one homogenous dataset, we will be making a critical contribution to the total cosmological sample of SNe Ia, which currently has $\approx$ 1000 SNe Ia (Scolnic et al. 2022). By itself, the entire Swope sample could also represent approximately 75% of the low-redshift SN Ia sample required for *Roman* mission success (Spergel et al. 2015; Roman et al. 2018).

Future Swope Supernova Survey SN Ia data releases will also improve in multiple ways. First, the current data release is limited to information gathered in one amplifier, similar to the CSP-I observations. We are presently expanding the photometric reductions to the four amplifiers used in the Swope detector. Additionally, we will improve the photometry pipeline. First, we will recover data currently lost due to insufficient stars detected for a robust PSF creation. Second, future data releases will incorporate thousands of u-band observations, which are vital for the SALT3 modeling efforts (Kenworthy et al. 2021b). Third, we will improve our calibration. Currently, the Swope Supernova Survey photometry is tied to the PS1 footprint. However, PS1 observations are restricted to above -30° declination, which has limited the calibration of Swope SNe observations below this threshold. However, with the imminent advent of the Vera Rubin Observatory Legacy Survey of Space and Time (LSST), we will recalibrate all our data, including the u band, to these precisely calibrated observations (Ivezić et al. 2019).

Finally, in Chapter 4, we have introduced a novel parametrization of the i-band light curve secondary maximum and minimum, showing a strong correlation with several

spectral parameters. Specifically, we find strong correlations between the $\Delta m_1 - \Delta m_2$ parameter (defined as the difference between the data and the model at the i-band minimum and the secondary maximum) and the spectral parameters Ca II pEW_0 and Si II v_0. Additionally, we show the impact that different spectral parameters have on the composite spectra and synthetic photometry of SN Ia i-band light curves, revealing the limitations of the SALT3 SN Ia model in capturing these variations. Furthermore, there are hints that SN Ia host-galaxy mass or metallicity could have a significant effect in shaping the i-band behavior, although the physical reason remains uncertain (Pessi et al. 2022; Deckers et al. 2024; Grayling & Popovic 2024).

While our current dataset is limited, the beginning of large-scale surveys, such as LSST, promises a transformative increase in SN Ia observations. These surveys will not only provide an unprecedented volume of photometric data but, when combined with frequent and high-quality spectral observations, will begin a new era in observational astronomy. With these unique observations, we will be able to further explore in detail the connections between SN Ia spectral features, i-band light curve morphology and diversity, physical processes, environmental dependencies, and the accuracy of SNe Ia as precise cosmological distance indicators.

Bibliography

Abbott B. P., et al., 2016, Physical Review Letters, 116, 061102

Abbott B. P., et al., 2017, ApJ, 848, L12

Alam S., et al., 2017, MNRAS, 470, 2617

Aleo P. D., et al., 2023, ApJS, 266, 9

Anderson J., 2016, Empirical Models for the WFC3/IR PSF, Instrument Science Report WFC3 2016-12, 42 pages

Anderson J., King I. R., 2000, PASP, 112, 1360

Armstrong P., et al., 2021, MNRAS, 507, 3125

Arnett W. D., 1982, ApJ, 253, 785

Barna B., et al., 2021a, MNRAS, 501, 1078

Barna B., et al., 2021b, MNRAS, 501, 1078

Becker A., 2015, HOTPANTS: High Order Transform of PSF ANd Template Subtraction, Astrophysics Source Code Library (ascl:1504.004)

Bellm E. C., et al., 2019, PASP, 131, 018002

Bertin E., Arnouts S., 1996, A&AS, 117, 393

Bertin E., Mellier Y., Radovich M., Missonnier G., Didelon P., Morin B., 2002, in

Bohlender D. A., Durand D., Handley T. H., eds, Astronomical Society of the Pacific Conference Series Vol. 281, Astronomical Data Analysis Software and Systems XI. p. 228

Bessell M. S., 1990, PASP, 102, 1181

Betoule M., et al., 2014, A&A, 568, A22

Blondin S., et al., 2006, AJ, 131, 1648

Blondin S., Mandel K. S., Kirshner R. P., 2011, A&A, 526, A81+

Bohlin R. C., Gordon K. D., Tremblay P.-E., 2014, PASP, 126, 711

Bohlin R. C., Hubeny I., Rauch T., 2020, AJ, 160, 21

Bradley L., et al., 2024, astropy/photutils: 1.11.0, doi:10.5281/zenodo.10671725, https://doi.org/10.5281/zenodo.10671725

Brout D., et al., 2019, ApJ, 874, 106

Brout D., et al., 2022a, ApJ, 938, 110

Brout D., et al., 2022b, ApJ, 938, 111

Brownsberger S., Brout D., Scolnic D., Stubbs C. W., Riess A. G., 2021, arXiv e-prints, p. arXiv:2110.03486

Burns C. R., et al., 2014, ApJ, 789, 32

Burns C. R., et al., 2020, ApJ, 895, 118

Calabretta M. R., Greisen E. W., 2002, A&A, 395, 1077

Chambers K. C., et al., 2016, preprint, (arXiv:1612.05560)

Chauvenet W., 1863, A manual of spherical and practical astronomy

Chen Y., et al., 2023a, ApJ, 955, 42

Chen Y., Drout M. R., Piro A. L., Kilpatrick C. D., Foley R. J., Rojas-Bravo C., Magee

M. R., 2023b, ApJ, 955, 43

Clemens J. C., Crain J. A., Anderson R., 2004, in Moorwood A. F. M., Iye M., eds, Society of Photo-Optical Instrumentation Engineers (SPIE) Conference Series Vol. 5492, Ground-based Instrumentation for Astronomy. pp 331–340, doi:10.1117/12.550069

Colgate S. A., McKee C., 1969, ApJ, 157, 623

Contreras C., et al., 2010, AJ, 139, 519

Coulter D. A., et al., 2017, Science, 358, 1556

Coulter D. A., et al., 2023, PASP, 135, 064501

Coulter D. A., et al., 2024, arXiv e-prints, p. arXiv:2404.15441

DES Collaboration et al., 2024, arXiv e-prints, p. arXiv:2401.02929

Dai M., Jones D. O., Kenworthy W. D., Kessler R., Pierel J. D. R., Foley R. J., Jha S. W., Scolnic D. M., 2023, ApJS, 267, 1

Deckers M., et al., 2024, arXiv e-prints, p. arXiv:2406.19460

Dhawan S., Leibundgut B., Spyromilio J., Maguire K., 2015, MNRAS, 448, 1345

Dhawan S., et al., 2022, MNRAS, 510, 2228

Di Valentino E., et al., 2021, Classical and Quantum Gravity, 38, 153001

Dimitriadis G., et al., 2019a, ApJ, 870, L1

Dimitriadis G., et al., 2019b, ApJ, 870, L14

Do A., et al., 2024, arXiv e-prints, p. arXiv:2403.05620

Drout M. R., et al., 2017a, Science, 358, 1570

Drout M. R., et al., 2017b, Science, 358, 1570

Elias J. H., Frogel J. A., Hackwell J. A., Persson S. E., 1981, ApJ, 251, L13

Filippenko A. V., 1997, ARA&A, 35, 309

Filippenko A. V., et al., 1992a, AJ, 104, 1543

Filippenko A. V., et al., 1992b, ApJ, 384, L15

Filippenko A. V., Li W. D., Treffers R. R., Modjaz M., 2001a, in Paczynski B., Chen W.-P., Lemme C., eds, Astronomical Society of the Pacific Conference Series Vol. 246, IAU Colloq. 183: Small Telescope Astronomy on Global Scales. p. 121

Filippenko A. V., Li W. D., Treffers R. R., Modjaz M., 2001b, in Paczynski B., Chen W.-P., Lemme C., eds, Astronomical Society of the Pacific Conference Series Vol. 246, IAU Colloq. 183: Small Telescope Astronomy on Global Scales. p. 121

Filippenko A. V., Chornock R., Swift B., Modjaz M., Simcoe R., Rauch M., 2003, IAU Circ., 8159, 2

Flewelling H. A., et al., 2020, ApJS, 251, 7

Folatelli G., et al., 2010, AJ, 139, 120

Foley 2017, GRB Coordinates Network, 21557

Foley R. J., Narayan G., Challis P. J., Filippenko A. V., Kirshner R. P., Silverman J. M., Steele T. N., 2010, ApJ, 708, 1748

Foley R. J., Sanders N. E., Kirshner R. P., 2011, ApJ, 742, 89

Foley R. J., et al., 2013, ApJ, 767, 57

Foley et al. 2017, GRB Coordinates Network, 21536

Foley R. J., et al., 2018, MNRAS, 475, 193

Freedman W. L., et al., 2001, Astrophys. J. , 553, 47

Freedman W. L., et al., 2009, ApJ, 704, 1036

Fukugita M., Ichikawa T., Gunn J. E., Doi M., Shimasaku K., Schneider D. P., 1996, AJ, 111, 1748

GBM-LIGO 2017, GRB Coordinates Network, 21506

Gagliano A., Narayan G., Engel A., Carrasco Kind M., LSST Dark Energy Science Collaboration 2021, ApJ, 908, 170

Gagliano A., et al., 2022, ApJ, 924, 55

Gal-Yam A., 2017, Observational and Physical Classification of Supernovae. Springer International Publishing, Cham, pp 195–237, doi:10.1007/978-3-319-21846-5˙35, https://doi.org/10.1007/978-3-319-21846-5_35

Ganeshalingam M., et al., 2010, ApJS, 190, 418

Gezari S., 2021, ARA&A, 59, 21

Grayling M., Popovic B., 2024, arXiv e-prints, p. arXiv:2410.13747

Grayling M., Thorp S., Mandel K. S., Dhawan S., Uzsoy A. S. M., Boyd B. M., Hayes E. E., Ward S. M., 2024, MNRAS, 531, 953

Guy J., et al., 2007, A&A, 466, 11

Guy J., et al., 2010, A&A, 523, A7+

Haas M. R., et al., 2010, ApJ, 713, L115

Hamuy M., Phillips M. M., Suntzeff N. B., Schommer R. A., Maza J., Aviles R., 1996, AJ, 112, 2391

Hamuy M., et al., 2006, Publ. Astron. Soc. Pac. , 118, 2

Hicken M., Garnavich P. M., Prieto J. L., Blondin S., DePoy D. L., Kirshner R. P., Parrent J., 2007, ApJ, 669, L17

Hicken M., et al., 2009, ApJ, 700, 331

Hicken M., et al., 2012, ApJS, 200, 12

Hinkle J. T., et al., 2021, MNRAS, 500, 1673

Ho A. Y. Q., et al., 2019, ApJ, 871, 73

Ho A. Y. Q., et al., 2023, ApJ, 949, 120

Hodgkin S. T., et al., 2021, A&A, 652, A76

Holoien T. W. S., et al., 2020, ApJ, 898, 161

Holz D. E., Hughes S. A., 2005, ApJ, 629, 15

Hounsell R., et al., 2018, ApJ, 867, 23

Howell D. A., et al., 2006, 4, 443, 308

Hoyle F., Fowler W. A., 1960, ApJ, 132, 565

Hsiao E. Y., Conley A., Howell D. A., Sullivan M., Pritchet C. J., Carlberg R. G., Nugent P. E., Phillips M. M., 2007, ApJ, 663, 1187

Hung T., et al., 2020, ApJ, 903, 31

Hung T., et al., 2021, ApJ, 917, 9

INTEGRAL 2017, GRB Coordinates Network, 21507

Iben Jr. I., Tutukov A. V., 1984, ApJS, 54, 335

Ivezić Ž., et al., 2019, ApJ, 873, 111

Jacobson-Galán W. V., et al., 2020a, ApJ, 896, 165

Jacobson-Galán W. V., et al., 2020b, ApJ, 898, 166

Jacobson-Galán W. V., et al., 2020c, ApJ, 898, 166

Jacobson-Galán W. V., et al., 2024, arXiv e-prints, p. arXiv:2403.02382

Jencson J. E., et al., 2021, ApJ, 920, 127

Jha S. W., 2017, preprint, (arXiv:1707.01110)

Jha S., et al., 2006, AJ, 131, 527

Jones D. H., et al., 2009, MNRAS, 399, 683

Jones D. O., et al., 2018a, ApJ, 857, 51

Jones D. O., et al., 2018b, ApJ, 857, 51

Jones D. O., et al., 2018c, ApJ, 867, 108

Jones D. O., et al., 2019, ApJ, 881, 19

Jones D. O., et al., 2021, ApJ, 908, 143

Jones D. O., Kenworthy W. D., Dai M., Foley R. J., Kessler R., Pierel J. D. R., Siebert M. R., 2023, ApJ, 951, 22

Kamionkowski M., Riess A. G., 2023, Annual Review of Nuclear and Particle Science, 73, 153

Kasen D., 2006, ApJ, 649, 939

Kasen D., 2010, ApJ, 708, 1025

Kasen D., Woosley S. E., 2007, ApJ, 656, 661

Kelly P. L., Hicken M., Burke D. L., Mandel K. S., Kirshner R. P., 2010, ApJ, 715, 743

Kenworthy W. D., et al., 2021a, ApJ, 923, 265

Kenworthy W. D., et al., 2021b, ApJ, 923, 265

Kessler R., et al., 2009, PASP, 121, 1028

Kilpatrick C. D., et al., 2017, Science, 358, 1583

Kilpatrick C. D., et al., 2018a, preprint, (arXiv:1806.08436)

Kilpatrick C. D., et al., 2018b, MNRAS, 473, 4805

Kilpatrick C. D., et al., 2018c, MNRAS, 473, 4805

Kilpatrick C. D., et al., 2021a, MNRAS, 504, 2073

Kilpatrick C. D., et al., 2021b, ApJ, 923, 258

Kilpatrick C. D., et al., 2022a, ApJ, 926, 49

Kilpatrick C. D., Coulter D. A., Foley R. J., Piro A. L., Rest A., Rojas-Bravo C., Siebert M. R., 2022b, ApJ, 936, 111

Krisciunas K., et al., 2001, AJ, 122, 1616

Krisciunas K., et al., 2003, AJ, 125, 166

Krisciunas K., et al., 2011, AJ, 142, 74

Krisciunas K., et al., 2017, AJ, 154, 211

Kushnir D., Katz B., Dong S., Livne E., Fernández R., 2013, ApJ, 778, L37

LIGO/Virgo collaboration 2017a, GRB Coordinates Network, 21509

LIGO/Virgo collaboration 2017b, GRB Coordinates Network, 21513

LSST Science Collaboration et al., 2009, preprint, (arXiv:0912.0201)

Lampeitl H., et al., 2010, ApJ, 722, 566

Lattimer J. M., Schramm D. N., 1974, ApJ, 192, L145

Leaman J., Li W., Chornock R., Filippenko A. V., 2011, MNRAS, 412, 1419

Leibundgut B., et al., 1993, AJ, 105, 301

Li W. D., et al., 2000, in Holt S. S., Zhang W. W., eds, American Institute of Physics Conference Series Vol. 522, American Institute of Physics Conference Series. pp 103–106 (arXiv:astro-ph/9912336), doi:10.1063/1.1291702

Li W., et al., 2001, PASP, 113, 1178

Li W., Filippenko A. V., Chornock R., Jha S., 2003, PASP, 115, 844

Li W., et al., 2011, Mon. Not. R. Astron. Soc. , 412, 1441

Li W., et al., 2019, ApJ, 870, 12

Linder E. V., 2003, Physical Review Letters, 90, 091301

Liu Z.-W., Röpke F. K., Han Z., 2023, Research in Astronomy and Astrophysics, 23,

082001

Livne E., 1990, ApJ, 354, L53

Lu J., et al., 2023, ApJ, 948, 27

Maeda K., Terada Y., 2016, International Journal of Modern Physics D, 25, 1630024

Maoz D., Mannucci F., Nelemans G., 2014, ARA&A, 52, 107

Margutti R., et al., 2019, ApJ, 872, 18

Martini P., et al., 2014, in Ramsay S. K., McLean I. S., Takami H., eds, Society of Photo-Optical Instrumentation Engineers (SPIE) Conference Series Vol. 9147, Ground-based and Airborne Instrumentation for Astronomy V. p. 91470Z (arXiv:1407.4541), doi:10.1117/12.2056834

Mazzali P. A., Nomoto K., Cappellaro E., Nakamura T., Umeda H., Iwamoto K., 2001, ApJ, 547, 988

Meikle W. P. S., 2000, MNRAS, 314, 782

Miller J., Stone R., 1994, The Kast Double Spectograph. Lick Observatory technical reports, University of California Observatories/Lick Observatory, https://books.google.com/books?id=QXk2AQAAIAAJ

Minkowski R., 1941, PASP, 53, 224

Murguia-Berthier A., et al., 2017a, ApJ, 848, L34

Murguia-Berthier A., et al., 2017b, ApJ, 848, L34

Narayan G., et al., 2019, ApJS, 241, 20

Neustadt J. M. M., et al., 2020, MNRAS, 494, 2538

Nicholl M., et al., 2019, MNRAS, 488, 1878

Nissanke S., Holz D. E., Dalal N., Hughes S. A., Sievers J. L., Hirata C. M., 2013, arXiv

e-prints,

Nomoto K., 1982, ApJ, 257, 780

Nugent P., Phillips M., Baron E., Branch D., Hauschildt P., 1995, ApJ, 455, L147

Oke J. B., Gunn J. E., 1983, ApJ, 266, 713

Oke J. B., et al., 1995, PASP, 107, 375

One-Meter Two-Hemisphere (1M2H) collaboration 2017, GRB Coordinates Network, 21529

Padmanabhan N., et al., 2008, ApJ, 674, 1217

Pakmor R., Kromer M., Röpke F. K., Sim S. A., Ruiter A. J., Hillebrandt W., 2010, 4, 463, 61

Pakmor R., Kromer M., Taubenberger S., Sim S. A., Röpke F. K., Hillebrandt W., 2012, ApJ, 747, L10

Pan Y.-C., et al., 2014, MNRAS, 438, 1391

Pan Y. C., et al., 2017, ApJ, 848, L30

Parrent J. T., et al., 2012, ApJ, 752, L26

Pastorello A., et al., 2022, arXiv e-prints, p. arXiv:2208.02782

Pearson J., et al., 2024, ApJ, 960, 29

Perley D. A., et al., 2019, MNRAS, 484, 1031

Perlmutter S., et al., 1999, ApJ, 517, 565

Pessi P. J., et al., 2022, MNRAS, 510, 4929

Phillips M. M., 1993, ApJ, 413, L105

Phillips M. M., Wells L. A., Suntzeff N. B., Hamuy M., Leibundgut B., Kirshner R. P., Foltz C. B., 1992, AJ, 103, 1632

Phillips M. M., Lira P., Suntzeff N. B., Schommer R. A., Hamuy M., Maza J., 1999, AJ, 118, 1766

Phillips M. M., et al., 2019, PASP, 131, 014001

Phillips M. M., et al., 2024, ApJS, 273, 16

Phinney E. S., 1989, 4, 340, 595

Pierel J. D. R., et al., 2022, ApJ, 939, 11

Pignata G., et al., 2009, in G. Giobbi, A. Tornambe, G. Raimondo, M. Limongi, L. A. Antonelli, N. Menci, & E. Brocato ed., American Institute of Physics Conference Series Vol. 1111, American Institute of Physics Conference Series. pp 551–554 (arXiv:0812.4923), doi:10.1063/1.3141608

Piro A. L., Kollmeier J. A., 2018, ApJ, 855, 103

Piro A. L., Morozova V. S., 2016, ApJ, 826, 96

Planck Collaboration et al., 2018, preprint, (arXiv:1807.06209)

Pskovskii I. P., 1978, AZh, 55, 420

Rees M. J., 1988, 4, 333, 523

Rest A., et al., 2005, ApJ, 634, 1103

Rest A., et al., 2014, ApJ, 795, 44

Rheault J.-P., Mondrik N. P., DePoy D. L., Marshall J. L., Suntzeff N. B., 2014, in Ground-based and Airborne Instrumentation for Astronomy V. p. 91475L, doi:10.1117/12.2063560

Riess A. G., Press W. H., Kirshner R. P., 1996, ApJ, 473, 88

Riess A. G., et al., 1998, AJ, 116, 1009

Riess A. G., et al., 1999, AJ, 117, 707

Riess A. G., Casertano S., Yuan W., Bowers J. B., Macri L., Zinn J. C., Scolnic D., 2021, ApJ, 908, L6

Riess A. G., et al., 2022, ApJ, 934, L7

Riess A. G., et al., 2024, ApJ, 977, 120

Rigault M., et al., 2013, A&A, 560, A66

Rigault M., et al., 2018, arXiv e-prints,

Rigault M., et al., 2024, arXiv e-prints, p. arXiv:2406.02073

Roman M., et al., 2018, A&A, 615, A68

Rose B. M., et al., 2021, arXiv e-prints, p. arXiv:2111.03081

Ross A. J., Samushia L., Howlett C., Percival W. J., Burden A., Manera M., 2015, MNRAS, 449, 835

Rubin D., et al., 2023, arXiv e-prints, p. arXiv:2311.12098

STScI Development Team 2013, pysynphot: Synthetic photometry software package, Astrophysics Source Code Library, record ascl:1303.023

Sand D. J., Brown T., Haynes R., Dubberley M., 2011, in American Astronomical Society Meeting Abstracts #218. p. 132.03

Scalzo R., et al., 2012, ApJ, 757, 12

Schechter P. L., Mateo M., Saha A., 1993, PASP, 105, 1342

Schlafly E. F., et al., 2012, ApJ, 756, 158

Scolnic D., et al., 2015, Astrophys. J. , 815, 117

Scolnic D. M., et al., 2018, ApJ, 859, 101

Scolnic D., et al., 2022, ApJ, 938, 113

Shappee B. J., et al., 2014, ApJ, 788, 48

Shappee B. J., et al., 2017, Science, 358, 1574

Siebert M. R., et al., 2017, ApJ, 848, L26

Siebert M. R., et al., 2019, MNRAS, 486, 5785

Siebert M. R., Foley R. J., Jones D. O., Davis K. W., 2020, MNRAS, 493, 5713

Silverman J. M., Ganeshalingam M., Li W., Filippenko A. V., Miller A. A., Poznanski D., 2011, MNRAS, 410, 585

Silverman J. M., Kong J. J., Filippenko A. V., 2012, MNRAS, 425, 1819

Silverman J. M., et al., 2013, ApJS, 207, 3

Speagle J. S., 2019, arXiv e-prints, p. arXiv:1909.12313

Spergel D., et al., 2015, preprint, (arXiv:1503.03757)

Stahl B. E., et al., 2019, MNRAS, 490, 3882

Stetson P. B., 1987, PASP, 99, 191

Stritzinger M. D., et al., 2011, AJ, 142, 156

Sullivan M., et al., 2010, MNRAS, 406, 782

Tartaglia L., et al., 2018, ApJ, 853, 62

Taubenberger S., 2017, The Extremes of Thermonuclear Supernovae. Springer International Publishing, Cham, pp 317–373, doi:10.1007/978-3-319-21846-5˙37, https://doi.org/10.1007/978-3-319-21846-5_37

Taubenberger S., et al., 2011, MNRAS, 412, 2735

Taylor G., et al., 2023, MNRAS, 520, 5209

Tody D., 1986, in Crawford D. L., ed., Society of Photo-Optical Instrumentation Engineers (SPIE) Conference Series Vol. 627, Instrumentation in astronomy VI. p. 733, doi:10.1117/12.968154

Tonry J. L., et al., 2018, PASP, 130, 064505

Tripp R., 1998, A&A, 331, 815

Uddin S. A., et al., 2023, arXiv e-prints, p. arXiv:2308.01875

Vazquez J., Kilpatrick C. D., Dimitriadis G., Foley R. J., Piro A. L., Rest A., Rojas-Bravo C., 2023, ApJ, 949, 75

Verde L., Treu T., Riess A. G., 2019, arXiv e-prints,

Wang Q., et al., 2021a, ApJ, 923, 167

Wang Q., et al., 2021b, ApJ, 923, 167

Wang Q., et al., 2024, ApJ, 962, 17

Webbink R. F., 1984, ApJ, 277, 355

Whelan J., Iben I. J., 1973, ApJ, 186, 1007

Woosley S. E., Taam R. E., Weaver T. A., 1986, ApJ, 301, 601

Yamanaka M., et al., 2009, ApJ, 707, L118